Fast Magnetosonic Wave Heating of the NUWMAK Tokamak Reactor

J.E. Scharer, D.T. Blackfield, J.B. Beyer, and T.K. Mau

May 1978

UWFDM-227

FUSION TECHNOLOGY INSTITUTE

UNIVERSITY OF WISCONSIN

MADISON WISCONSIN

Fast Magnetosonic Wave Heating of the NUWMAK Tokamak Reactor

J.E. Scharer, D.T. Blackfield, J.B. Beyer, and T.K. Mau

Fusion Technology Institute
University of Wisconsin
1500 Engineering Drive
Madison, WI 53706

http://fti.neep.wisc.edu

May 1978

UWFDM-227

Fast Magnetosonic Wave Heating of the NUWMAK Tokamak Reactor

J.E. Scharer*, D.T. Blackfield+, J.B. Beyer*, and T.K. Mau+

Electrical and Computer Engineering* and Nuclear Engineering+ Departments,

University of Wisconsin, Madison, Wisconsin 53706

June, 1978

UWFDM-227

This work was supported by DOE Contract ET-78-S-02-4636.

Abstract

We present studies of radiofrequency (RF) coupling and heating to ignition of a conceptual tokamak fusion reactor by means of the fast magnetosonic wave at the second ion cyclotron harmonic. First, the current status of fast magnetosonic wave propagation and heating, mode conversion, and eigenmode theory is briefly reviewed. Next, a space-averaged, time-dependent startup model is used to describe the role of RF heating for ignition of a tokamak reactor. The computational code simultaneously solves the ion and electron energy balance equations. Conduction, convection, and radiative losses are compared with the ion and electron wave heating mechanisms together with alpha-particle heating resulting from fusion reactions. The model shows that 200 MJ corresponding to an RF power level of 80 MW for a three second period is required to ignite a 700 MWe fusion power plant the size of NUWMAK. To couple the RF power to the torus, both external cavities coupled by apertures and poloidal coil systems are considered. A calculation of the wave coupling from an external vacuum-filled cavity to fast magnetosonic waves via apertures is discussed. The cavity coupling scheme allows an impedance transformation from a coaxial feed to the plasma wave modes and distributes the power flow over a larger surface area than is the case for coils. This minimizes breakdown effects by reducing the wave field strength at the apertures. A description of the hardware necessary to accomplish the task is presented and heat transfer, neutron flux, material, and power handling considerations are discussed. It is concluded that external cavity coupling offers potential technological advantages for a reactor over coaxial coupling

to coils within the reactor chamber. The use of coils is also possible since it appears feasible to sufficiently cool vanadium alloy coils in a reactor environment.

TABLE OF CONTENTS

	Page
ABSTRACT	i
List of Figure Captions	iii
I. Introduction	1
II. Fast Magnetosonic Wave Theory	5
A. Wave Propagation and Absorption	5
B. The Influence of the Launching Structure and Mode Conversion on the Excited Mode Wave Spectrum	13
III. Reactor Startup Model	26
IV. RF Circuit Coupling to Magnetosonic Waves in the Tokamak Reactor	58
A. Introduction	58
B. Cavity Backed Aperture Antenna	61
C. Coil Antenna	74
V. The Radiofrequency Heating System for NUWMAK	78
A. Introduction	78
B. The Wave Generating System	80
C. The RF Transmission System	84
D. The Coupling System	111
1. Cavity Backed Aperture Antenna	112
2. Coil Antenna	121
E. Prime Power Requirement for the Overall RF System	125
VI. Summary	128
Acknowledgements	133

List of Figure Captions

Page

Chapter II

Fig. 1. Local fast magnetosonic dispersion relation for a plasma profile given by $n_e = 2n_{D_2} = 2n_T = 4 \times 10^{14}\ (1-(r/a)^2)\text{cm}^{-3}$, $T_e = T_i = 5\ (1 - 0.9(r/a)^2)^2$ keV, $k_{\parallel} = 10\ \text{m}^{-1}$, f = 92 MHz and B_0 = 60 kG on axis. 10

Chapter III

Fig. 1. Magnetosonic wave heating for RF power levels of 50, 70, 80 and 100 MW applied for 3 sec. 41

Fig. 2. Magnetosonic wave heating for RF power levels of 50, 100, 125, 150 and 200 MW applied for 1 sec. 42

Fig. 3. Magnetosonic wave heating to reactor ignition and alpha power deposited in the electrons for an RF pulse of 1 sec. at 175 MW. 43

Fig. 4. $k_{\perp}$ averaged over the resonance zone of each species for an RF power level of 175 MW. 44

Fig. 5. Deuterium and tritium resonance widths for an RF power level of 175 MW. 45

Fig. 6. Magnetosonic wave electric field $|E_+|$ for an RF power level of 175 MW. 46

Fig. 7. RF power absorbed by each species for a total input power of 175 MW. 47

Fig. 8. Electron energy balance terms for an RF power level of 175 MW for a 1 sec. pulse. 48

Fig. 9. Ion energy balance terms for an RF power level of 175 MW for a 1 sec. pulse. 49

Fig. 10. RF power absorption of each species for a pulse ramped linearly from 0 to 75 in 3 sec. and then constant 75 MW for 1 sec. During the first 3 secs, the plasma current rises linearly from 1 to 6.5 MA. 53

Fig. 11. Evolution of plasma current and minor radius during the plasma current rise for a 3 sec. operation. 54

		Page
Fig. 12.	Magnetosonic wave heating to ignition for an RF pulse ramped from 0 to 75 MW during the 3 sec. plasma current rise and then constant 75 MW for an additional 1 sec.	56
	Chapter IV	
Fig. 1.	Illustration of the effect of a conducting wall on a half-wavelength dipole antenna.	59
Fig. 2.	Schematic of proposed TE_{101} mode cavity antenna system mounted on a torus.	62
Fig. 3.	Resonance curve of the C and A dimensions of the cavity antenna at 92 MHz.	63
Fig. 4.	Schematic of antenna cavity and reactor fields.	64
Fig. 5.	Schematic of a center-fed half-wavelength dipole antenna.	74
	Chapter V	
Fig. 1.	Schematic of HV Power Supply and Transmitter for One RF Module in NUWMAK	83
Fig. 2.	Coax peak power ratings as a function of pressure and gas type. (Reproduced from Ref. 5).	87
Fig. 3.	A typical coaxial line.	88
Fig. 4.	Attenuation correction factor vs. temperature for coax. (Reproduced from Ref. 5).	91
Fig. 5.	Coaxial vacuum window configuration (side-view).	94
Fig. 6.	Power reflection coefficient as a function of window length. $\varepsilon_r = 6.5$ for BeO.	96
Fig. 7.	Radial profile of RF dissipation in coaxial BeO windows.	100
Fig. 8.	Cross-sectional view of NUWMAK.	102
Fig. 9.	Fundamental multipactor breakdown region; plate separation = 6 cm and $-60° < \theta_o < 18°$, k = 3.	109
Fig. 10.	Wedge coaxial cavity and coax feed mounted on a torus.	113

		Page
Fig. 11.	Exact and approximate TE_{101} resonance curves for the poloidal and toroidal dimensions of the outer cavity at 92 MHz.	116
Fig. 12.	Aperture array on outer cavity viewed from major axis.	118
Fig. 13.	Cross-section of NUWMAK between TF coils (with inner RF cavity).	120
Fig. 14.	Top view of NUWMAK.	122
Fig. 15.	Base design of RF coils coupling array in NUWMAK.	123

I. Introduction

It is clear that a supplementary heating system will be required to heat a tokamak plasma from the efficient Ohmic heating limit of a few keV to the 7-10 keV required for reactor ignition conditions. In this paper we consider the scaling of fast magnetosonic wave heating at the second ion cyclotron harmonic for the NUWMAK tokamak reactor. While a considerable amount of theoretical[1-10] and experimental[11-15] work has been done on recent and current tokamaks including PLT, ATC, TFR, T-4, and ST, relatively little work has been done on the scaling to reactor size machines[16-20]. This work is directed toward clarifying the reactor heating problem and discussing the hardware associated with coupling to a tokamak.

The work starts with a review of fast magnetosonic wave theory including hot plasma dispersion, absorption, eigenmode density and mode conversion processes. In a reactor the competition between the dense spectrum of eigenmodes and the mode conversion from fast magnetosonic waves to electrostatic ion Bernstein modes near the second harmonic resonance surface with the consequent decrease in "Q" is a most important consideration. At the two extremes one has either a dense spectrum of modes which can be excited with some selectivity provided by the launching structure or a plane wave picture where all the power launched by the antenna is essentially absorbed in a single pass via mode conversion. A brief discussion of this aspect is made and its implication in terms of the coupling structure is presented.

Next, the problem of reactor startup utilizing fast magnetosonic wave heating is addressed. A spatially-averaged, time-dependent

transport code which simultaneously solves the ion and electron energy balance equations is presented. A local weak damping approximation is used to derive the RF heating term in the equations. The code includes alpha-particle and RF heating terms, species equilibration, and conduction, convection, Bremsstrahlung, and synchrotron losses. It is found that 80 MW of power absorbed by the plasma for a period of three seconds is sufficient to increase the alpha particle heating rate so that the plasma ignites and reaches its equilibrium operating conditions in a sufficiently short time.

In order to provide the power assumed to be propagating in the machine in the startup model, the problem of efficient coupling from external RF generators to desired fast magnetosonic wave modes in the plasma is addressed. The coupling structure must match impedance levels between the generator and plasma waves so that a maximum power transfer with low external losses is achieved. This must be done without exceeding RF breakdown conditions. The launching structure must be compatible with the high neutron flux emanating from the plasma and the access constraints imposed by a high field, high density, minimum size tokamak reactor. Finally, a summary is presented.

References

1. J. Adam and A. Samain, Association Euratom - C.E.A. Report EUR-CEA-FC-579 (Fontenay-aux-Roses, 1971); J. Adam, Report EUR-CEA-FC-711 (Fontenay-aux-Roses, 1973).

2. F. W. Perkins, Symposium on Plasma Heating and Injection, Varenna, Italy (1972).

3. R. R. Weynants, Phys. Rev. Letters 33, 78 (1974).

4. D. G. Swanson and Y. C. Ngan, Phys, Rev. Letters 35, 517 (1975).

5. D. G. Swanson, Phys. Rev. Letters 36, 316 (1976).

6. T. H. Stix, Nuclear Fusion 15, 737 (1975).

7. R. Klima, A. V. Longinov, and K. N. Stepanov, Sov. Phys. Tech. Phys. 21, 409 (1976).

8. J. E. Scharer, B. D. McVey, and T. K. Mau, Nuclear Fusion 17, 297 (1977); J. E. Scharer, B. D. McVey, and T. K. Mau, Proceedings 3rd International Meeting on Theoretical and Experimental Aspects of Heating of Toroidal Plasmas (C.E.A., Grenoble, 1976) Vol. 1, p. 79; J. E. Scharer, T. K. Mau, D. T. Blackfield and B. D. McVey, Proc. Seventh European Conference on Controlled Fusion and Plasma Physics, p. 145, Lausanne, September, 1975.

9. J. Jacquinot, B. D. McVey, and J. E. Scharer, Phys. Rev. Lett. 39, 88 (1977).

10. F. W. Perkins, Nuclear Fusion 17, 1197 (1977).

11. J. Adam, M. Chance, H. Eubank, W. Getty, E. Hinnov, W. Hooke, J. Hosea, F. Jobes, F. Perkins, R. Sinclair, J. Sperling, and H. Takahashi, Proceedings 5th International Conference on Plasma Physics and Controlled Nuclear Fusion Research (IAEA, Vienna, 1975) p. 65.

12. V. L. Vdovin, N. V. Shapotkovskii, and V. D. Rusanov, Proceedings 3rd International Meeting on Theoretical and Experimental Aspects of Toroidal Plasmas (C.E.A. Grenoble, 1976) Vol. 2, p. 349.

13. H. Takahashi, C. C. Daughney, R. A. Ellis, R. J. Goldston, H. Hsuan, T. Nagashima, F. J. Paoloni, A. J. Sivo, and S. Suckewer, Phys. Rev. Letters 39, 31 (1977).

14. V. V. Buzankin, V. A. Vershkov, N. V. Ivanov, I. A. Kovan, V. A. Krupin, I. A. Popov, I. B. Semenov, and Yu. A. Sokolov, Proceedings of the 6th International Conference on Plasma Physics and Controlled Nuclear Fusion Research, (IAEA, Vienna, 1977) p. 61.

15. Equipe TFR, Proceedings 6th International Conference on Plasma Physics and Controlled Nuclear Fusion (IAEA, Vienna, 1977) 39; Proceedings 3rd International Meeting on Theoretical and Experimental Aspects of Heating of Toroidal Plasmas (C.E.A., Grenoble, 1976) Vol. I, p. 87; Proceedings 3rd Symposium and Workshop on Plasma Heating in Toroidal Devices (Varenna, 1976).

16. J. E. Scharer, R. W. Conn, and D. T. Blackfield, EPRI Report ER-268, (1976).

17. J. Adam and J. Jacquinot, Report EUR-CEA-FC-886, Fontenay-aux-Roses (1977).

18. T. H. Stix, Third Symposium of Plasma Heating in Toroidal Devices, Varenna (1976). PPPL Report-1298.

19. J. C. Hosea, Third Symposium of Plasma Heating in Toroidal Devices, Varenna (1976). PPPL Report-1309.

20. B. W. Reed, O. N. Bowen, H. M. Hill, J. Q. Lawson, W. G. Newman, and A. J. Sivo, PPPL Report-1410 (1977).

II. Fast Magnetosonic Wave Theory

A. Wave Propagation and Absorption

In this section we present the wave propagation, absorption, eigenmode, and mode conversion properties for the fast magnetosonic wave. Early theoretical works by Adam and Samain[1], Perkins[2], and Weynants[3] have presented the basic wave propagation and absorption mechanisms for the mode in the ion cyclotron frequency range (ICRF). The operative absorption mechanisms are cyclotron harmonic damping of the wave by the ions and Landau and transit-time damping of the wave by the electrons. Stix[6] has shown that when cross terms in the dielectric tensor are included in the electron damping calculation that for TFTR parameters the net electron damping is Landau damping and has a value which is half that for the transit time considered separately. We have found from computational studies that this is generally the case for reactor oriented machines.

We now present a brief derivation of the fast magnetosonic wave hot plasma dispersion relation. Assuming an $e^{-i\omega t + i\bar{k}\cdot\bar{r}}$ Fourier component of wave quantities, the wave equation is obtained as $\bar{k} \times (\bar{k} \times \bar{E}) + (\omega/c)^2 \bar{\bar{K}} \cdot E = 0$ where $\bar{\bar{K}}$ is the dielectric tensor as defined in Stix[21]. By noting that in the magnetosonic regime that the Bessel function argument $\lambda_j = k_\perp^2 \rho_j^2/2$ is small for both ion and electron terms, one can obtain a tractable dispersion relation in which first-order finite gyroradius effects are included by expanding to first order in λ_j. Further, the K_{zz} component of the dielectric tensor is so large compared to other elements involving the z component that the dispersion relation can be obtained to a very good approximation by expanding the 2 x 2 minor of the K_{zz} component. The dispersion

relation then becomes ($k_\perp = k_x$, $k_\parallel = k_z$) to the fourth order in $k_\perp$

$$\begin{vmatrix} (\omega/c)^2 K_{xx} - k_\parallel^2 & (\omega/c)^2 K_{xy} \\ (\omega/c)^2 K_{yz} & (\omega/c)^2 K_{yy} - k_\parallel^2 - k_\perp^2 \end{vmatrix} = 0 \qquad (1)$$

where

$$K_{xx} = 1 + \sum_{\alpha=i,e} (\omega_{p\alpha}^2/2\omega k_\parallel v_\alpha)(Z_1^\alpha + Z_{-1}^\alpha) - k_\perp^2 \sum_{\alpha=i,e} (\omega_{p\alpha}^2 v_\alpha/4\omega k_\parallel \omega_{c\alpha}^2)(Z_1^\alpha + Z_{-1}^\alpha - Z_2^\alpha - Z_{-2}^\alpha),$$

$$K_{yy} = K_{xx} + k_\perp^2 \sum_{\alpha=i,e} (\omega_{p\alpha}^2 v_\alpha/\omega k_\parallel \omega_{c\alpha}^2)\,[Z_0^\alpha - 1/2(Z_1^\alpha + Z_{-1}^\alpha)],$$

$$K_{xy} = -K_{yz} = -i \sum_{\alpha=i,e} (\omega_{p\alpha}^2/2\omega k_\parallel v_\alpha)(Z_1^\alpha - Z_{-1}^\alpha) + ik_\perp^2 \sum_{\alpha=i,e} (\omega_{p\alpha}^2 v_\alpha/4\omega k_\parallel \omega_{c\alpha}^2)(2Z_1^\alpha - 2Z_{-1}^\alpha -$$

$$Z_2^\alpha + Z_{-2}^\alpha)$$

and Z_ℓ^α denotes the Fried and Conte plasma dispersion function $Z((\omega + \ell\omega_{c\alpha})/k_\parallel v_\alpha)$. The dispersion relation then includes wave absorption due to finite ion gyroradius effects, cyclotron damping, and electron transit-time damping (a factor of 2 greater than the resulting Landau damping obtained from the 3 x 3 dispersion relation).

The power absorbed by the ions and electrons per unit volume can be obtained in the weak damping limit in a manner following Stix[6] as $p = \omega\bar{E}^* \cdot (\bar{\bar{K}}^a \cdot \bar{E})/2(\text{watt/cm}^3)$ where $\bar{\bar{K}}^a$ is the anti-Hermitian part of the dielectric tensor. The finite ion gyroradius damping term becomes

$$p_i = \pi^{1/2} \varepsilon_o \omega_{pi}^2 \mathrm{Re}(\lambda_i)^{\ell-1} |E_+|^2 e^{-((\omega - \ell\omega_{ci})/k_\parallel v_i)^2/4k_\parallel v_i} \qquad (2)$$

In a similar way the electron Landau damping term can be obtained from the anti-Hermitian part of the K_{yy}, K_{yz}, K_{zy}, and K_{zz} elements and written as

$$P_e = \pi^{1/2}\varepsilon_o(\omega_{pe}/\omega_{ce})^2 k_\perp^2 |E_y|^2 v_e e^{-(\omega/k_\parallel v_e)^2/4k_\parallel} . \qquad (3)$$

In the above equations, ℓ is the harmonic number $\omega = \ell\omega_{ci}$, E_+ is the left-hand circularly polarized electric field component rotating in the sense of the ions, and E_y is the rectangular component of the electric field. $|E_+|^2 = |1-\chi|^2|E_y|^2 = |1+x^2|^{-1}|E_y|^2$ where

$\chi = iE_x/E_y \simeq \dfrac{-i\ K_{xy}}{K_{xx} - n_\parallel^2}$ is the polarization factor for the second harmonic and

$$x^2 = 3\pi^{1/2}\ k_\perp^2 v_\perp^2/(8\ k_\parallel v_i \omega_{ci}) \ .$$

The ion cyclotron harmonic absorption term occurs in a region of finite width in the tokamak minor cross section due to the thermal effects and the 1/R variation of the toroidal magnetic field. For the second harmonic, this width is $\Delta = k_\parallel\ v_i R/\omega_{ci}$. It is further assumed that the energy deposited in the slab is uniformly distributed over the circular flux surface intersecting the radial element on the slab due to the rotational transform.

To take rotational transform effects into account in the ion heating expressions we write

$$B_T = \frac{B_o}{1 - \frac{r}{R}\sin\theta} \qquad (4)$$

where B_o is the B-field on axis.

For a large aspect ratio device, we may approximately write

$$B_T \approx B_o \left(1 + \frac{r}{R} \sin\theta\right) . \tag{5}$$

By averaging over a flux surface, we can define

$$\langle p_i(r)\rangle_\theta = \frac{1}{2\pi} \int_0^{2\pi} p_i(r,\theta)\, d\theta \tag{6}$$

where

$$\langle p_i(r)\rangle_\theta = \frac{\pi^{1/2}\varepsilon_o\, \omega_{pi}^{\,2}\, \lambda_i^{\,\ell-1}}{4\, k_\parallel v_i} |E_+|^2\, e^{-\gamma^2 \sin^2\theta} \tag{7}$$

and

$$\gamma^2 = \frac{\ell^2 \omega_{cio}^2\, r^2}{R^2\, k_\parallel^{\,2}\, v_i^{\,2}} \text{ , and } \omega_{cio} = \frac{q\, B_o}{m_i} .$$

Then equation (6) yields

$$\langle p_i(r)\rangle_\theta = \frac{\pi^{1/2}\varepsilon_o\, \omega_{pi}^{\,2}}{4\, k_\parallel\, v_i}\, \lambda_i^{\,\ell-1}\, I_o\left(\frac{\gamma^2}{2}\right)\, |E_+|^2 \tag{8}$$

where we have assumed that $|E_+|^2$ is not an explicit function of θ. For $\gamma^2/2 \gg 1$ we find that

$$\langle p_i(r)\rangle_\theta = \varepsilon_o(\omega_{pi}^{\,2}/\omega_{cio})\, (R/r)\, \mathrm{Re}(\lambda_i)^{\ell-1}\, |E_+|^2/4\ell . \tag{9}$$

Note that this provides a strong peaking of the energy deposition to the ions at the plasma core. By integration over the tokamak cross section these equations are adapted to a time-dependent model for the startup calculation in NUWMAK.

Figure 1 shows the dispersion relation for the magnetosonic wave for NUWMAK parameters. The parameter $\lambda_D = k_\perp^2 \rho_D^2/2$ (D = deuterium) is plotted as a function of the minor radius on the horizontal plane of the machine with parabolic density and temperature profiles assumed over the cross section. The parallel wavelength ($k_\parallel = 10\ m^{-1}$) is assumed constant over the cross-section and a peak temperature of $T_i = T_e = 5$ keV and peak density $n = 4 \times 10^{14}/cm^3$ is assumed on the axis with values at the plasma edge ($r = 1.25$ m) dropping to one percent of those on axis. The wave frequency is 92 MHz which corresponds to second or third cyclotron harmonic resonance for deuterium or tritium at 60 kG on axis, respectively.

From the dispersion curve in Fig. 1, one notes that the imaginary part of the roots for λ_D corresponds to absorption, mode conversion, and evanescent regions. The roots labelled F correspond to the fast magnetosonic mode and those labeled B correspond to an electrostatic ion Bernstein branch. In the region where the two roots coalesce, some of the wave power propagating in the fast wave branch can be coupled into the backward wave mode ion Bernstein branch and some can be transmitted through. Works by Swanson, Ngan, Scharer, McVey, Mau, Jacquinot and Perkins[4,5,8,9,10,22] have treated this problem. No exact model has been put forth that will describe the amount of wave energy which tunnels through and is absorbed by cyclotron harmonic absorption and the amount of incident fast wave energy that is mode converted for

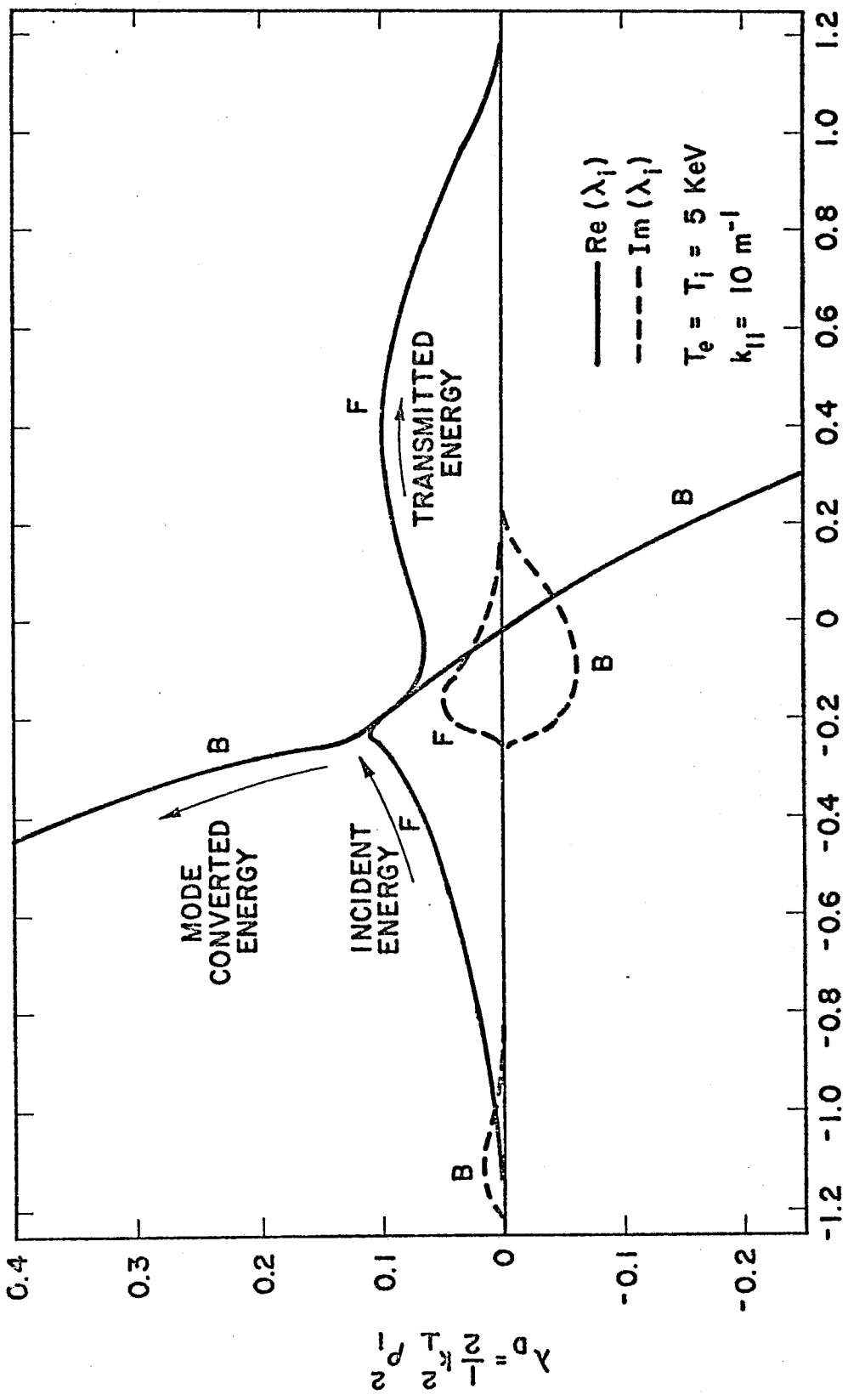

Fig. 1. Local fast magnetosonic dispersion relation for a plasma profile given by $n_e = 2n_D = 2n_T = 4 \times 10^{14}$ $(1-(r/a)^2)cm^{-3}$, $T_e = T_i = 5\ (1 - 0.9(r/a)^2)^2$ keV, $k_{\parallel} = 10\ m^{-1}$, f = 92 MHz and $B_o = 60$ kG on axis.

all values of $k_{\parallel}$ and plasma parameters. However, in the limit where $k_{\perp}^2\rho_i/k_{\parallel} >> 1$, computational results predict that fast wave energy incident from the high magnetic field side of the cyclotron harmonic resonance is essentially all converted to the backward wave ion Bernstein mode and wave energy incident from the low magnetic field side is completely reflected from the cyclotron harmonic resonance zone. In this limit the eigenmode description of fast magnetosonic waves is not appropriate and wave energy propagating along the fast wave branch from the high field side of resonance can be visualized as being completely absorbed in a single pass via mode coupling to the more strongly damped ion Bernstein mode.

Perkins[10] has shown that once the wave energy flows along the ion Bernstein branch, the effect of the poloidal component of the magnetic field provided by the rotational transform from the Ohmic heating current greatly modifies the local $k_{\parallel}$ and strong absorption can result. McVey and Scharer[22] have done ray tracing studies incorporating this effect and obtained a dispersion relation for the ion cyclotron range of frequencies (ICRF) which accurately describes the dispersion of the ion Bernstein branch for all ranges of the parameter $\lambda_i \lesssim 10$. The results show that strong ion or electron absorption of waves launched from the high field region can occur in the low $k_{\parallel}$ regime, dependent on the orientation of the initial ray direction at the plasma edge and its location in the vertical profile.

For sufficiently large $k_{\parallel}$ (20 m^{-1} for NUWMAK parameters), the mode conversion process can be neglected and fast wave tunneling

through the second ion cyclotron harmonic absorption region is possible. However, even though the weak absorption limit $|k_i|/|k_r| \ll 1$ is locally valid in this regime, the harmonic absorption width in a reactor, Δ, is sufficiently large so that the wave is substantially damped in a single pass through the resonance zone. This lowers the wave Q in the machine and makes an eigenmode description of the fields inadequate.

Nevertheless, we adopt the eigenmode description of wave fields in our reactor study due to the relative ease of formulating the coupling problem. The final verdict on the role of mode conversion in absorption in the ICRF range awaits more detailed experimental measurement on scaling as the size of tokamaks is increased.

A further condition that must be met in order to have high Q eigenmodes is that the impurity proton concentration which is at the fundamental ion cyclotron resonance must not exceed $n_H/n_D = \beta_i$ [10] so that fundamental proton absorption or mode conversion near the two-ion hybrid resonance does not dominate the deuterium cyclotron harmonic absorption and strongly reduce the mode Q. As a practical matter for a reactor such as NUWMAK the proton concentration should not exceed fractions of a percent ($n_H/n_D = 0.003$).

Finally, if mode conversion processes are ultimately shown to dominate the absorption in a reactor, the resultant spatial and plasma species absorption rates can be incorporated in the time dependent transport code for startup calculations in a similar manner as we have done for the case of fast wave eigenmode absorption. However, the formulation of the coupling problem and calculation and antenna radiation impedance for the wave absorption via mode conversion will be much more formidable.

II.B. The Influence of the Launching Structure and Mode Conversion on the Excited Mode Wave Spectrum.

Fast magnetosonic wave experiments on the ST, ATC, TFR, T-4, TM-1-VCh, PLT, MACROTOR, CALTECH, ERASMUS, and TEXAS TECH tokamaks have observed high Q eigenmodes under appropriate conditions at the second harmonic of the ion cyclotron frequency. When this occurs an enhanced radiation resistance of the antenna is present and the coupling from the RF generator to plasma waves is very efficient. In this section we determine the possible dense spectrum of eigenmodes in the plasma and consider the influence of wave processes such as mode conversion and the spectrum of the launching structure in determining the composite heating picture and loading of the antenna.

Stix[18] and Hosea[19] have considered the density of eigenmodes in a cold homogeneous cylindrical plasma such that the axial RF magnetic field varies as $B_z \sim J_m(k_r r) \exp(im\theta + in\phi - i\omega t)$ where m is the poloidal mode number, $n = k_{\parallel} R$ is the toroidal mode number, and k_r is the radial wave number. Stix calculates the density of eigenmodes when the radial (μ), azimuthal (m), and toroidal (n) indices are varied assuming a perfectly conducting wall at radius r=a. The boundary conditions determine that eigenmodes appear whenever $k_r a \simeq \pi(\mu + |m/2|)$ where μ and m are the radial and poloidal mode numbers. If one lets $\nu = \pi(\mu + |m/2|) > 1$, then eigenmodes appear at half-integral values of ν with a $(2\nu-1)$ multiplicity due to the various combinations of μ and m yielding the same ν. By integrating over the values of ν and n, subject to the approximate cold plasma dispersion relation,

$$k_{\perp}^2 + \left(\frac{\omega + \omega_{ci}}{\omega_{ci}}\right) k_{\parallel}^2 = (\omega/v_A)^2 \ , \qquad (10)$$

Stix obtains the total number of propagating modes as

$$N = \frac{2}{3\pi^2} \left(\frac{\omega + \omega_{ci}}{\omega_{ci}}\right)^{1/2} a^2 R \left(\frac{\omega}{v_A}\right)^3 \tag{11a}$$

where R is the major radius and v_A is the Alfvén speed. The mode separation $d\omega$ necessary to increase N by 1 is

$$d\omega/\omega = dN/3N = 1/3N \tag{11b}$$

For reactors the size of NUWMAK with a = 1.25 m, R = 5.0 m, $\bar{n}_e$ = $2 \times 10^{14}/cm^3$, B_o = 60 kG, and $\omega = 2\omega_{ci}$ the separation in eigenmode frequencies is about one part in 4.6×10^4 when compared to the second ion cyclotron harmonic for deuterium. The argument then follows that the antenna can provide a poloidal and toroidal resolution of 100 with individual Q's of order 100 so that about 5 modes are simultaneously excited. If too many modes are simultaneously excited, the cumulative field intensity is in phase near the antenna, but due to radial phase shifts can be out of phase and destructively interfere at regions in the plasma core. This can lead to undesirable surface heating of the plasma.

The above analysis assumed that all mode indices were equally excited and that the excitation spectrum of the antenna provided a combined poloidal and toroidal resolution of about 100. A more complete picture of an ideal launching structure would include the following considerations. First, the launching structure would have a Fourier spectrum which peaks at fairly low values of m and becomes negligible for $|m| > 3$. This greatly reduces the number of modes over which substantial RF power is distributed and thus the effective

density of modes. Secondly, the low $k_{\parallel} = n/R$ modes as we have seen are those which are most readily mode converted and have an equivalent low Q. If competition for power density among the mode spectrum takes place, the strongly mode converted "modes" might receive the least amount of wave power and the higher Q eigenmodes corresponding to the higher $k_{\parallel}$ part of the spectrum would receive most of the wave power due to their enhanced radiation resistance.

Hosea[19] has looked at the mode density question for larger machines and noted that the spectrum is quite dense for higher $k_{\parallel}$ modes but that it is relatively sparse for lower $k_{\parallel} \approx 0$ modes. He suggests an antenna structure which preferentially excites low $k_{\parallel}$ modes and uses frequency tracking and gas puffing for density control to excite the desired modes. It would appear that due to the preferential mode conversion process for low $k_{\parallel}$ modes and the higher density of modes for larger $k_{\parallel}$, the presence of low $k_{\parallel}$ eigenmodes and selective tracking of higher $k_{\parallel}$ eigenmodes in a reactor is very difficult technologically and somewhat academic. The resolution of this question awaits further detailed experimental evidence on the mode conversion process and eigenmode scaling in larger tokamaks such as PLT and TFTR.

Hosea further points out that density fluctuations in the plasma can effectively scan over modes so that tracking a single mode becomes very difficult. It should also be kept in mind that plasma heating via mode conversion processes can offer the advantage of a well defined process dominating cyclotron harmonic absorption. One possible disadvantage is the reduced radiation resistance for absorption via mode conversion processes when compared with that where the dominant absorption is via cyclotron harmonic damping for high Q eigenmodes.

For reactor size machines longer resonant half-wavelength antennas can be considered rather than the electrically short coils used in present day machines. This will act to enhance the radiation resistance and counter the expected decrease due to mode conversion processes providing efficient coupling of the RF power to the fast magnetosonic wave for plasma heating.

We now calculate the mode spectrum and spacing for fast magnetosonic waves in a tokamak. Due to the weak rotational transform effects in a tokamak compared to the circumference, we adopt the cold, uniform plasma-filled guide problem discussed by Bernstein and Trehan[23]. For waves in the ion cyclotron frequency range the TE mode solution ($E_z = 0$) is derivable from the axial magnetic field component given by

$$H_z = H_1 J_m(k_r r) e^{im\theta + in\phi - i\omega t} \tag{12}$$

where H_1 is an amplitude coefficient, k_r is the radial wavenumber, m is the poloidal mode number and $n = k_{\parallel} R$ is the toroidal mode number corresponding to an eigenmode. The dispersion relation is given by

$$k_r = [k_{\parallel}^4/S - 2k_0^2 k_{\parallel}^2 + k_0^4 RL/S]^{1/2} \cdot [k_0^2 - k_{\parallel}^2/S]^{-1/2} \tag{13}$$

where S, R, L, and D are defined in the Stix[21] notation and $k_0 = \omega/c$. For our case $S = \omega_{pi}^2/(\omega_{ci}^2 - \omega^2)$, $RL/S = \omega_{pi}^2/\omega_{ci}^2$, and $D/S = -\omega/\omega_{ci}$.

The θ component of the electric field which is the tangential electric field at the edge of the cylindrical column can be calculated via Maxwell's equations and is

$$E_\theta = i\omega \mu_0 H_1 [a_2(m/r) J_m(k_r r) + a_1 k_r J_m'(k_r r)] \tag{14}$$

where $a_1 = -k_r^{-2} = (k_\parallel^2/S - k_0^2)/\Lambda$ and $a_2 = (D/S)k_0^2/\Lambda = (-\omega/\omega_{ci})k_0^2/\Lambda$ are polarization factors and $\Lambda = k_\parallel^4/S - 2k_0^2k_\parallel^2 + k_0^4RL/S$. Applying the boundary condition for a plasma filled guide with a conducting boundary $E_\theta\ (r=a) = 0$ yields

$$a_2(m/a)\ J_m(k_ra) + a_1\ k_r\ J_m'(k_ra) = 0$$

or

$$k_ra\ J_m'(k_ra)/J_m(k_ra) = m(\omega/\omega_{ci})k_A^2/(k_\parallel^2 - k_A^2 - k_\parallel^2(\omega/\omega_{ci})^2) \qquad (15)$$

where $k_A = \omega/v_A$ and v_A is the Alfvén velocity.

We now investigate the eigenfrequencies and frequency spacing as the radial (μ), azimuthal (m), and toroidal (n) indices are varied. We assume that the wave launching structure and large reactor size satisfy the following conditions: 1) $k_ra >> m$, 2) $k_r \simeq k_A >> k_\parallel$, and 3) $\omega \simeq 2\omega_{ci}$. By using the asymptotic form of the Bessel functions

$$\lim_{k_ra >> m} J_m'(k_ra)/J_m(k_ra) \to -\tan(k_ra - \frac{m\pi}{2} - \frac{\pi}{4}) \ ,$$

Eq. (15) can be written in the form

$$k_ra - m\pi/2 - \pi/4 = \mu\pi + m(\omega/\omega_{ci})/(k_ra) \qquad (16)$$

where $\mu > 0$ is the radial eigenvalue related to the number of radial half-wavelengths that fit in the machine.

Since $\tan(\phi) = \tan(\phi - \mu\pi)$ we can write

$$\tan(k_ra - \nu\pi - \pi/4) = m(\omega/\omega_{ci})/k_ra \qquad (17)$$

where $\nu = \mu + m/2$.

We now consider the shift in eigenmode frequencies due to various changes in the mode indices. The smallest shift will be due to a

shift in m and μ while maintaining constant ν and n indices. We note that $|k_r a - \nu\pi - \pi/4| \ll 1$ and let $\Delta k_r = k_{r1} - k_{r2}$. Thus,

$$\Delta k_r a = \Delta m(\omega/\omega_{ci})/(k_r a)$$

and since $$\Delta k_r = \Delta\omega/v_A \simeq \Delta\omega\ k_r/\omega$$

we have

$$\Delta\omega(\mu,m)/\omega\big|_{\nu,n} = \Delta m(\omega/\omega_{ci})/(k_r a)^2 \ , \tag{18}$$

In a similar fashion we obtain

$$\Delta\omega(\mu)/\omega\Big|_{n,m} = \Delta\mu\pi/(k_r a) \tag{19}$$

and

$$\Delta\omega(m)/\omega\Big|_{n,\mu} = \Delta m\pi/(2\ k_r a) \ . \tag{20}$$

For $\Delta\omega(n)/\omega\Big|_{\mu,m}$ we must use a more accurate dispersion relation for finite $k_{\shortparallel} = n/R$. The cold plasma dispersion relation can be written

$$(\pi\nu/a)^2 + ((\omega + \omega_{ci})/\omega_{ci})(n/R)^2 = (\omega/v_A)^2 \tag{21}$$

where the second term is small for our regime of interest. Thus

$$2\ \omega\ \Delta\ \omega \simeq v_A^2\ ((\omega + \omega_{ci})/\omega_{ci})\ 2n\Delta n/R^2$$

and utilizing $v_A \simeq \omega/k_r$, we obtain

$$\Delta\ \omega(n)/\omega\Big|_{\mu,m} = \Delta n((\omega + \omega_{ci})/\omega_{ci})\ n/(k_r R)^2 \ . \tag{22}$$

For the NUWMAK tokamak with $\bar{n} = 2 \times 10^{14}/cm^3$, $B_0 = 60$ kG, $R = 5$ m, and $a = 1.25$ m the previous results yield

$$\Delta\omega(\mu,m)/\omega \Big|_{\nu,n} = 1.6 \times 10^{-4}\, \Delta m \ , \tag{23}$$

$$\Delta\omega(\mu)/\omega \Big|_{n,m,} = 2.8 \times 10^{-2}\, \Delta\mu \ , \tag{24}$$

$$\Delta\omega(m)/\omega \Big|_{\mu,n} = 1.4 \times 10^{-2}\, \Delta m \ , \tag{25}$$

and

$$\Delta\omega(n)/\omega \Big|_{\mu,m} = 3.9 \times 10^{-3}\, \Delta n \ . \tag{26}$$

The above results show the spacing between adjacent eigenmodes for the variation of a single mode index. Note that since the dispersion relation for Alfvén waves varies as $\omega^2 = k_r^2 v_A^2 \sim n_e^{-1}$ that $\Delta\omega/\omega = -\Delta n_e/2n_e$ and that the above expressions can be interpreted as the shift in density required to shift to an adjacent mode. It is noted that the density fluctuations in a tokamak discharge should ultimately be taken into account in obtaining the time-average heating and absorption rates for ion cyclotron harmonic waves. We now look at ways in which the launching structure and mode conversion processes tend to limit the spectrum of excited modes.

There are currently two main processes being considered in the propagation and absorption of wave energy in a tokamak. The first involves ion cyclotron harmonic absorption near the second harmonic resonance. In today's machines this can lead to high Q eigenmodes with weak absorption processes. As larger, more dense, and hotter plasmas are created suitable for a reactor device the second process of mode conversion from fast magnetosonic wave modes to ion Bernstein modes is expected to become more substantial. An adjustment of the $k_{\parallel}$ spectrum is then required if one wishes to insure that the wave is absorbed by ion cyclotron harmonic processes. Computations by McVey[22] show that $k_{\parallel}$ must be increased to 20 m^{-1} in a reactor device in order that mode conversion processes can be neglected and that the local weak damping description is valid. By increasing $k_{\parallel}$, the width $\Delta = k_{\parallel} v_i R/\omega_{ci}$ of the cyclotron harmonic absorption zone is substantially increased so that even though the weak damping limit ($k_i/k_r \ll 1$) is satisfied locally, the cumulative effect over the whole absorption zone is such as to strongly damp the wave and yield a low Q situation. As mentioned earlier, this means that efficient coupling to the cavity requires a transformation of impedance levels such as that found in the aperture coupled cavity or the use of resonant half-wavelength coil antennas.

We now consider the desirable properties of a launching structure so that efficient wave coupling and heating in a tokamak can be achieved.

With regard to the poloidal spectrum, we note that the spatial heating profiles for an eigenmode vary as $J^2_{m-1}(k_r r)$ so that an antenna which excites a low m spectrum is desirable to provide core heating and avoid edge heating of less well confined plasma particles. As an example, the expression for the current in a coil which covers half the poloidal angle and is of uniform amplitude and phase is $I(\theta) = I_0(H(\theta + \pi/2) - H(\theta - \pi/2))$ where the H stands for the Heaviside function. The current can be represented as

$$I(\theta) = \sum_{m=0}^{\infty} I_m e^{im\theta}$$

where the Fourier coefficient can be calculated as $I_m = \frac{1}{2\pi} \int_0^{2\pi} I(\theta) e^{-im\theta} d\theta$.

Thus

$$I_m = \begin{cases} 1/2 \ (m=0) \\ \frac{1}{\pi |m|} \ m \text{ odd; } m = \pm 1, \pm 3, \pm 5, \ldots \\ 0 \quad m \text{ even; } m = \pm 2, \pm 4, \pm 6, \ldots \end{cases}$$

Since the excited power is proportional to I_m^2 for slowly varying radiation resistance, we can assume that most of the power launched will be in the $|m| \leq 3$ part of the spectrum. It should be noted that the above current excitation could only be excited with a poloidal array of properly phased, electrically short ($\ell << 0.1\lambda$) current elements. If a resonant half-wavelength antenna were used, the cosine-shaped exciting current amplitude about the feed point would produce substantially more power in the higher m part of the spectrum.

For the toroidal spectrum, we assume that a peak at $k_{\parallel} = 20\ m^{-1}$ is excited to insure heating via finite ion gyroradius effects at the

second harmonic resonant zone. A plasma density profile which is sufficiently sharp at the edges is assumed so that the wave evanescent zone is not appreciable and the wave propagates over most of the plasma cross section. We assume a toroidal array of an even number of elements (N_A) with a 180° time-phase shift between successive elements spaced $2\pi R/N_A$ apart. The toroidal current distribution is given by

$$I(\phi) = \sum_{n=0}^{\infty} I_n e^{in\phi} \qquad \phi = z/R$$

where

$$I_n = (2\pi)^{-1} \int_0^{2\pi} I(\phi) e^{-in\phi} d\phi$$

The toroidal Fourier spectrum is given by the well-known form

$$I_n = \sin((2n - N_A)\pi/2)/(2\pi\sin((2n - N_A)\pi/2N_A)). \qquad (27)$$

The spectrum peaks at $n = k_{\parallel}R = (2p+1)N_A/2$ where p is an integer and has a width $\Delta k_{\parallel}/k_{\parallel 0} = 2/N_A$ corresponding to $\Delta n = 2$ for large N_A.

We now calculate the number of modes for which an appreciable Fourier spectrum excitation coefficient exists.

$$N_E = \int_{\nu_{min}}^{\nu_{max}} D(\nu) d\nu \int_{n_{min}}^{n_{max}} dn \qquad (28)$$

where $D(\nu)$ is a degeneracy factor taking into account different combinations of m and μ for the same ν.

If only $|m| = 3$, 1, and 0 modes are appreciably excited we have $D(\nu) = 5$. The width of the n spectrum is $\Delta n = 2$ about the peak and we have two regions of $k_{\parallel}$ below the $k_{\parallel\ max}$ fast wave cutoff for $k_{\parallel 0} = 20\ m^{-1}$. Thus we have

$$N_E = 5 \cdot \Delta\nu \cdot 2 \cdot \Delta n(=2) . \qquad (29)$$

Now the fast wave dispersion relation can be written

$$(\pi\nu/a)^2 + ((\omega + \omega_{ci})/\omega_{ci})(n/R)^2 = (\omega/V_A)^2 \ .$$

For fixed frequency the above dispersion relation yields

$$d\nu = -3(a/\pi)^2(n/\nu)\ dn/R^2. \qquad (30)$$

For $\Delta n = 2$, $n = 100$, $\nu = 110$, $a = 1.25$ m, and $R = 5$ m we have $\Delta\nu = 0.10$. Thus $N_E = 5 \cdot (0.1) \cdot 2 \cdot 2 = 2$ modes. To complete the problem one has to consider the Q of generator and fast wave modes.

The previous calculation shows that the array can substantially reduce the mode spectrum to provide heating. The practical implementation of a large array in the NUWMAK reactor environment is much more difficult. The excited spectrum is likely to be larger than the ideal case previously calculated due to access constraints and a limit on the number of elements in the array.

References

1. J. Adam and A. Samain, Association Euratom - C.E.A. Report EUR-CEA-FC-579 (Fontenay-aux-Roses, 1971); J. Adam, Report EUR-CEA-FC-711 (Fontenay-aux-Roses, 1973).

2. F. W. Perkins, Symposium on Plasma Heating and Injection, Varenna, Italy (1972).

3. R. R. Weynants, Phys. Rev. Letters 33, 78 (1974).

4. D. G. Swanson and Y. C. Ngan, Phys. Rev. Letters 35, 517 (1975).

5. D. G. Swanson, Phys. Rev. Letters 36, 316 (1976).

6. T. H. Stix, Nuclear Fusion 15, 737 (1975).

7. R. Klima, A. V. Longinov, and K. N. Stepanov, Sov. Phys. Tech. Phys. 21, 409 (1976).

8. J. E. Scharer, B. D. McVey, and T. K. Mau, Nuclear Fusion 17, 297 (1977); J.E. Scharer, B.D. McVey, and T.K. Mau, Proceedings 3rd International Meeting on Theoretical and Experimental Aspects of Heating of Toroidal Plasmas (C.E.A., Grenoble, 1976), Vol. 1, pp. 62 and 79.

9. J. Jacquinot, B. D. McVey, and J. E. Scharer, Phys. Rev. Lett. 39, 88 (1977).

10. F. W. Perkins, Nuclear Fusion 17, 1197 (1977).

11. J. Adams, M. Chance, H. Eubank, W. Getty, E. Hinnov, W. Hooke, J. Hosea, F. Jobes, F. Perkins, R. Sinclair, J. Sperling, and H. Takahashi, Proceedings 5th International Conference on Plasma Physics and Controlled Nuclear Fusion Research (IAEA, Vienna, 1975), p. 65.

12. V. I. Vdovin, N. V. Shapotkovskii, and V. D. Rusanov, Proceedings 3rd International Meeting on Theoretical and Experimental Aspects of Toroidal Plasmas (C.E.A., Grenoble, 1976) Vol. 2, p. 349.

13. H. Takahashi, C. C. Daughney, R. A. Ellis, R. J. Goldston, H. Hsuan, T. Nagashima, F. J. Paoloni, A. J. Sivo, and S. Suckewer, Phys. Rev. Letters 39, 31 (1977).

14. V. V. Buzankin, V. A. Vershkov, N. V. Ivanov, I. A. Kovan, V. A. Krupin, I. A. Popov, I. B. Semenov, and Yu. A. Sokolov, Proceedings of the 6th International Conference on Plasma Physics and Controlled Nuclear Fusion Research, (IAEA, Vienna, 1977), p. 61.

15. Equipe TFR, Proceedings 6th International Conference on Plasma Physics and Controlled Nuclear Fusion (IAEA, Vienna, 1977) 39; Proceedings 3rd International Meeting on Theoretical and Experimental Aspects of Heating of Toroidal Plasmas (C.E.A., Grenoble, 1976) Vol. I, p. 87; Proceedings 3rd Symposium and Workshop on Plasma Heating in Toroidal Devices (Varenna, 1976).

16. J. E. Scharer, R. W. Conn, and D. T. Blackfield, EPRI Report ER-268, (1976).

17. J. Adam and J. Jacquinot, Report EUR-CEA-FC-886, Fontenay-aux-Roses (1977).

18. T. H. Stix, Third Symposium of Plasma Heating in Toroidal Devices, Varenna (1976). PPPL Report-1298.

19. J. C. Hosea, Third Symposium of Plasma Heating in Toroidal Devices, Varenna (1976). PPPL Report-1309.

20. B. W. Reed, O. N. Bowen, H. M. Hill, J. Q. Lawson, W. G. Newman, and A. J. Sivo, PPPL Report-1410 (1977).

21. T. H. Stix, The Theory of Plasma Waves (McGraw Hill, New York, 1962).

22. B. D. McVey and J. E. Scharer, Proceedings of the Third Topical Conference on Radiofrequency Plasma Heating, paper D6-1, Pasadena (1978). B. D. McVey, Ph.D. Thesis, University of Wisconsin, 1978. To be published.

23. I. B. Bernstein and S. K. Trehan, Nuclear Fusion 1, 3 (1960).

III. Reactor Startup Model

In this section, we examine various ways in which a reactor may be heated to ignition using RF auxiliary heating. Time varying temperature as well as various heating and loss mechanism curves are obtained by solving the time dependent ion and electron energy balance equations. The RF heating terms are calculated assuming a linear, weak damping, finite Larmor radius theory. A computer point code, based on a spatially independent, "0-D" model is used to solve the energy balance equations. The energy balance equations can be obtained from the Boltzman equation,[1,2,3]

$$\frac{df_j}{dt} + \vec{v} \cdot \vec{\nabla} f_j + \frac{e_j}{m_j} (\vec{E} + \vec{v} \times \vec{B}) \cdot \vec{\nabla}_v f_j = C_j \qquad (1)$$

where C_j is the Fokker-Planck Collision operator.[4]
By taking the second velocity or energy moment of Eq. (1) we obtain

$$\frac{\partial}{\partial t} (\frac{3}{2} n_j kT_j) = - \vec{\nabla} \cdot (\frac{3}{2} kT_j \vec{\Gamma}_j + \vec{Q}_j) - n_j kT_j \vec{\nabla} \cdot \vec{V}_j + n_j e_j \vec{E} \cdot \vec{V}_j + m_j \int v^2 C_j d^3v \qquad (2)$$

$$\vec{Q}_j \equiv \int \vec{v} (\vec{v} - \vec{V}_j)^2 f_j d^3v \qquad (3)$$

where use has been made of both the particle and momentum conservation equations.[1]

Averaging over a magnetic flux surface yields the spatially dependent fluid energy equations for both electrons and ions. For electrons we have

$$\frac{\partial}{\partial t}\left(\frac{3}{2} n_e kT_e\right) = \frac{n_i^2 \langle\sigma v\rangle_{DT}}{4} E_\alpha U_{\alpha e} + \frac{1}{r}\frac{\partial}{\partial r}\left[r\left(Q_e + \frac{3}{2} kT_e \Gamma_e\right)\right]$$

$$- Q_{ei} - P_{rad} + P_{Ohm} + P^e_{INJ} + P^e_{RF} \qquad (4)$$

where a source term for an external injection of power either from RF or beams as well as loss terms from Bremsstrahlung and synchrotron radiation have been added. The radiation loss terms are calculated assuming that a local Maxwellian temperature occurs for the electrons over time scales much longer than the relaxation scale in Eq. (1). The ion equation is

$$\frac{\partial}{\partial t}\left(\frac{3}{2} n_i kT_i\right) = \frac{n_i^2 \langle\sigma v\rangle_{DT}}{4} E_\alpha U_{\alpha i} + \frac{1}{r}\frac{\partial}{\partial r}\left[r\left(Q_i + \frac{3}{2} kT_i \Gamma_i\right)\right]$$

$$+ Q_{ei} + P^i_{INJ} - P_{cx} + P^i_{RF} \qquad (5)$$

where

n_e, n_i = electron and ion densities

T_e, T_i = electron and ion temperatures

$U_{\alpha e}$, $U_{\alpha i}$ = fraction of alpha energy to electrons and ions

Q_{ei} = electron-ion rethermalization term

P_{rad} = Bremsstrahlung, line, recombination and synchrotron radiation losses

P_{Ohm} = Ohmic heating

P^e_{INJ}, P^i_{INJ} = electron and ion heating sources from beams

P_{cx} = charge exchange energy loss

Γ_e, Γ_i = electron and ion particle fluxes

Q_e, Q_i = electron and ion energy conduction terms

P^e_{RF}, P^i_{RF} = electron and ion RF power absorption terms

To obtain the particle flux terms in Eqns. (4) and (5), we examine the particle conservation equation of the zeroth moment of Eq. (1)

$$\frac{\partial n_i}{\partial t} = \frac{1}{r}\frac{\partial}{\partial r}(r\Gamma_i) - \frac{n_i^2 \langle\sigma v\rangle_{DT}}{2} + S_p(r,t) \qquad (6)$$

where $S_p(r,t)$ is the particle source due to neutral beams, pellet injection, or gas puffing and we may write[1]

$$\Gamma_i = D_i \frac{\partial n_i}{\partial r} \qquad (7)$$

$$Q_{e,i} = \chi_{e,i} \frac{\partial (kT_{e,i})}{\partial r} \qquad (8)$$

To obtain the ion-electron equilibration term in Eqns. (4) and (5) we use the classical expression which is in agreement with experimental results,

$$Q_{ei} = \frac{3n_e}{\tau_{ei}} \frac{m_e}{m_i} k(T_e - T_i) , \qquad (9)$$

where τ_{ei} is the electron-ion equilibration time which for the neoclassical banana regime is given by[5]

$$\tau_{ei} = \frac{3\, m_e^{1/2}\, T_e^{3/2}}{4(2\pi)^{1/2} e^4 n_i \ell n\Lambda} . \qquad (10)$$

The Ohmic heating term is evaluated from the neoclassical model

$$P_{Ohm} = E_\phi J_\phi \qquad (11)$$

$$E_\phi = \eta_{nc} J_\phi \qquad (12)$$

where η_{nc} is the neoclassical resistivity obtained from the Spitzer resistivity by[1,6]

$$\eta_{nc} = \eta_{sp} \left[1 - 1.95(r/R)^{1/2} + .95(r/R)\right]^{-1} \tag{13}$$

The energy loss from Bremsstrahlung may be written as[2,5]

$$P_B = 4.8 \times 10^{-31} Z_{eff} n_e^2 T_e^{1/2} \quad \text{watts/cm}^3 \tag{14}$$

with T_e in keV.

The synchrotron loss term is[8]

$$P_{syn} = 1.55 \times 10^{-14}(1 - r_w)^{1/2}[5. + .17(5-\lambda)]^3 \frac{n_e^{1/2} B_\phi^{5/2}}{a^{1/2}} T_e^{2.1} \text{ W/cm}^3 \tag{15}$$

where

r_w = wall reflectivity

T_e in keV

B_T = toroidal field in Tesla

a = minor radius

Finally Eqns. (4) and (5) become[9]

$$\frac{\partial n_e T_e}{\partial t} = 4.28 \times 10^{-11} n_e n_i \frac{(T_i - T_e)}{T_e^{3/2}} + \frac{1}{1.5r}\frac{\partial}{\partial r}\left(r n_e \chi_e \frac{\partial T_e}{\partial r}\right) - \frac{1}{r}\frac{\partial}{\partial r}\left(r n_e V_e T_e\right)$$

$$+ 4.17 \times 10^{15} \{n_D n_T \langle\sigma v\rangle U_{\alpha e} + \bar{E} \cdot \bar{J} + P_{inj}\left(U_{be} + f\left(\frac{E_\alpha}{E_b}\right) U_{\alpha e}\right)$$

$$- P_B - P_S - P_L - P_R\} + P_{RF}^e \tag{16}$$

and

$$\frac{\partial n_i T_i}{\partial t} = -4.28 \times 10^{-11} n_i n_e \frac{(T_i - T_e)}{T_e^{3/2}} + \frac{1}{1.5r}\frac{\partial}{\partial r}\left(r n_i \chi_i \frac{\partial T_i}{\partial r}\right) - \frac{1}{r}\frac{\partial}{\partial r}\left(r n_i V_i T_i\right)$$

$$+ 4.17 \times 10^{15}\left\{n_D n_T \langle\sigma v\rangle_{DT} U_{\alpha i} + P_{cx} + P_{inj}\left(U_{bi} + f\left(\frac{E_\alpha}{E_B}\right)U_{\alpha i}\right)\right\} + P_{RF}^{i} \qquad (17)$$

$T_{e,(i)}$ is the electron (ion) temperature (eV), B_p is the poloidal magnetic field (Gauss), $n_{e,(i)}$ is the electron (ion) density (cm^{-3}), V_i is the ion velocity (cm/ms), J is the toroidal current density (amp/cm^2), E is the toroidal electric field (volt/cm), r is the radius (cm), t is time (ms), $\chi_{e,(i)}$ is the electron (ion) thermal diffusivity (cm^2/ms), η_{NC} is the neoclassical resistivity (ohm-cm), D is the diffusion coefficient (cm^2/ms), $U_{bi,(e)}$ is the fraction of beam energy going to ions (electrons), and f is the fraction of deuterons in the neutral beam which undergo fusion as they slow down in a tritium target plasma. P_B, P_S, P_L, and P_R represent Bremsstrahlung, synchrotron, line and recombination radiation, respectively (watts), P_{cx} is the energy loss due to charge exchange (watts), and E_B is the beam energy, and $P_{RF}^{i,e}$ is the ion (electron) power absorption (watts).

Since the point code is spatially independent, we need to eliminate the gradients in both the conduction and convection terms. Therefore, we may replace the conduction term by[10]

$$\frac{2}{3}\frac{\partial}{\partial r}\left[rn\,\chi\,\frac{\partial T}{\partial r}\right] \rightarrow \frac{nT}{\tau_c} \qquad (18)$$

where τ_c is a characteristic thermal conduction time. For the convection term we have[10]

$$\frac{1}{r}\frac{\partial}{\partial r}\left(r\,nVT\right) \rightarrow \frac{nT}{\tau_D} \qquad (19)$$

where τ_D is a characteristic thermal diffusion time.

Qualitatively, we can replace τ_c and τ_D by

$$\tau_c^{i,e} \rightarrow \frac{a^2}{\chi_{i,e}} \tag{20}$$

$$\tau_D \rightarrow \frac{a^2}{D} \tag{21}$$

where a is the plasma minor radius and D is the diffusion coefficient, and χ is the thermal conduction coefficient.

To calculate D and $\chi_{i,e}$ [11] we first must examine single particle orbits. Particles may travel along magnetic field lines which, if closed and in the absence of drifts, result in no particle losses. However, due to the 1/R variation in the magnetic field, as a particle travels along a given field line it passes through regions of varying field strengths. For a maximum magnetic field strength on that line of B_{max} particles with energy $E < \mu B_{max}$ will be reflected from the high magnetic field regions and become trapped in weak magnetic wells, undergoing periodic motion between reflection points. The bounce frequency for this periodic motion is approximately

$$\omega_b \simeq \frac{v_T}{Rq} \sqrt{2\varepsilon} \tag{22}$$

where $\varepsilon = r/R$ and q is the safety factor

$$q = \frac{rB_T}{RB_p} \quad . \tag{23}$$

Besides this bounce motion, particles also experience an effective gravitational force again caused by the inhomogeneity in the magnetic

field. The resultant drift of particles may be characterized by the velocity

$$V_D \simeq (mv_{\parallel}^2 + \mu B) \frac{B \times \nabla B}{eB^3} \sim \frac{m}{eB} \frac{v_T^2}{R} \tag{24}$$

The combination of bounce motion with drift produces a banana-shaped orbit whose width is given by

$$\Delta r_T \simeq \frac{2V_D}{\omega_b} \simeq 2\rho_\theta \sqrt{\varepsilon} = 2q\ \rho/\sqrt{\varepsilon} \tag{25}$$

where $\rho_\theta = \frac{V_T m}{eB_p}$.

A general particle diffusion coefficient may be defined by $D \sim (\Delta x)^2/\Delta t$ where Δx is the mean spatial step size caused by the scattering process during the time Δt. In the absence of bounce motion and drifts, simple Coulomb collisions produce particle transport. For low β machines, the classical diffusion coefficient is written[11] as

$$D \sim \nu_{ei} \rho^2 \tag{26}$$

where ρ, the gyroradius, is the step size and

$$\nu_{ei} = \frac{4\sqrt{2\pi}\ n_i Z^2\ e^4 \ell n \Lambda}{3\sqrt{m_e}\ T_e^{3/2}} = \text{electron-ion collision frequency.} \tag{27}$$

However, when banana orbits are present in tokamaks, this simple diffusion picture becomes more complicated.

For low ν, the trapped particles have a step size on the order of the banana width rather than their gyroradius. This step size is valid when the collision frequency for the scattering of trapped particles

out of the region of trapped particle velocity space is small compared to the bounce frequency. Since Coulomb collisions are small angle processes we define

$$\nu_{eff} \sim \frac{\nu_{90°}}{(\Delta\theta)^2} \sim \frac{\nu_{ei}}{\varepsilon} \tag{28}$$

The condition for trapped particles to be considered "collisionless" is that

$$\nu_{eff} < \omega_b \text{ or } \nu < \varepsilon^{3/2} V_T/Rq \tag{29}$$

In this "neoclassical" regime, the diffusion coefficient due to trapped particles is

$$D \sim \nu_{eff} (\Delta r_T)^2 f_T \sim \nu \rho^2 q^2 \varepsilon^{-3/2} \tag{30}$$

where f_T is the fraction of trapped particles

$$f_T \equiv \frac{B_{max}}{B_{min}} - 1 \equiv \sqrt{2\varepsilon} \tag{31}$$

For ions in this neoclassical regime $\chi_i \sim D$.

Since plasmas in tokamaks are neither spatially uniform nor Maxwellian, they are subject to both macroinstabilities and microinstabilities. Microinstabilities may be driven by velocity space anisotropy or temperature, density and pressure gradients. Microinstabilities lead to enhanced or "anomalous" transport of which, for tokamaks, the most important kind are those driven by the various gradients present in all tokamaks.

In an inhomogeneous plasma, there is an apparent drift of particles in the $\bar{B}X\nabla n$ direction given by

$$V_d = \frac{T}{eB}\frac{1}{n}\frac{dn}{dr} = \frac{\rho}{r_n} v_T \tag{32}$$

where r_n = effective plasma radius = $(\frac{1}{n}\frac{dn}{dr})^{-1}$.

When there exists an E_θ in the $\overline{B}X\nabla n(\theta)$ direction, with wave number k_θ, this field produces a drift wave with frequency

$$\omega_* = k_\theta V_D \ . \tag{33}$$

Since $\frac{1}{r} < k_\theta < \rho_i^{-1}$ we may have a range of drift frequencies with

$$\omega_{*min} \simeq \frac{V_d}{r} \sim \frac{v_{thi}}{r}\frac{\rho_i}{r_n} \tag{34}$$

$$\omega_{*max} \simeq \frac{V_d}{\rho_i} \sim \frac{v_{thi}}{r_n} \ . \tag{35}$$

There is no energy or momentum exchange between species since E_θ causes both ions and electrons to drift in the $\overline{E}_\theta X\overline{B}$ direction, hence no instability develops. However, various mechanisms exist which may retard one of the drifting species, resulting in a net exchange of either momentum or energy with the drift wave causing an instability to grow. These mechanisms which result in enhanced transport may be classified between various natural frequencies in the plasma ω_{*min}, ω_{*max}, ω_b and the curvature drift frequency $\omega_D \equiv k_\theta v_D$. In tokamaks, we usually have

$$\omega_{Dmin} < \omega_{*min} << \omega_{bi} << \omega_{*max} < \omega_{be} \ .$$

Therefore, we may order the various types of instabilities due to drift waves in order of decreasing collision frequency.

For $\nu_{eff} > \omega_{be}$ but $\nu < \omega_{*max}$, i.e., trapped particles collide before a full bounce period is completed, drift dissipative modes develop and we have the following "pseudoclassical" transport coefficients

$$\chi_e \sim C_o \nu_{ei} \rho_{\theta e}^2 \qquad \text{and} \qquad D \sim C_1 \nu_{ei} \rho_{\theta e}^2 \tag{36}$$

with $C_o = 10$ and $C_1 = 10/3$ for NUWMAK.

For $\nu_{eff_e} < \omega_{be}$, $\nu_{eff_e} > \omega_{*min}$ trapped particles bounce before undergoing Coulomb collisions, hence are "collisionless". When a temperature gradient exists, these collisions do not retard the $\overline{E \times B}$ drift of the trapped electrons and the dissipative trapped electron mode develops with transport coefficients

$$\chi_e \sim \frac{3\,\varepsilon^{3/2}\, r^2\, \omega_{*min}\, \omega_{*min}^T}{\nu_{ei}} \qquad \text{with } \omega_{*min}^T = \frac{1}{e\,Br}\frac{\partial T}{\partial r} \tag{37}$$

$D \sim \varepsilon \chi_e \sim \chi_i$.

For $\nu_{effe} < \omega_{be}$, $\nu_{effe} < \omega_o \sim 0.1\,(r/\rho_{\theta e})\,\omega_{*min}$ again we have a dissipative trapped electron mode instability developing. However, in this lower collision frequency regime the effective wave number k of this mode is determined by the magnetic shear and we obtain

$$\chi_e \sim C_2 \nu_{ei} \rho_{\theta e}^2 \qquad \text{where } C_2 = 0.06\,\varepsilon^{1/2}\,\frac{d\ell nT}{d\ell nn}\,\frac{m_i}{m_e}\,\frac{B_p}{\theta B} \tag{38}$$

$D \tilde{\sim} \varepsilon \chi_e \sim \chi_i$ = constant of order 10^2 depending upon the magnetic shear

$\theta \equiv r_n/L \rightarrow \theta = r_n/L_S$

Finally for $\nu_{eff_i} \ll \omega_{bi}$ the frequency of this mode is below the ion bounce frequency. The drift wave in this case is supported by only trapped particles and we have

$$D \sim \chi_e \sim \chi_i \sim \frac{\varepsilon^{5/2} r^2 \omega_{*min}^2}{\nu_{ei} (1 + T_e/T_i)^2} \tag{39}$$

In the point code, all of the above transport coefficients are first calculated and the largest values for D and $\chi_{i,e}$ are used in the energy balance equations.

To eliminate the spatial dependency in density and temperature, we use the following expressions for the average density and temperature[9,10]

$$\bar{n} = 2 \int_o^a \frac{n(r) r dr}{a^2} \tag{40}$$

$$\bar{T} = \frac{\int_o^a n(r)\, T(r)\, r dr}{\int_o^a n(r)\, r dr} \tag{41}$$

where both T(r) and n(r) are assumed of parabolic form

$$n(r) = 2\, n_o \left(1 - \frac{r^2}{a^2}\right)^{\alpha} \tag{42}$$

$$T(r) = 2\, T_o \left(1 - \frac{r^2}{a^2}\right)^{\beta} \tag{43}$$

where α and β are set equal to 1 for the cases we analyze.

Since NUWMAK is noncircular, a shape factor S is defined[10] by

$$S = \frac{\text{circumference of plasma}}{\text{circumference of prescribed circular plasma}} \tag{44}$$

so that the stability factor q is given by

$$q = \frac{S}{A} \frac{B_T}{B_p} \tag{45}$$

where A is the aspect ratio of the smaller inscribed circular plasma and B_p is the poloidal field at the plasma edge.

In the point code, we assume that through some fueling mechanism, such as low energy neutral beams or pellets, the density of deuterium and tritium remains constant, although the ratio of the two species may vary if neutral deuterium beams are used. The resultant alphas from both main body and TCT fusions are calculated and we may find the resultant electron density by the charge neutrality condition

$$n_e = n_D + n_T + 2n_\alpha \tag{46}$$

We now spatially average the RF heating expressions (Eqns. (9) and (3) in Section II) assuming the parabolic expressions (42), (43) and define

$$PRFI = \int_0^a \frac{\varepsilon_o \omega_{pi}^2(r)}{4\ell\, \omega_{cio}} \frac{R}{r} \left[\frac{\langle k_\perp^2\rangle v_{thi}^2(r)}{2\,\omega_{ci}^2(r)}\right]^{\ell-1} |E_+|^2\, r dr \Big/ \int_0^a r dr \tag{47}$$

$$PRFE = \frac{\displaystyle\int_0^a \frac{\pi^{1/2}\varepsilon_o}{4\,k_\parallel} \frac{\omega_{pe}^2(r)}{\omega_{ce}^2(r)} \langle k_\perp^2\rangle v_{the}(r)\,(1 + x^2(r))\,|E_+|^2\, e^{-\left(\frac{\ell^2\omega_{cio}^2}{k_\parallel^2 v_{the}^2(r)}\right)} r dr}{\displaystyle\int_0^a r dr} \tag{48}$$

In the expressions for PRFI and PRFE we have previously averaged $k_\perp^2$ over the resonant heating zone whose width is given for both ion species by

$$\Delta R = \frac{2\, k_{\parallel}\, v_{thi}\, R}{\ell\, \omega_{cio}} \tag{49}$$

while for the electrons, ΔR is taken to be the entire plasma cross section since electron Landau heating as well as transit time magnetic pumping occur over the entire plasma radius. With this model we have neglected possible effects due to coupling problems as well as multiple modes. With this we find that

$$PRFI = \frac{|E_+|^2}{2\ell\omega_{cio}a^2}\, \varepsilon_o R \int_0^a \omega_{pi}^2(r) \left[\frac{\langle k_\perp^2\rangle\, v_{thi}^2(r)}{2\,\omega_{ci}^2(r)}\right]^{\ell-1} dr \tag{50}$$

$$= PRFI'\ |E_+|^2$$

$$PRFE = \langle k_\perp^2\rangle \frac{|E_+|^2}{2k_{\parallel}a^2}\, \pi^{1/2} \int_0^a \frac{\omega_{pe}^2(r)}{\omega_{ce}^2(r)}\, v_{the}(r)\, (1 + x^2(r))\, e^{-\ell^2\omega^2_{cio}/k_{\parallel}^2 v^2_{the}} dr \tag{51}$$

$$= PRFE'\ |E_+|^2 \tag{52}$$

Since $2\omega_{CD} = 3\omega_{CT}$ we have $\ell = 2$ for deuterium, $\ell = 3$ for tritium. Hence,

$$\text{TOTAL RF INJECTED POWER} = |E_+|^2 \times (PRFD' + PFRT' + PFRE') \times \text{VOLUME} \tag{53}$$

where PRFD' is the contribution to PRFI' from deuterium while PRFT' is that from tritium.

In the point code, we input the total power deposited in the plasma; therefore we normalize $|E_+|^2$ such that

$$|E_+|^2 = \frac{\text{TOTAL RF INJECTED POWER}}{(\text{PRFD}' + \text{PRFT}' + \text{PRFE}') \times \text{VOLUME}} \quad . \tag{54}$$

There are several possible scenarios for an RF heated reactor startup[12-14]. As shown in Table 1, we are looking at a non-circular tokamak of minor radius 1.25 m, major radius of 5.00 m, non-circularity factor of 1.33, toroidal B field on axis of 60 kG which determines the RF frequency used as 92 MHz and plasma current of 6.48 MA which results in a thermal energy output of 2300 MW. The average electron density is approximately 2.00×10^{14} cm^{-3}, while the plasma is a 50-50 mix of D and T. Also initially, $T_i=T_e=1.0$ keV for Figs. 1 thru 9, while for the latter figures $T_i=T_e=300$ eV.

First of all, in Fig. 1, a moderate amount of power may be supplied for a relatively long time, or left on during the entire burn time in the case of a driven reactor. In Fig. 1, we supply RF power levels of 50, 70, 80 and 100 MW for a full 3 seconds. We notice that for power levels of 80 MW and above, an equilibrium ion temperature of 15 keV can be achieved within 3 seconds.

By going to higher RF power levels supplied over a shorter time, we may increase the duty cycle of the power reactor. In Fig. 2, for power levels above 125 MW supplied for 1 second, an equilibrium ion temperature of 13.5 keV may be achieved as early as 1.5 seconds after the RF heating phase, thereby decreasing the startup phase by as much as 1.5 seconds. The equilibrium temperature in Fig. 1 is higher than the one in Fig. 2 because the continuous supply of RF power in the driven case causes the plasma to reach a higher equilibrium. If the RF was shut off in the driven case, the plasma would then relax to the equilibrium value of the undriven case. In addition Fig. 2

Table 1

REACTOR PARAMETERS

$a = 125$ cm	$\bar{n}_e = 1.95 \times 10^{14}$ cm^{-3}
$R = 500$ cm	$\bar{n}_e = \bar{n}_T = .975 \times 10^{14}$ cm^{-3}
$A = 4$	$\frac{n_{edge}}{n_{max}} = \frac{T_{edge}}{T_{max}} = .01$
$S = 1.33$	$T_i = T_e = 1.0$ keV
$I = 6.48$ MA	$f = 92$ MHz
$B_o = 60$ KG	$k_{\parallel} = 0.1$ cm^{-1}
$P \simeq 2300$ MW	$k_{\perp} \sim 1.6$ cm^{-1}
Toroidal mode number = 50	

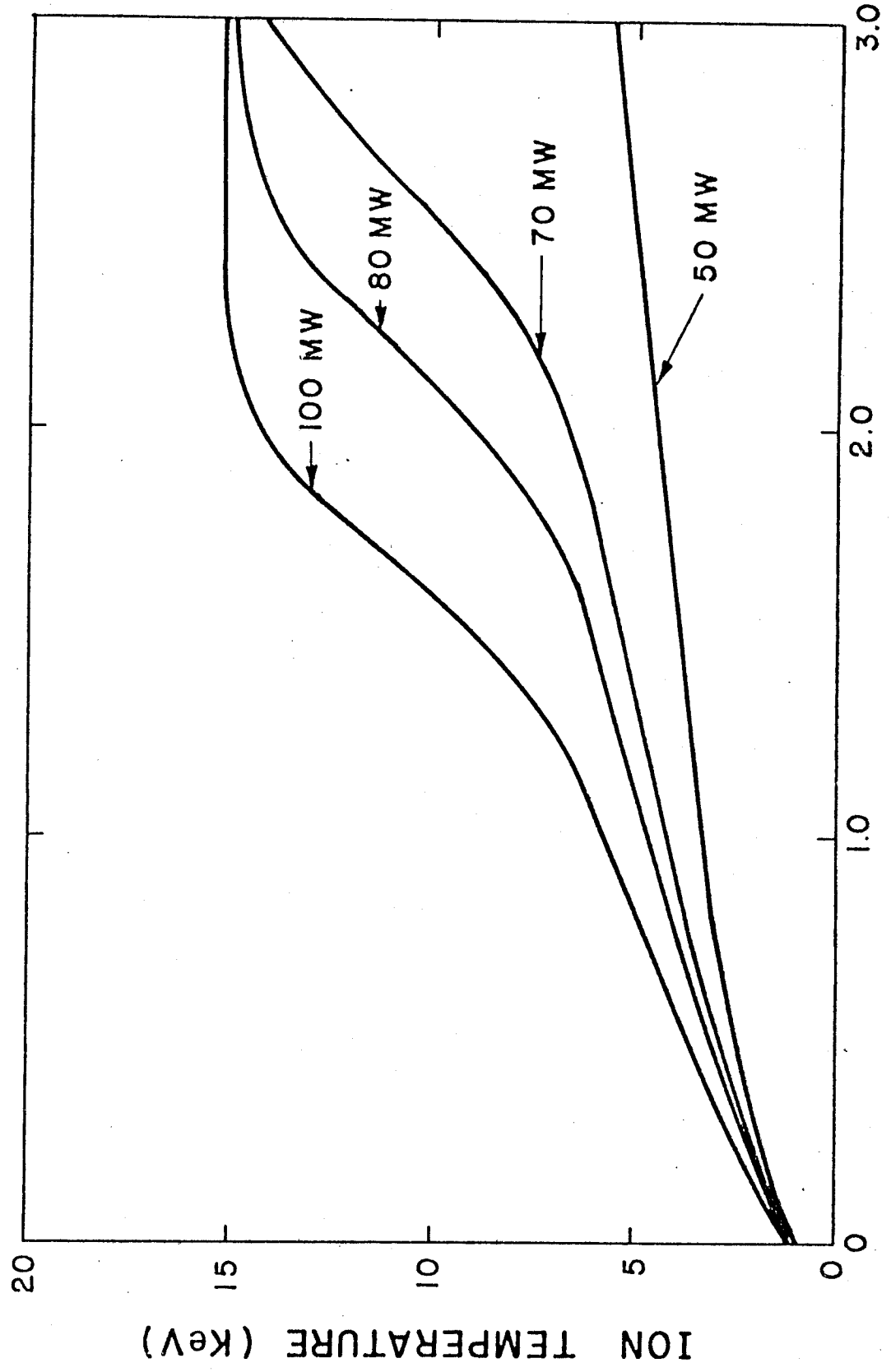

Fig. 1. Magnetosonic wave heating for RF power levels of 50, 70, 80 and 100 MW applied for 3 sec.

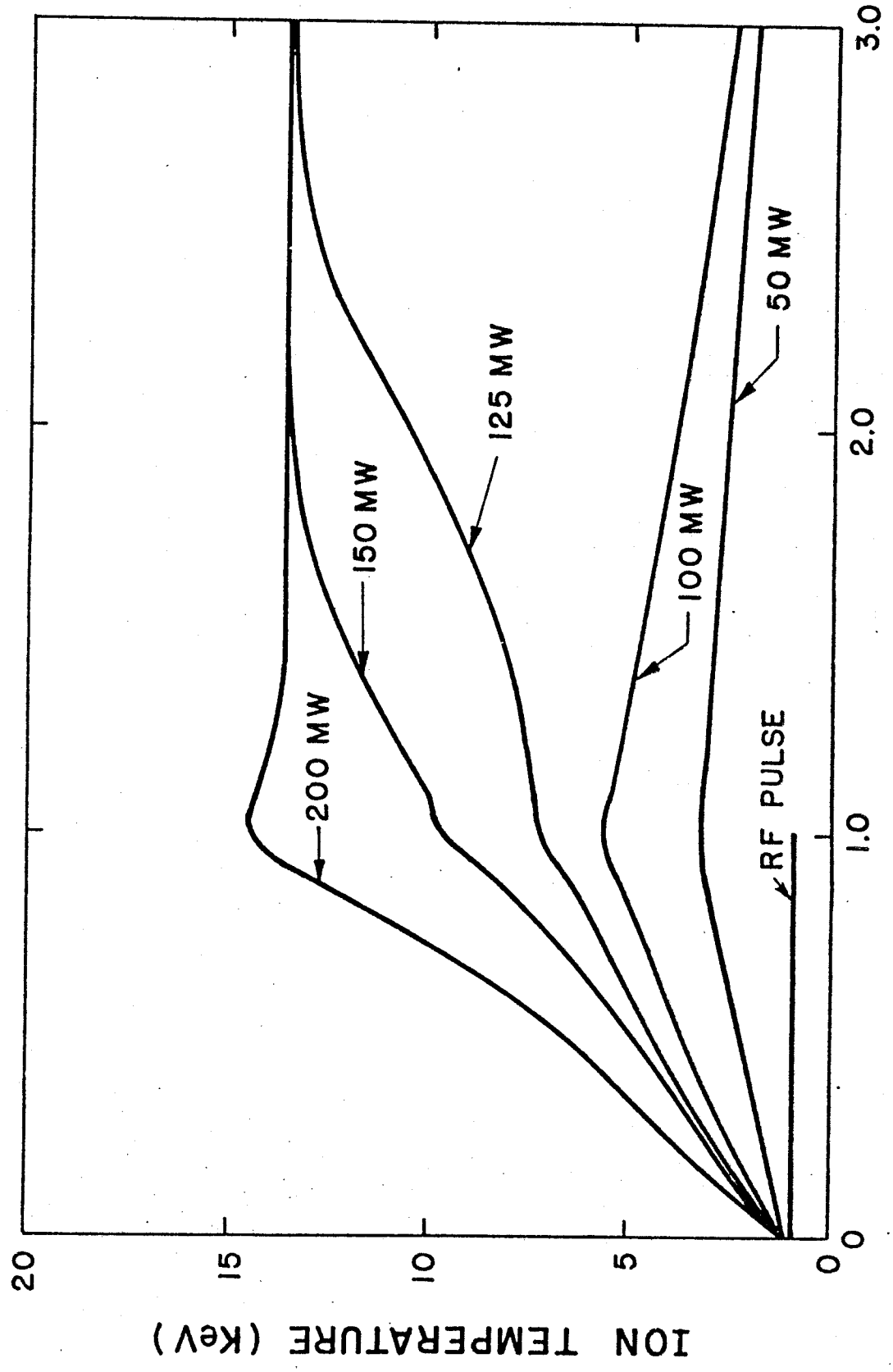

Fig. 2. Magnetosonic wave heating for RF power levels of 50, 100, 125, 150 and 200 MW applied for 1 sec.

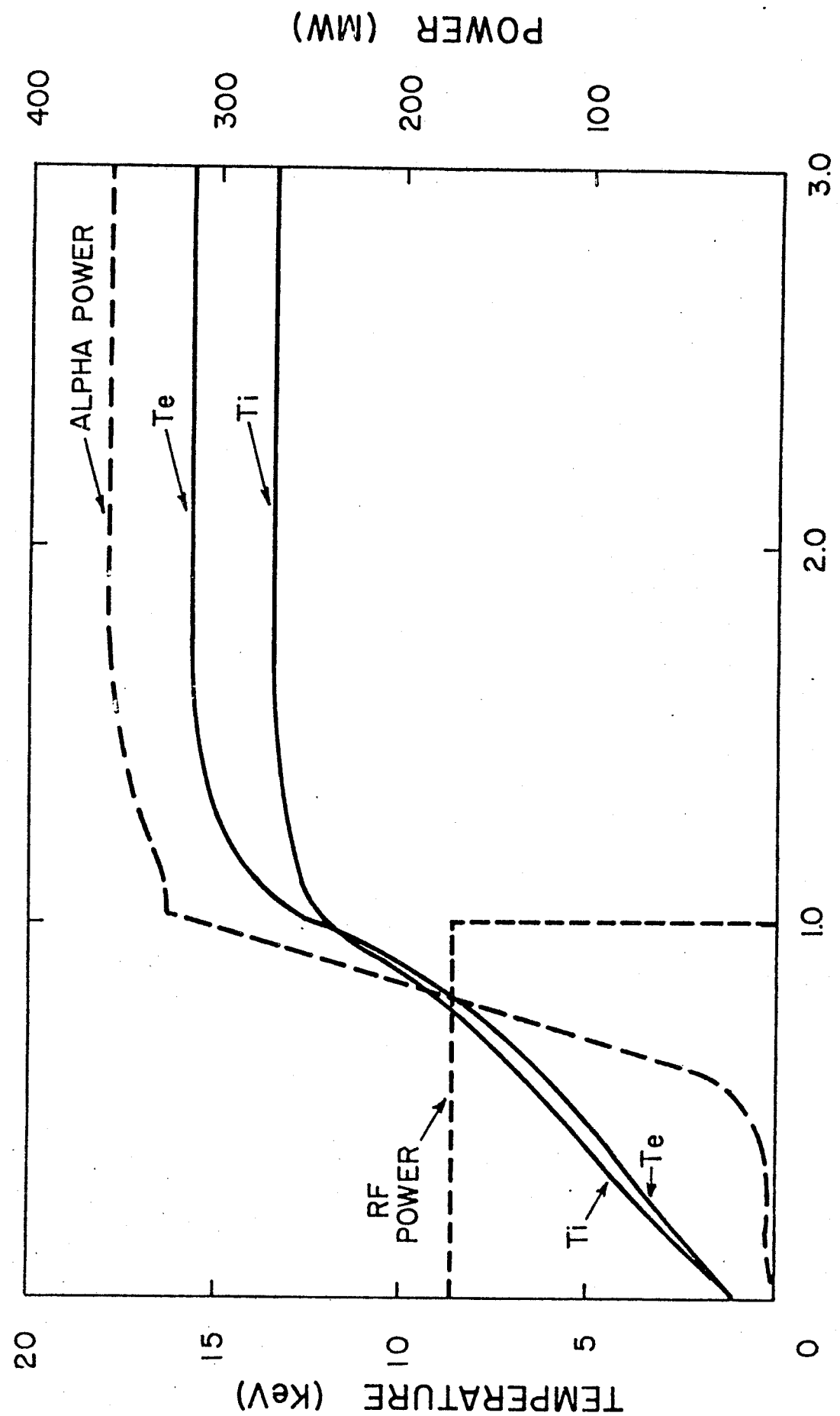

Fig. 3. Magnetosonic wave heating to reactor ignition and alpha power deposited in the electrons for an RF pulse of 1 sec. at 175 MW.

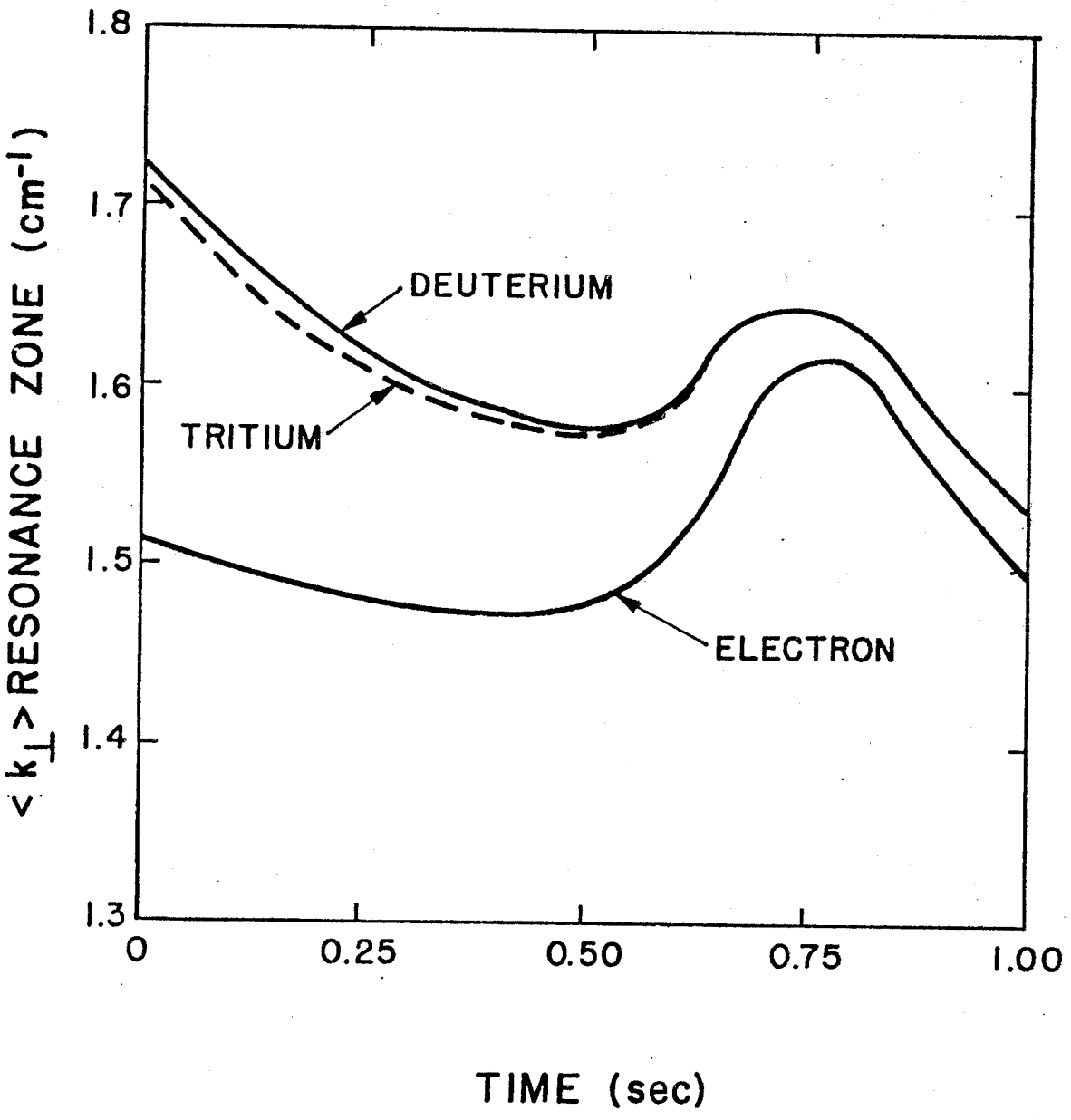

Fig. 4. $k_{\perp}$ averaged over the resonance zone of each species for an RF power level of 175 MW.

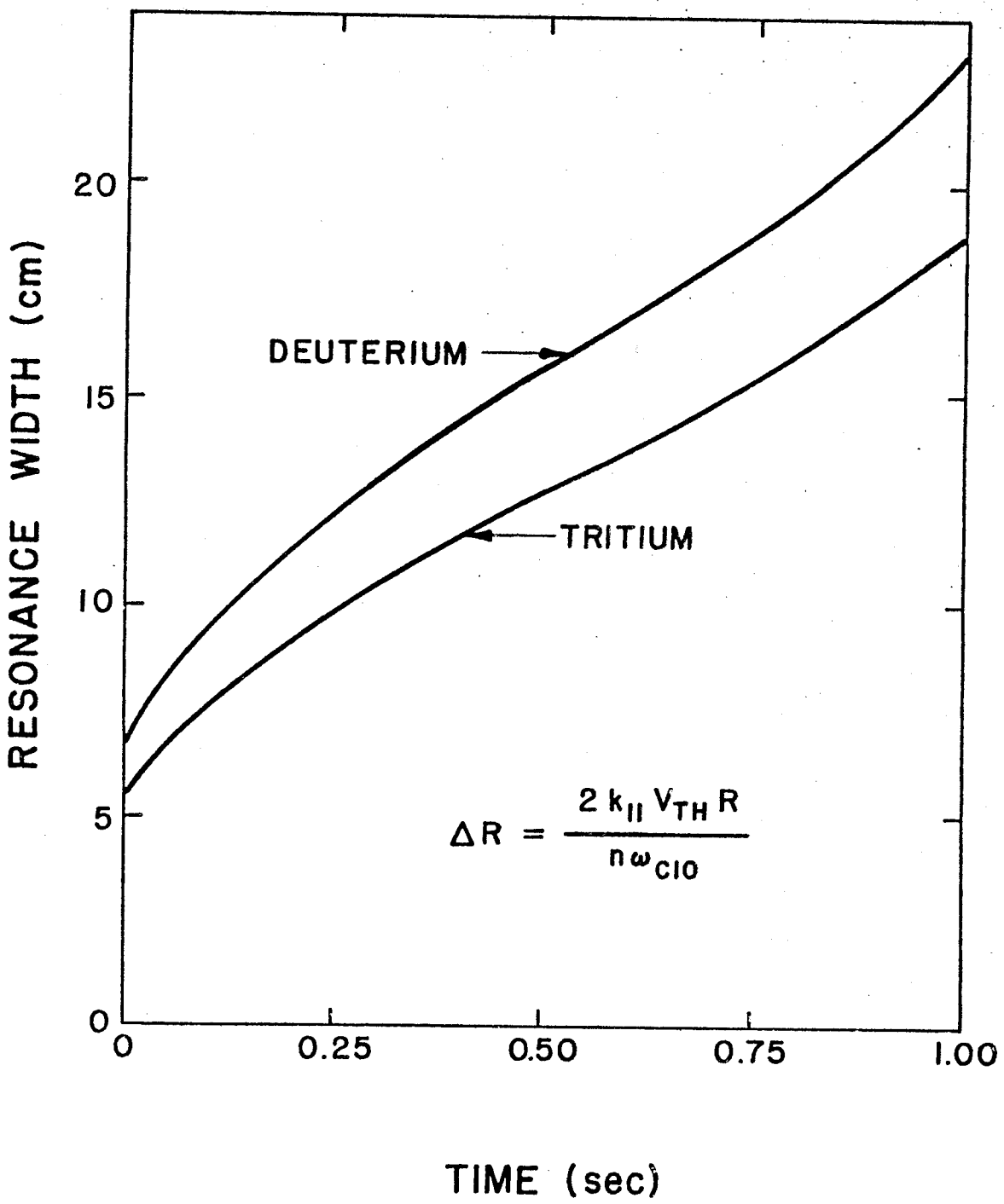

Fig. 5. Deuterium and tritium resonance widths for an RF power level of 175 MW.

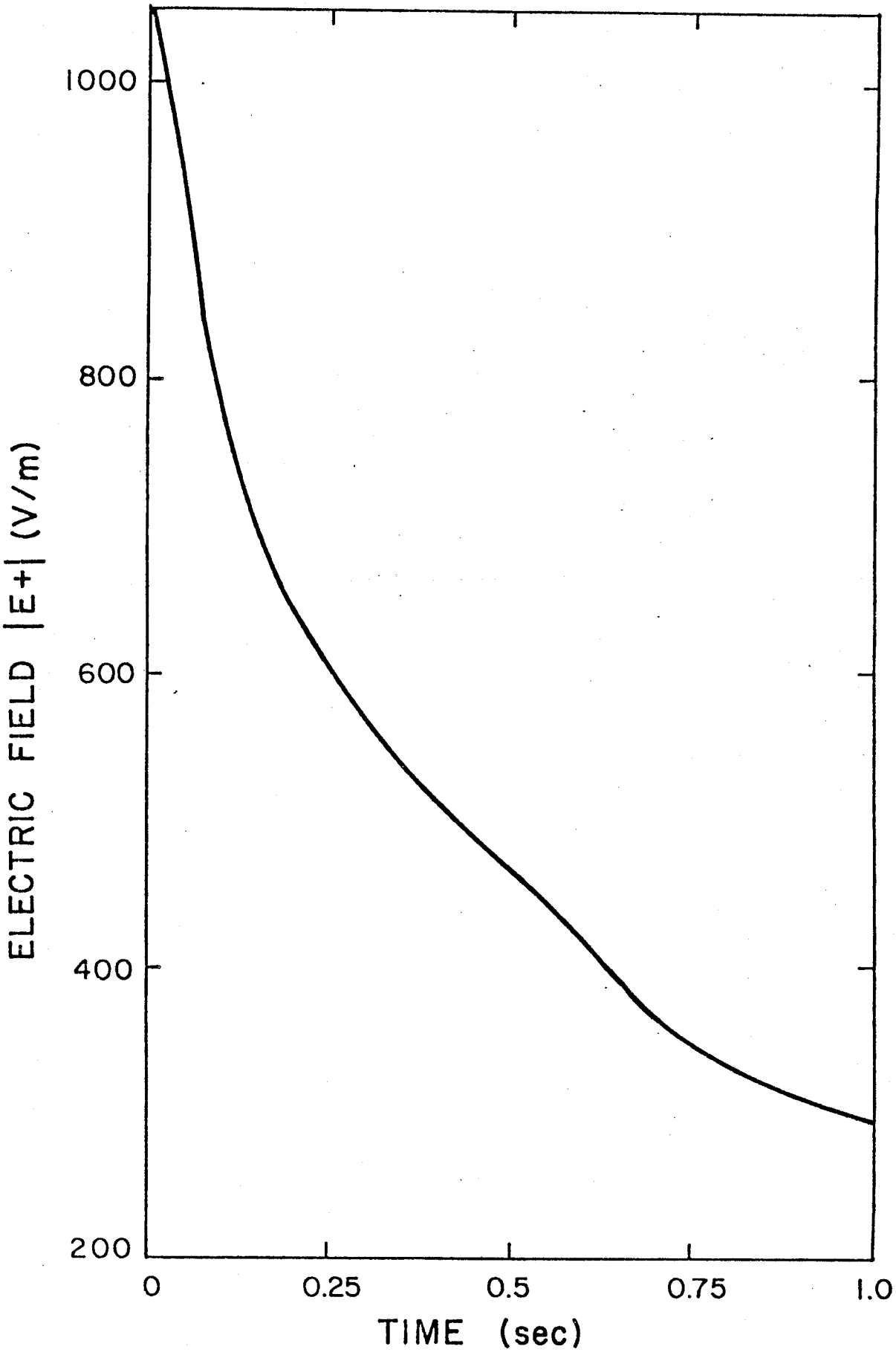

Fig. 6. Magnetosonic wave electric field $|E_+|$ for an RF power level of 175 MW.

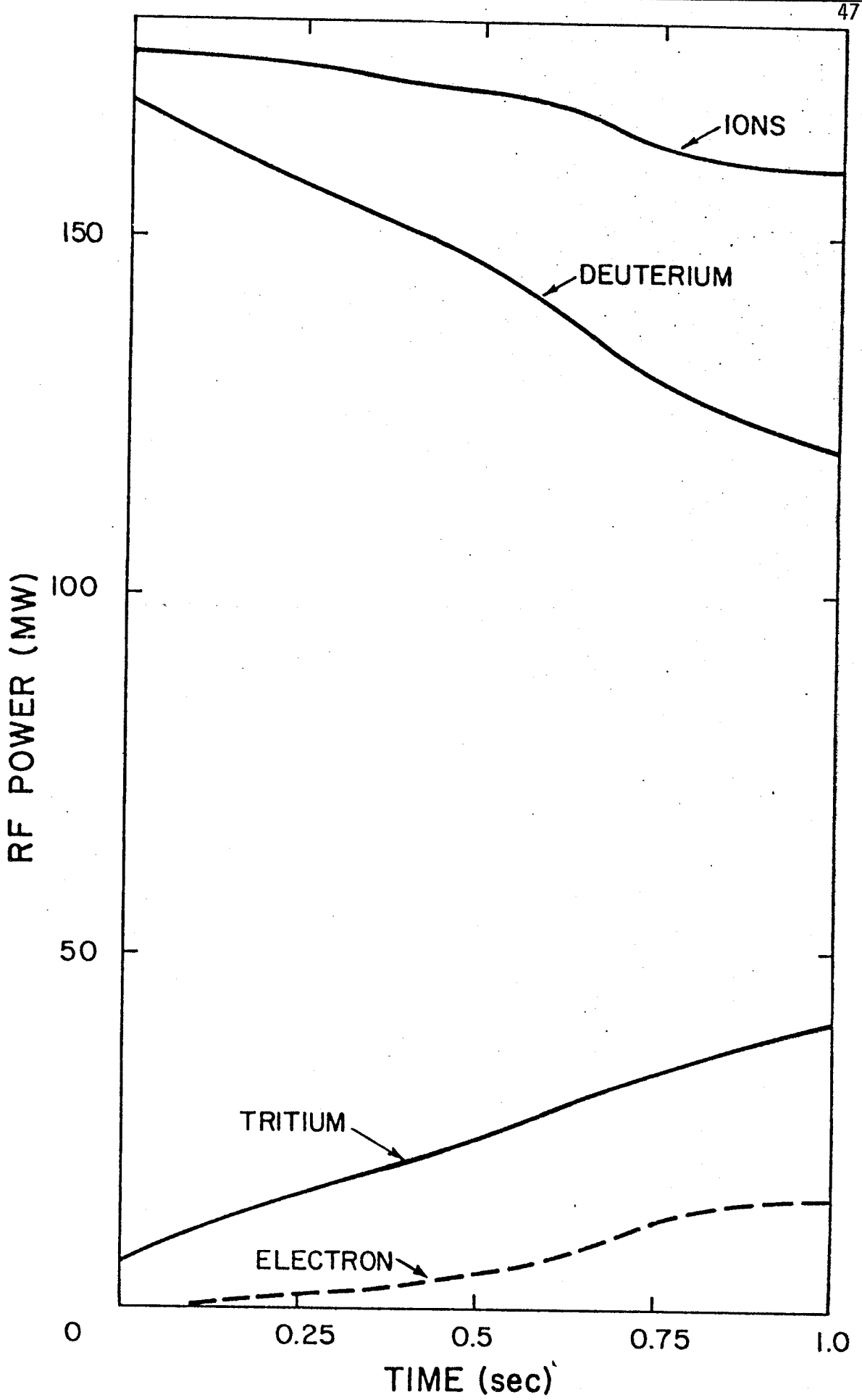

Fig. 7. RF power absorbed by each species for a total input power of 175 MW.

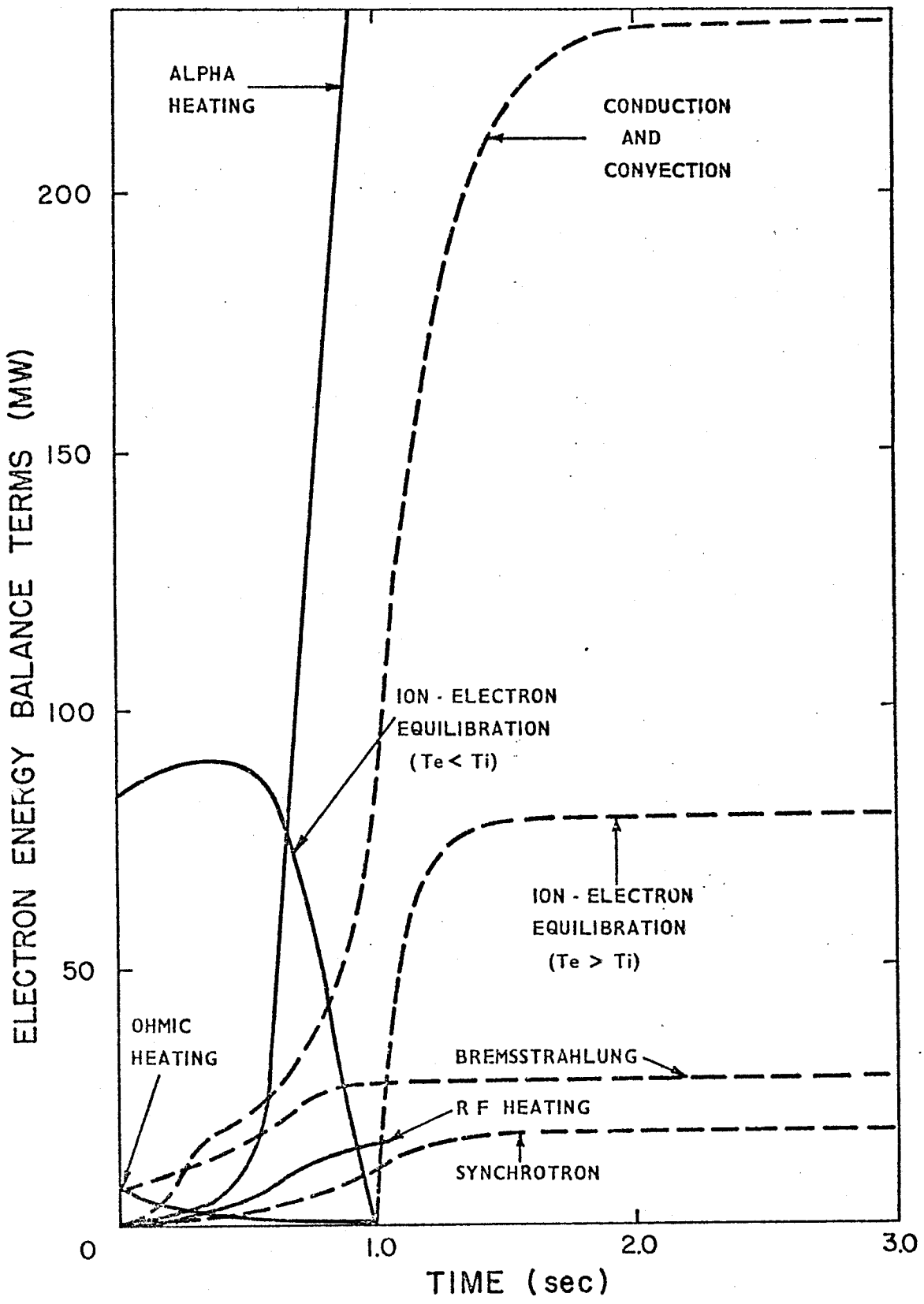

Fig. 8. Electron energy balance terms for an RF power level of 175 MW for a 1 sec. pulse.

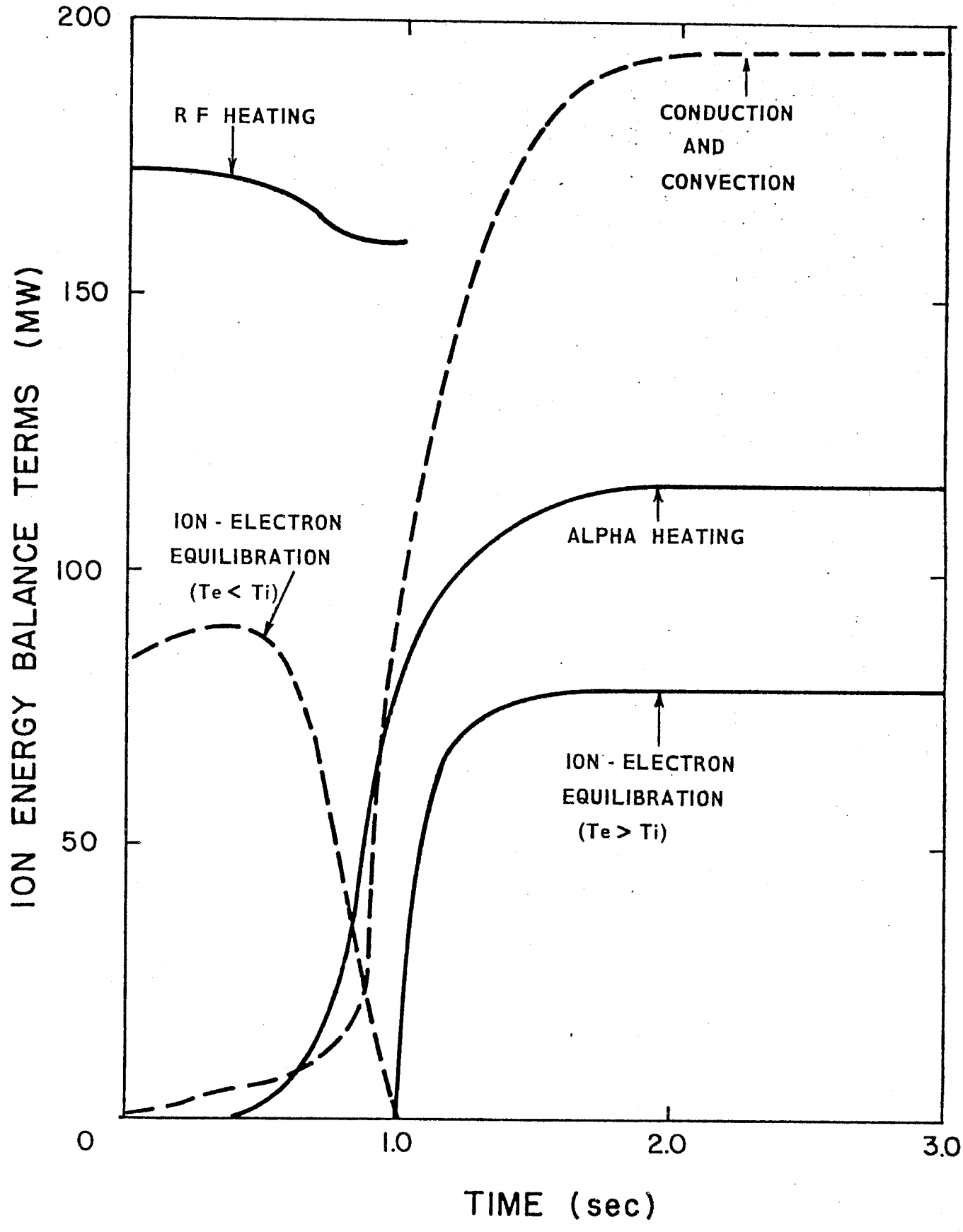

Fig. 9. Ion energy balance terms for an RF power level of 175 MW for a 1 sec. pulse.

shows that for power levels of 100 MW and below the plasma never reaches ignition and the plasma temperature subsequently drops once the RF is turned off.

In Figs. 3 thru 9 we deal with the case of 175 MW supplied for 1 second. In Fig. 3, we notice that in the first second of operation T_i is greater than T_e because most of the RF power is supplied to the ions (see Fig. 7). However, 800 ms after the RF is turned on, T_i becomes so high that a significant number of fusions occur. The resultant alphas deposit most of their energy in the electrons as they thermalize causing T_e to become greater than T_i, reaching a steady state value of 15 keV as compared to that of 13.5 keV for the ions. The alpha power to the electrons as shown in Fig. 3 rises sharply after 800 ms and eventually reaches an equilibrium value of 360 MW. The kink in the alpha curve corresponds to the sudden loss of RF heating power at the time of shut off.

In Eqs. (50) and (51) an averaged value for $k_\perp^2$ was used. In Fig. 4 we have the averaged value $\langle k_\perp^2 \rangle^{1/2}$ for each species when $k_\perp^2$ is averaged over either the resonant heating zone of each ion species as shown in Fig. 5 or, for the case of the electrons, over the entire plasma cross section. In Fig. 5, the resonant width for deuterium increases from 6.6 cm to 23 cm while that of tritium spreads from 5.5 cm to 18.8 cm as T_i increases.

Figure 6 displays the magnitude of the spatially averaged electric field $|E_+|$. We notice that $|E_+|$ drops from a peak value of 1040 V/m to that of 280 V/m with increasing time. As time increases, the plasma conductivity increases, hence the magnitude of E_+ must decrease if we wish to supply a constant amount of power to the plasma.

In Fig. 7, we see the amount of RF power supplied to each species. Most of the power supplied goes to the ions though it does decrease from an initial high of 175 MW to 160 MW. As the plasma temperature increases, the power flow to deuterium decreases from 170 MW to 120 MW. This decrease is partially compensated by an increase of power flow to tritium, which rises from 7 MW to 40 MW. The remaining power is deposited in the electrons, reaching a peak before shut off of 15 MW. As the temperature increases, power flow to the electrons increases because the expression in the exponential factor of the electron heating term decreases. In addition we see more power going to the tritium at the expense of the deuterium because of the ratio $\frac{P_T}{P_D} \sim T_i$.

Figures 8 and 9 show the terms in the electron and ion energy balance equations. Dashed lines indicate energy loss mechanisms while solid lines indicate heating terms. In Fig. 8, we see that at these high plasma temperatures the Ohmic heating term is quite small, decreasing from 7 MW to 1 MW. After 500 ms, the alpha heating term becomes so large that even if mode conversion processes were present causing most of the power to be deposited in the electrons, our results would still be the same. As Fig. 3 shows, since $T_i \simeq T_e$, the electron-ion equilibration time is quite short, indicating that heating of the electrons would drag the ion temperature along with it, thus not changing our results. Equilibrium is reached when the loss terms equal the heating terms. In the case of the electrons, at equilibrium as shown in Fig. 8, the electrons lose 18 MW from synchrotron radiation, 28 MW from Bremsstrahlung, 235 MW through con-

duction and convection, and since $T_e > T_i$ at equilibrium, the electrons lose 80 MW to the ions from the equilibration term. However, as shown in Fig. 3, the electrons receive 360 MW from the thermalization of the alphas. As for the ions at equilibrium, Fig. 9 shows that the ions lose 195 MW through conduction and convection, but receives 80 MW from the electrons due to the equilibration term and also receives 115 MW from the thermalization of the alphas.

Finally,in order to increase the duty cycle of a reactor while at the same time use a lower level of RF power, it may be possible to heat during the Ohmic-heating current-rise phase of operation. Figure 10 shows the amount of RF power to each species as well as the total amount. In this case, the RF power is ramped linearly up to 75 MW in 3 seconds and then kept at this power level for an additional .1 second after the current rise period. We see that the power to the ions reaches a peak value of 72 MW after 3 seconds and then decreases to a value of 68 MW. During this time the power to deuterium also peaks at 3 seconds with a value of 60 MW before it declines to the final value of 48 MW. Again we see a steady rise in power to tritium up to 20 MW as well as to the electrons, up to 7 MW. The drop in power to the deuterium while the rise in power to both tritium and electrons may be explained as before.

In Fig. 11, we notice that during the Ohmic-heating current rise period, the plasma current is assumed to rise linearly in 3 seconds from 1 MA to its final value of 6.5 MA. During this period, by assuming that q, the safety factor, or consequently, the plasma current density remains constant, we obtain a plot of the increasing plasma minor

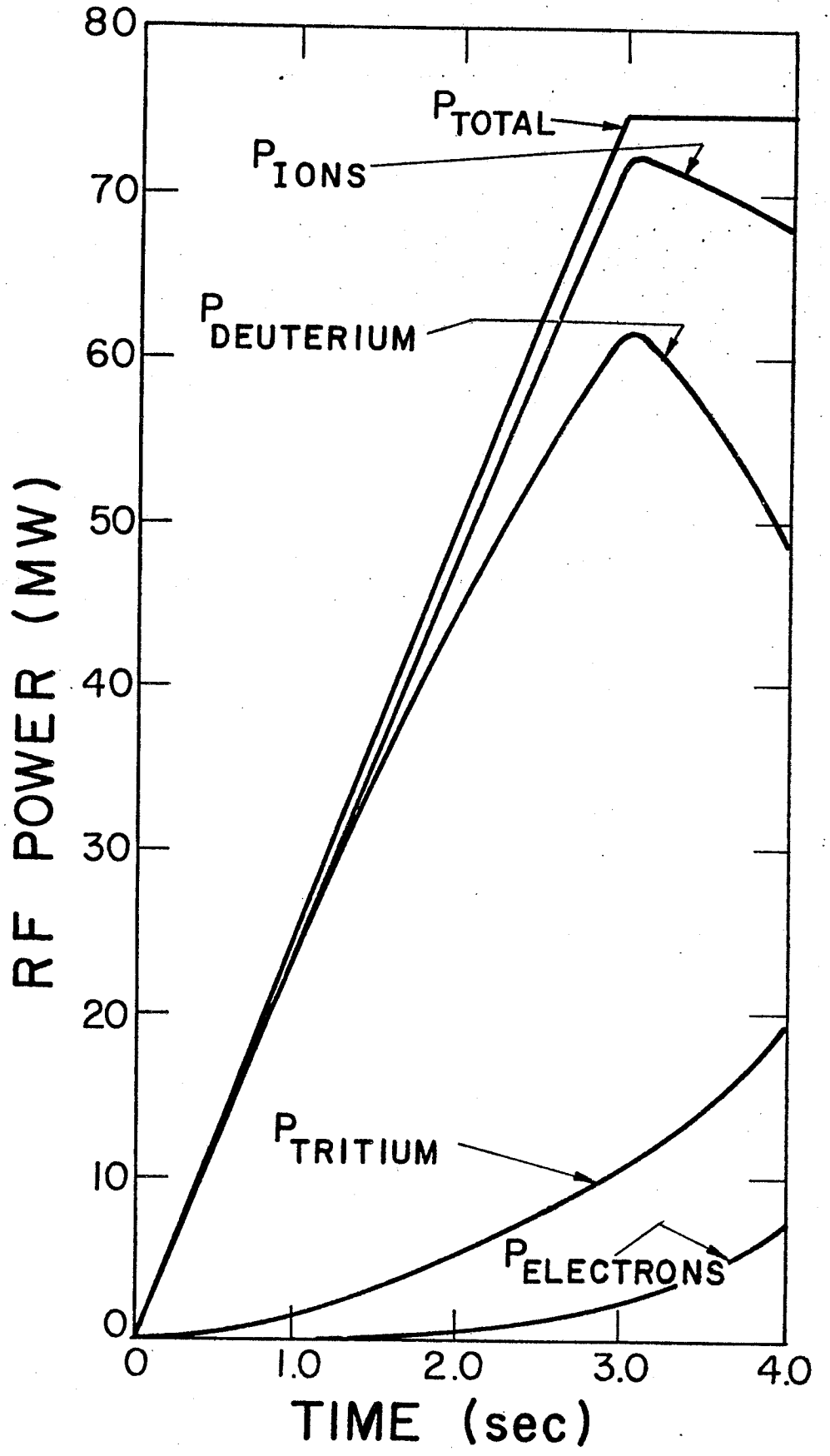

Fig. 10. RF power absorption of each species for a pulse ramped linearly from 0 to 75 MW in 3 sec. and then constant 75 MW for 1 sec. During the first 3 secs, the plasma current rises linearly from 1 to 6.5 MA.

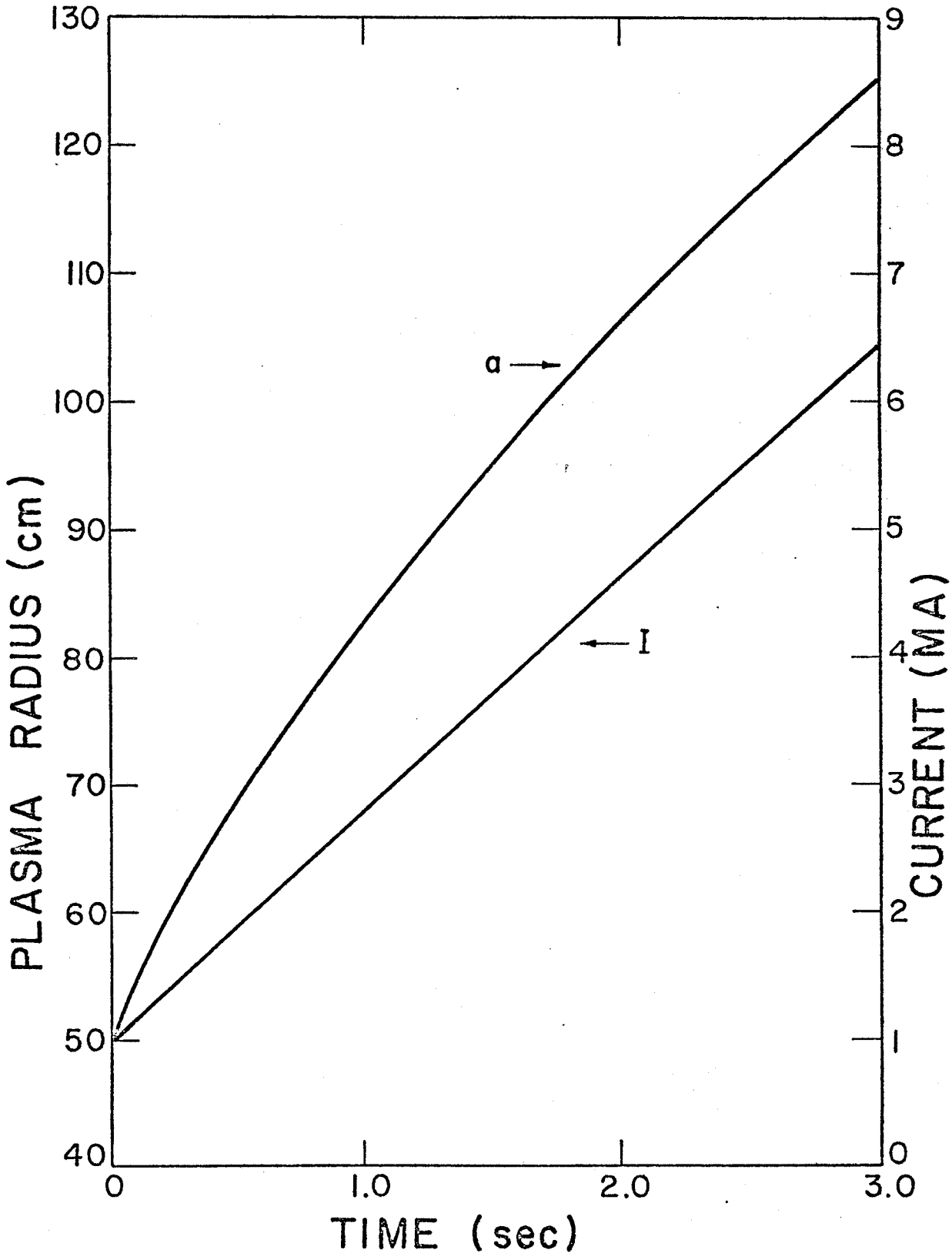

Fig. 11. Evolution of plasma current and minor radius during the plasma current rise for a 3 sec. operation.

radius also displayed in Fig. 11. At 1 MA we have a corresponding plasma minor radius of 50 cm while at the full current of 6.5 MA the corresponding final minor radius is 1.25 m.

In Fig. 12, by looking at the plot of the ion and electron temperatures, we see that equilibrium is achieved after a total time of 4.4 seconds or 1.4 seconds after the Ohmic-heating current-rise period. This time is approximately 1.5 seconds sooner than that obtained in Fig. 1. While this time is essentially identical to that obtained in Fig. 3, lower power levels were used.

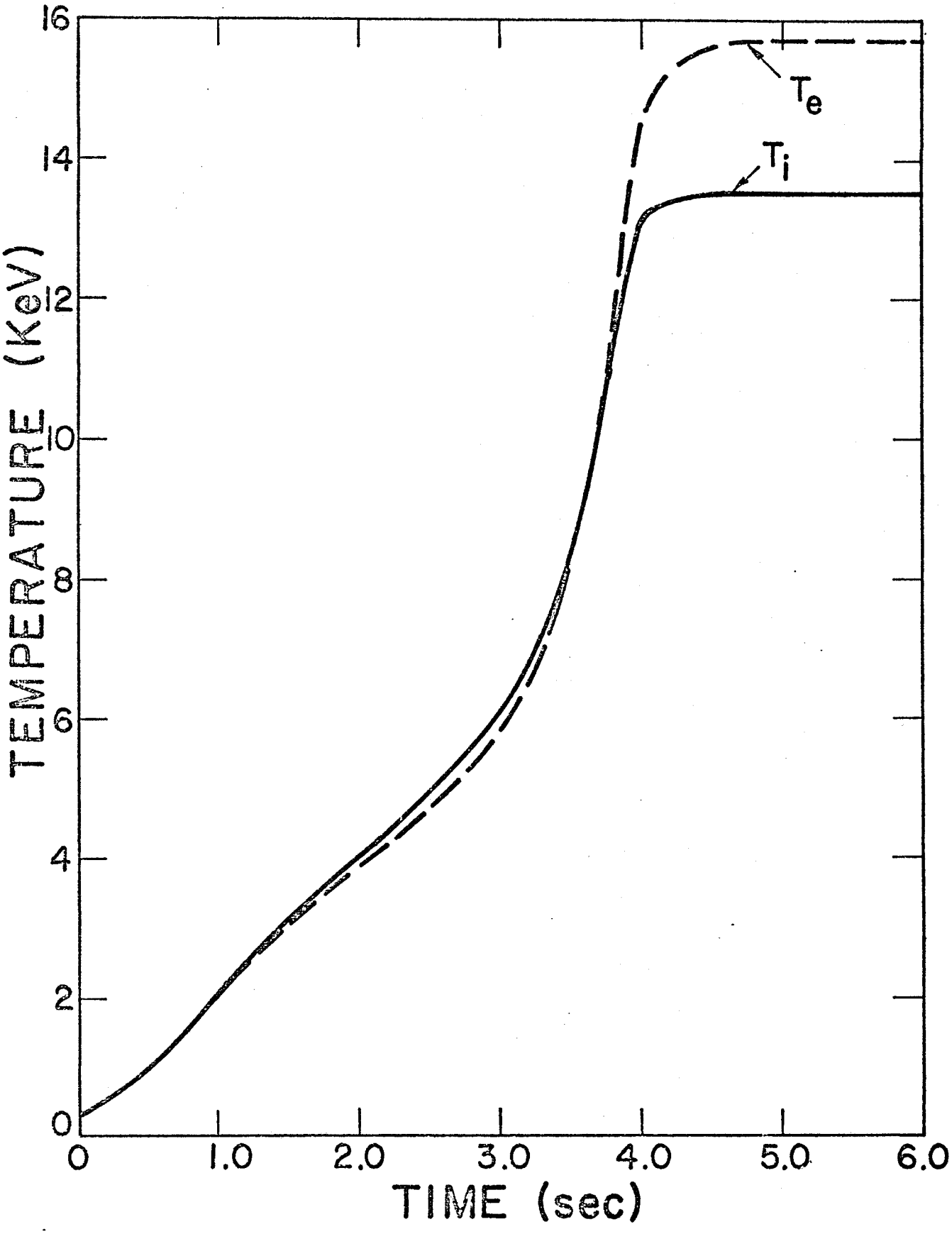

Fig. 12. Magnetosonic wave heating to ignition for an RF pulse ramped from 0 to 75 MW during the 3 sec. plasma current rise and then constant 75 MW for an additional 1 sec.

References

1. W. Houlberg, Ph.D. Thesis, (1977) University of Wisconsin-Madison, Madison, Wisconsin.

2. S. I. Braginskii, Review of Plasma Physics, M. A. Leontovich, Ed., Plenum Publishing Co., New York, Vol. I, p. 205, (1965).

3. N. A. Krall and A. W. Trivelpiece, Principles of Plasma Physics McGraw-Hill Book Co., New York (1973).

4. F. L. Hinton and R. D. Hazeltine, "Theory of Plasma Transport in Toroidal Confinement Systems", Reviews of Modern Physics 48, 239 (1976).

5. R. W. Conn, "Plasma Equations and Energy Equilibria and Stability", Nuclear Engineering Department Report UWFDM-16, p. 4, (University of Wisconsin-Madison, July 1972).

6. Lyman Spitzer, Jr., Physics of Fully Ionized Gases, Interscience Publishers, New York (1962).

7. D. J. Rose and M. Clark, Jr., Plasmas and Controlled Fusion, MIT Press, p. 233, Cambridge (1961).

8. T. F. Yang, H. K. Forsen and G. A. Emmert, "The Calculation and Parametric Study of the Synchrotron Radiation Loss for Tokamak Reactors", Nuclear Engineering Department Report UWFDM-49 (University of Wisconsin-Madison, 1973).

9. J. E. Scharer, R. W. Conn and D. T. Blackfield, "Study of Fast Magnetosonic and Neutral Beam Heating of Large Tokamaks", EPRI Report ER-268 Project 237-3 Topical Report, Sept. 1976.

10. B. Badger, et al. "UWMAK-III, A Noncircular Tokamak Power Reactor Design", Nuclear Engineering Department Report UWFDM-150 (Univ. of Wisconsin-Madison, July 1976).

11. "Status and Objectives of Tokamak Systems for Fusion Research" U.S. Atomic Energy Commission Report WASH-1239 UC-20.

12. J. E. Scharer, J. Beyer and D. T. Blackfield, Proceedings of the Third Topical Conference on Radio Frequency Plasma Heating, paper D7-1 (1978).

13. J. E. Scharer and D. T. Blackfield, Bulletin of the American Physical Society, 21, 1158 (1976).

14. D. T. Blackfield and J. E. Scharer, Bulletin of the American Physical Society, 22, 1185 (1977).

IV. RF Circuit Coupling to Magnetosonic Waves in the Tokamak Reactor

A. Introduction

In present tokamaks coupling structures are necessarily small with respect to a wavelength. Loop coupling at a point of high RF magnetic field intensity using external lumped capacitance to resonate with the loop inductance has been commonly employed. In reactors where the larger size allows self-resonant coupling structures a different approach may be used to advantage. If, on such large structures, a high voltage point can be used as the driving point then such a point will exhibit a high radiation resistance and will have considerable advantage from the standpoint of the driving system. Considering that air insulated coax line will be used, minimum loss occurs at a characteristic resistance, Z_0, of 73Ω and maximum power handling capacity occurs at a Z_0 of 30Ω, hence, driving point resistances of the order of 50Ω have considerable practical advantage.

One might expect that a $\lambda/2$ dipole would be a structure exhibiting these qualities. However, due to the physical constraints imposed by the reactor the dipole must be located near a conducting wall. Hence, the dipole's image is located near the dipole and as a result the driving point impedance is lowered. For example, to estimate the effect consider self and mutual impedance data for free space dipoles spaced $\lambda/10$ apart.

$$z_{11} = 73\Omega$$

$$z_{12} = 70 + j\ 10\Omega$$

Then considering antenna 2 in Fig. 1 to be the short circuited image antenna, one finds for the driving point impedance

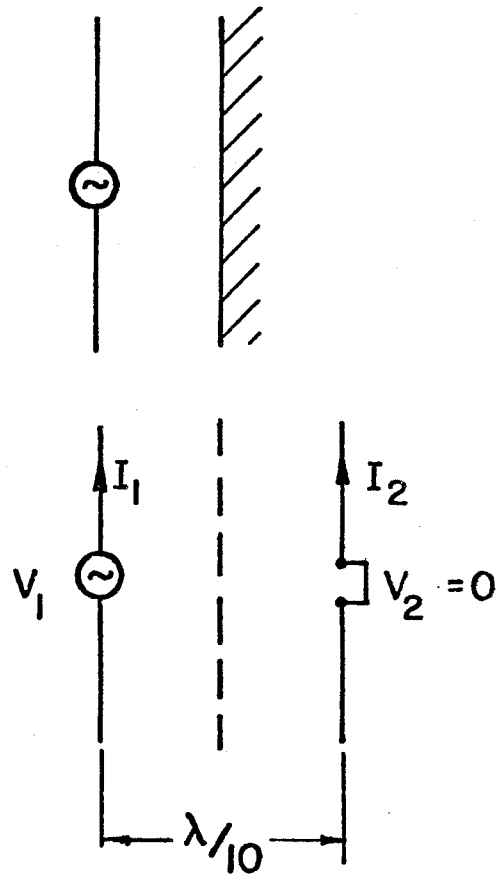

Fig. 1. Illustration of the effect of a conducting wall on a half-wavelength dipole antenna.

$$V_1 = I_1 Z_{11} + I_2 Z_{12}$$

$$V_2 = I_1 Z_{21} + I_2 Z_{22} \qquad (1)$$

$$\frac{V_1}{I_1} = Z_{11} - \frac{Z_{21}}{Z_{22}} Z_{12}$$

$$\simeq 5\Omega$$

This is rather low for efficient coupling. However, a higher impedance drive point may be selected away from the center of the antenna which will improve this value.

IV.B. Cavity-Backed Aperture Antenna

Let us consider now another method of obtaining a high driving point impedance, that of aperture coupling by using a cavity backed antenna. Such a concept has advantages from the reactor point of view since the coupling apertures are located flush with the first wall. In addition, from the RF driving system viewpoint the cavity acts as an impedance transformer and since it is in resonance, nearly any desired driving point resistance can be found by properly choosing the input coupling point to the cavity. Also the cavity can be conveniently tuned to accommodate changing reactor conditions. Figure 2 shows a proposed TE_{101} mode cavity antenna system. The cavity is a TE_{10} waveguide C meters wide and B meters high that is one half guide wavelength long in the A dimension. Figure 3 shows the resonance curve for the C and A dimensions at 92 MHz. (Note: In this mode B does not affect the resonant frequency.) Because of the given reactor dimensions we have chosen A = 3.5 m, B = 10 cm and C = 1.85 m. The height B = 10 cm was chosen to accommodate the input coupling structure in the outer blanket.

In order to further understand the choice of mode and cavity orientation one must consider the wave mode in the reactor. This mode is approximated by a TE_z cylindrical waveguide field description and since the H_z field at the outer wall is large, coupling via this field is used. Furthermore, since efficient core plasma heating is accomplished with low poloidal mode numbers ($m=0, \pm 1$), apertures over only half of the A dimension are used so that the reactor fields are not affected by the reversed H field over the other half of the antenna cavity. Figure 4 then shows the antenna cavity fields and their relationship to the reactor fields.

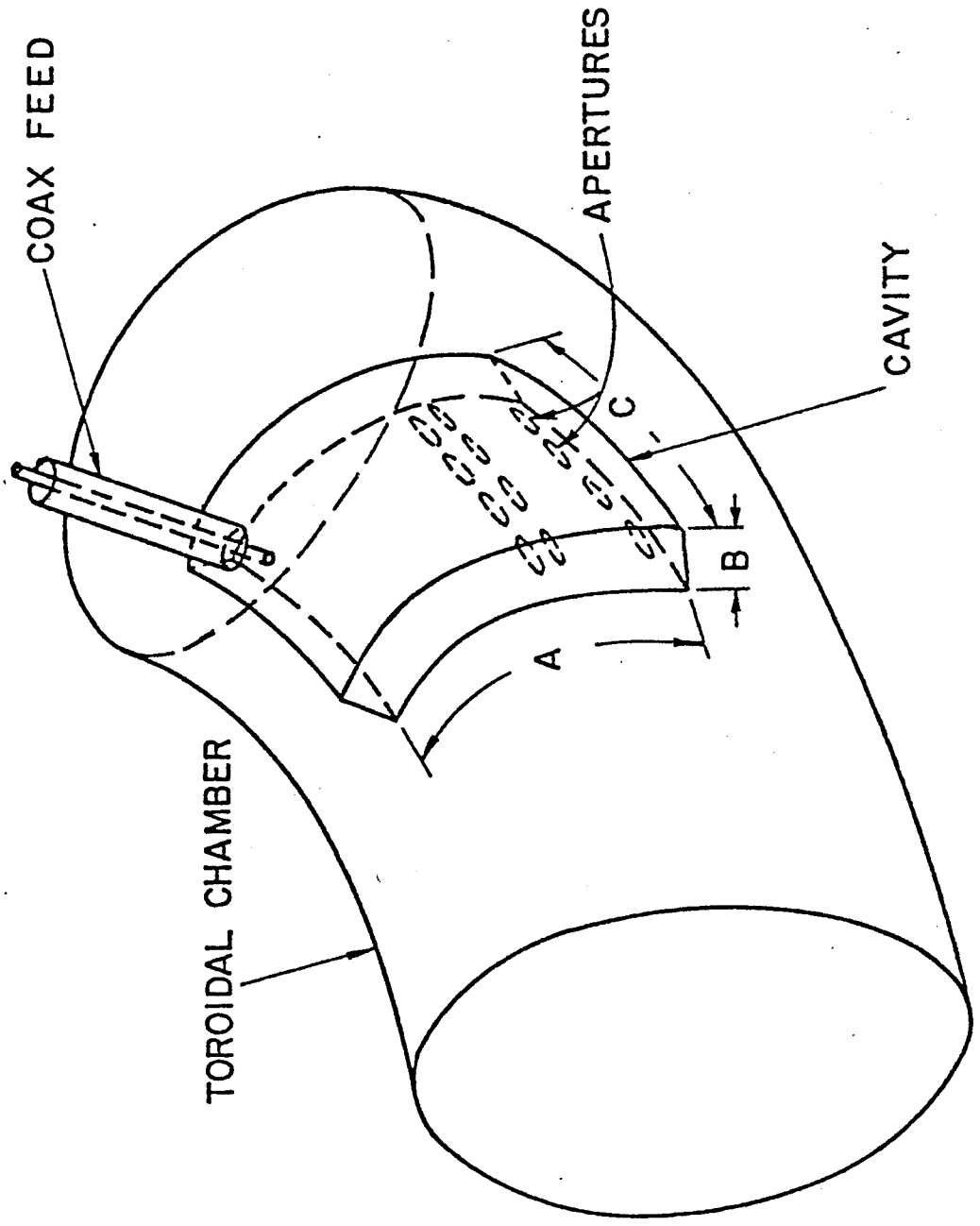

Fig. 2 Schematic of proposed TE_{101} mode cavity antenna system mounted on a torus.

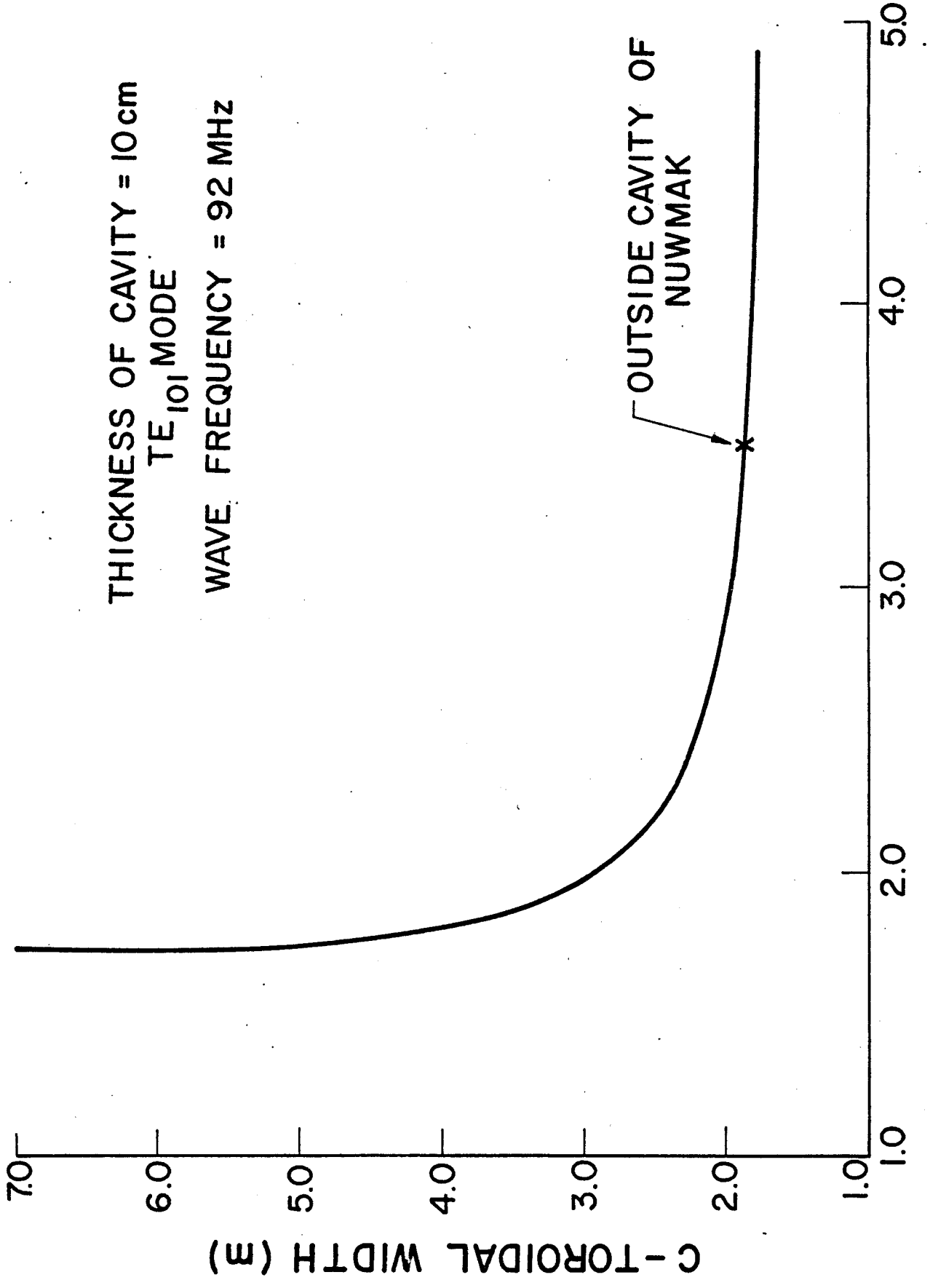

Fig. 3 Resonance curve of the C and A dimensions of the cavity antenna at 92 MHz.

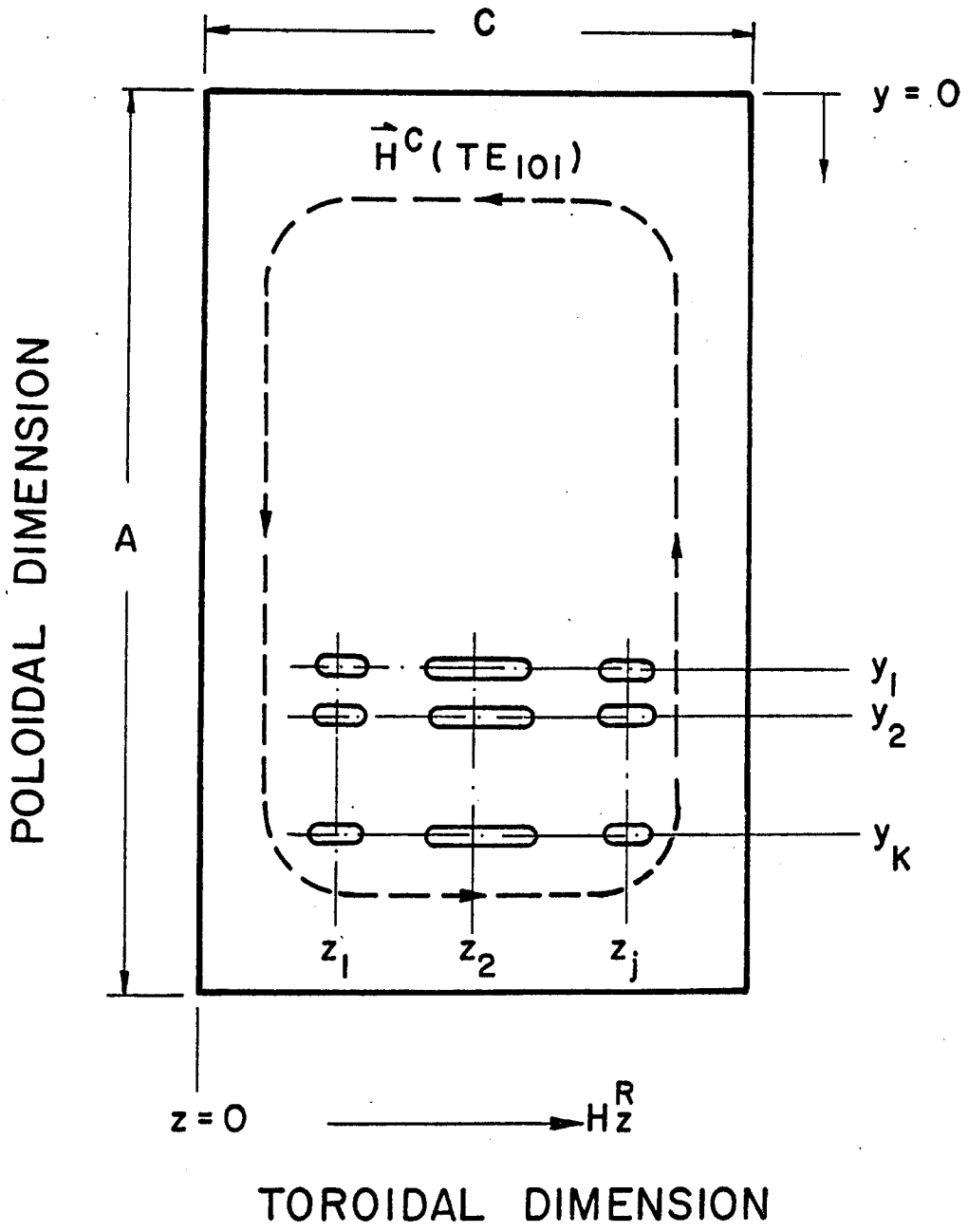

Fig. 4 Schematic of antenna cavity and reactor fields.

In the following equations the superscript R will designate reactor fields while the superscript C will be used for antenna cavity fields. Furthermore, the subscript m will indicate normal mode fields normalized according to

$$\iiint \mu_0 \bar{H}_m \cdot \bar{H}_m^* \, dV = 1 \tag{2}$$

For a description of the fields and normalization coefficient consider the following fields in a plasma-filled cylindrical waveguide which is an approximation to a toroidal cavity of minor radius a and major radius R. For the fast magnetosonic mode in a cold plasma, we can assume $E_z = 0$ (TE-mode).

Assume a single eigenmode of the form

$$H_z^R = h_{m0} J_m(k_r r) \, e^{i(k_\parallel z + m\theta - \omega t)} \tag{3}$$

where $k_\parallel = n/R = 20\ m^{-1}$ where n is the toroidal mode number.

m = poloidal mode number

$$k_r^2 = \Lambda/(k_0^2 - k_\parallel^2/S)$$

with $\Lambda = k_\parallel^4/S - 2k_0^2 k_\parallel^2 + k_0^4 \frac{RL}{S}$

$$S = 1 + \sum_\alpha \omega_{p\alpha}^2/(\omega_{c\alpha}^2 - \omega^2) \ , \quad R = 1 - \sum_\alpha \frac{\omega_{p\alpha}^2}{\omega^2} \left(\frac{\omega}{\omega+\omega_{c\alpha}}\right) \ , \quad L = 1 - \sum_\alpha \frac{\omega_{p\alpha}^2}{\omega^2} \left(\frac{\omega}{\omega-\omega_{c\alpha}}\right)$$

$k_0 = \omega/c$, $\omega_{c\alpha} = \frac{\varepsilon_\alpha e B_0}{m_\alpha}$ and $\varepsilon_\alpha = +1$ for ions and -1 for electrons.

The other field components are then given by

$$H_r^R = -ik_\parallel h_{m0}[a_2 \frac{m}{r} J_m(k_r r) + a_1 \, k_r \, J_m'(k_r r)] \tag{4a}$$

$$H_\theta^R = k_\parallel h_{m0}[a_1 \frac{m}{r} J_m(k_r r) + a_2 k_r J_m'(k_r r)] \qquad (4b)$$

where $a_1 = -k_r^{-2}$, $a_2 = (D/S)\, k_0^2/\Lambda$, and $D = \frac{1}{2}(R-L)$.

For an eigenmode, the boundary condition $E_\theta^R = -\frac{\omega}{k_\parallel} \mu_0 H_r^R = 0$ at $r = a$ is given by

$$a_2 \frac{m}{a} J_m(k_r a) + a_1 k_r J_m'(k_r a) = 0 \qquad (5)$$

Together with Eqs. (4), (5), and the normalization integral in Eq. (2), we obtain

$$h_{m0} = [2\pi^2 a^2 R_0 \mu_0 F_m(k_r a)]^{-1/2} \qquad (2a)$$

where h_{m0} is the normalized H-field amplitude as in Eq. (3), and

$$F_m(x) = 2 G_m(x) + k_\parallel^2 k_r^2 [(a_1 + a_2)^2 G_{m-1}(x) + (a_1 - a_2)^2 G_{m+1}(x)]$$

$$\text{with } G_m(x) = \frac{1}{2} J_m^2(x) \left(1 - \frac{m^2}{x^2}\right) + \frac{1}{2} J_m'^2(x) .$$

Let us first consider an overview of the coupling calculation. To find the cavity driving point impedance we work back from the reactor fields. From the computer simulation of the plasma heating equations the magnetic field in the reactor, H^R, is known everywhere for a given power delivered to the plasma, P_{diss}. We now assume that the reactor H^R field is excited by magnetic dipole equivalent sources at the coupling apertures. The required dipole moment is thus determined for a given P_{diss}. It is then a simple matter to relate the dipole moment to the magnetic field in the cavity, H^C. Knowledge of this field in turn will then give its source current on the input coupling structure. The terminal current on this

structure can then be calculated and since the input power is known (P_{diss}), and $P_{diss} = I^2_{drive} R_{drive}$, the driving point resistance is determined.

We begin by determining the source currents necessary to produce the required reactor fields. We assume that

$$\bar{H}^R = \sum_m B_m \bar{H}^R_m \tag{6}$$

where B_m is the amplitude coefficient of the mth normal mode field $\bar{H}^R_m$ normalized according to Eq. (2). For a surface distribution of magnetic current, $\bar{m}_s$, on the reactor wall, one finds for a particular mode m,[1]

$$(\omega_m^2 - \omega^2)\, B_m = - i\omega \iint \bar{m}_s \cdot \bar{H}^{R*}_m \, ds \tag{7}$$

where ω_m is the resonant mode frequency. In order to simplify the analysis for our case, we will assume a single mode exists in the reactor, hence m = 1. Since the coupling apertures are small with respect to a wavelength, each aperture can be accurately represented by a single magnetic dipole of moment $\bar{M}$ rather than a surface distribution of magnetic current. The integral on the right hand side of Eq. (7) can then be written as $\sum_{j,k} i\omega\mu_o \bar{H}^{R*}_m(r=a)\cdot\bar{M}_{jk}$ where $\bar{M}_{jk}$ is the magnetic moment of an aperture of the jth column and kth row of the array. With the further assumption that the reactor Q > 10,

ω_m in Eq. (7) may be approximated as

$$\omega_m^2 \simeq \omega^2 (1 + i1/Q) \ . \tag{8}$$

Noting that both $\bar{H}_m^R$ and $\bar{M}_{jk}$ are z-directed and using Eq. (8) in Eq. (7), we obtain

$$B_m = -iQ \sum_{j,k} \mu_o H_m^{R*}(a) M_{jk} \ . \tag{9}$$

Furthermore, the magnetic moment of an elliptical aperture, small with respect to a wavelength, may be written as[3]

$$M_{jk} = \frac{4\pi \ell_1^3 e_a^2 H_{jk}^c}{3[K(e_a)-E(e_a)]} \tag{10}$$

where $e_a = (1 - (\ell_2/\ell_1)^2)^{1/2}$ is the eccentricity of the ellipse and $2\ell_1$ and $2\ell_2$ are its major and minor axes, respectively. In Eq. (10) $K(e_a)$ and $E(e_a)$ are elliptic integrals given by

$$\left.\begin{aligned} K(e_a) &\simeq \ell n(4\ell_1/\ell_2) \\ E(e_a) &\simeq 1 \end{aligned}\right\} \text{ for } e_a \text{ near unity} \ . \tag{11}$$

To describe the field at the coupling apertures we refer to Fig. 4. The fields for the TE_{101} mode are given by

$$H_z^c = h_o^c \cos \frac{\pi y}{A} \sin \frac{\pi z}{C} \tag{12a}$$

$$E_x^c = i\, h_o^c\, n \left(1 + \frac{A^2}{C^2}\right)^{1/2} \sin \frac{\pi y}{A} \sin \frac{\pi z}{C} \tag{12b}$$

where $\eta(= 377\Omega)$ is the intrinsic impedance. Hence,

$$H^c_{jk} \cong h^c_o \cos \frac{\pi y_k}{A} \sin \frac{\pi z_i}{C} \quad . \tag{13}$$

For elliptic apertures with $e_a \sim 1$, we substitute Eqs. (10), (11) and (13) into Eq. (9) to obtain

$$B_m = -iQ \sum_{j,k} \frac{4\pi \ell_1^3 \mu_o H_m^{R*}(a)}{(\ell n\, 4\frac{\ell_1}{\ell_2} - 1)} \; h^c_o \cos \frac{\pi y_k}{A} \sin \frac{\pi z_j}{C} \quad . \tag{14}$$

We now express B_m in terms of an assumed power dissipated within the plasma. Let P_{in} be the power input per RF module and N be the number of modules. For the fast magnetosonic mode we can approximate the time-averaged wave energy density $<W>$ by $\frac{1}{2}\mu_o <\bar{H}^R \cdot \bar{H}^{R*}>$, and from the definition of Q, we have

$$<W> = \frac{QNP_{in}}{\omega V} \cong \frac{1}{2}\mu_o |B_m|^2 h^2_{mo} F_m (k_r a) \tag{15}$$

where V is the plasma volume. Using Eq. (12a) in Eq. (15) results in

$$|B_m| = \left(\frac{2QNP_{in}}{\omega}\right)^{1/2} \quad . \tag{16}$$

We now calculate the driving point resistance at the cavity feed point (y_o, z_o). We assume the coax line center conductor is connected to the wall of the cavity opposite the feed point. Hence, a cosinusoidal surface current is assumed on the coupling structure with a maximum at the wall, given by $\bar{J}_s = \frac{I_o}{4\ell} \cos(kx)\, \hat{u}_x$ where $k = 2\pi/\lambda_o$, and ℓ is the circumferential length of the structure. We now determine I_o from the known power input, namely

$$P_{in} = \frac{1}{2} \text{Re} \iint \bar{E}^{c*} \cdot \bar{J}_s \, ds \tag{17}$$

where the surface integral is evaluated over the coupling structure. For $B << \lambda_o$, we obtain for a structure uniform in x,

$$P_{in} = \text{Re}\,(ih_o^c)\, I_o \eta \left(1 + \frac{A^2}{C^2}\right)^{1/2} B \frac{1}{4\ell} \oint_c \sin\frac{\pi y}{A} \sin\frac{\pi z}{C} \, d\ell \tag{18}$$

where the contour integral is over the structure circumference centered at (y_o, z_o). Furthermore, since $I_{drive} \simeq I_o$, we have

$$R_{in} = 2P_{in}/I_o^2 \tag{19}$$

where R_{in} is the driving point resistance at the coax to cavity junction. Noting that $H_m^{R*}(a) \simeq (\mu_o V F_m(k_r a))^{-1/2} J_m(k_r a)$ and combining Eqs. (14), (16), (18) and (19) to eliminate B_m, h_o^c and I_o, we arrive at the following matching equation

$$R_{in}^{1/2} = \left(\frac{NVF_m(k_r a)}{Q\omega\mu_o}\right)^{1/2} \left(\ell n \frac{4\ell_1}{\ell_2} - 1\right) \eta \left(1 + A^2/C^2\right)^{1/2} B \left|\frac{1}{4\ell} \oint_c \sin\frac{\pi y}{A} \sin\frac{\pi z}{C} \, d\ell\right|$$

$$/2\pi \left|J_m(k_r a)\right| \ell_1^3 \sum_{j,k} \cos\frac{\pi y_k}{A} \sin\frac{\pi z_j}{C} \, . \tag{20}$$

Following a similar procedure, we obtain the cavity electric field distribution as

$$\left|E_x^c\right| = \left(\frac{NP_{in}VF_m(k_r a)}{2\mu_o\omega Q}\right)^{1/2} \left(\ell n \frac{4\ell_1}{\ell_2} - 1\right) \eta \left(1 + A^2/C^2\right)^{1/2} \left|\sin\frac{\pi y}{A} \sin\frac{\pi z}{C}\right|$$

$$/2\pi \left|J_m(k_r a)\right| \ell_1^3 \sum_{j,k} \cos\frac{\pi y_k}{A} \sin\frac{\pi z_j}{C} \, . \tag{21}$$

Equation (20) describes the possible locations of the coax feed point (y_o,z_o) coupling to a single fast wave eigenmode in the reactor through an array of elliptical apertures and matched to a coax of characteristic impedance R_{in}. From Eq. (21) a design constraint on high voltage breakdown may be imposed.

Let us now consider Eqs. (20) and (21) for NUWMAK parameters: $R = 5$ m, $a = 1.25$ m and $\omega = 2\pi \times 9.2 \times 10^7$ rad/sec, with the toroidal resonance conditions given by $k_{\parallel} = 20\ m^{-1}$, $m = 1$, $k_r a = 106$, $a_1 = -1.39 \times 10^{-4}\ m^2$ and $a_2 = -2.75 \times 10^{-4}\ m^2$. For a total input power of 80 MW through 4 RF modules, Eqs. (20) and (21) become

$$\left|\frac{1}{4\ell}\oint_c \sin\frac{\pi y}{A}\sin\frac{\pi z}{C}\,d\ell\right| = 6.96 \times 10^{-4}\,(R_{in}\,Q)^{1/2} \qquad (22)$$

and

$$|E_x^c|_{peak} = 456\ Q^{-1/2}\ \text{kV/cm} \qquad (23)$$

where a 12 x 4 array of elliptical apertures with $2\ell_1 = 6\ell_2 = 15$ cm as shown in Fig. 12 in Sec. V is assumed.

Both the position of the feed and shape of the coupling structure are design parameters that can be used to advantage to match the coax drive line properly to the cavity. For a 30Ω coax drive line of 30 cm outer diameter the left hand side of Eq. (22) is bounded by

$$10^{-2} \lesssim \left|\frac{1}{4\ell}\oint_c \sin\frac{\pi y}{A}\sin\frac{\pi z}{C}\,d\ell\right| < 1\ . \qquad (24)$$

From Eqs. (24) and (22), only certain combinations of the coax impedance R_{in} and the wave Q can be matched properly to a single toroidal eigenmode, namely, those with $R_{in}\,Q \gtrsim 206\Omega$. Shifting the poloidal mode number m

changes $F_m(k_r a)$ only slightly and the matching condition remains relatively stable. For the case of NUWMAK, a feed point of $y_o = z_o = 15.25$ cm at the upper left corner as shown in Fig. 12 in Sec. V has been chosen. For the above 30Ω coax located at the upper corner of the cavity, Q factors of the order of 10 can be accommodated. It should be noted that the collective summation over several modes in a reactor will tend to lower the axial wave magnetic field at the edge, raise the wave impedance there, and allow a match for the coax further from the corner of the external cavity. In addition, the peak electric field strength in the matching cavity will be reduced.

The implication of Eq. (23) on high voltage breakdown in the cavity is not as straightforward as it seems. For an RF frequency of 92 MHz, the wave period is short compared to the transit time of an electron between the cavity walls where the pressure is maintained below 10^{-4} torr and T_e is assumed to be 30 eV. Under this condition, ac multi-pactor breakdown has to be considered, which will be discussed in Section V-E for the coax.

IV.C. Coil Antenna

We have also considered an alternative method of coupling using a nearly self-resonant coil antenna type of structure. In general, there are two types of resonant coil antennas which can be used. The first kind is a center-fed half-wavelength dipole, open at its ends, which can be expected to have a relatively low driving point resistance. The second kind is the same as the first except that the structure is shorted at the ends, as shown in Figure 5. Since this antenna is driven at a high voltage point, the driving point resistance can presumably be raised to match the 30 ohm coaxial line feeding the antenna.

We have calculated, in a rudimentary fashion, the loading resistance for the two kinds of antennas, each coupling to a single fast wave eigenmode in NUWMAK, to assess the possibility of matching. To obtain a realistic picture for the plasma, we have adopted a two-step density profile model over the minor cross-section. The coil antenna is assumed to be located in the low density region at the wall. Preliminary analyses, assuming that the low density region approaches a vacuum, show that for open-ended antennas,

$$R_L \propto Q \, |J_m^2(k_\perp a)| \, F_+^2(m,\Delta\theta) \tag{25a}$$

while for short-ended antennas,

$$R_L \propto \{Q \, |J_m^2(k_\perp a)| \, F_-^2(m,\Delta\theta)\}^{-1} \tag{25b}$$

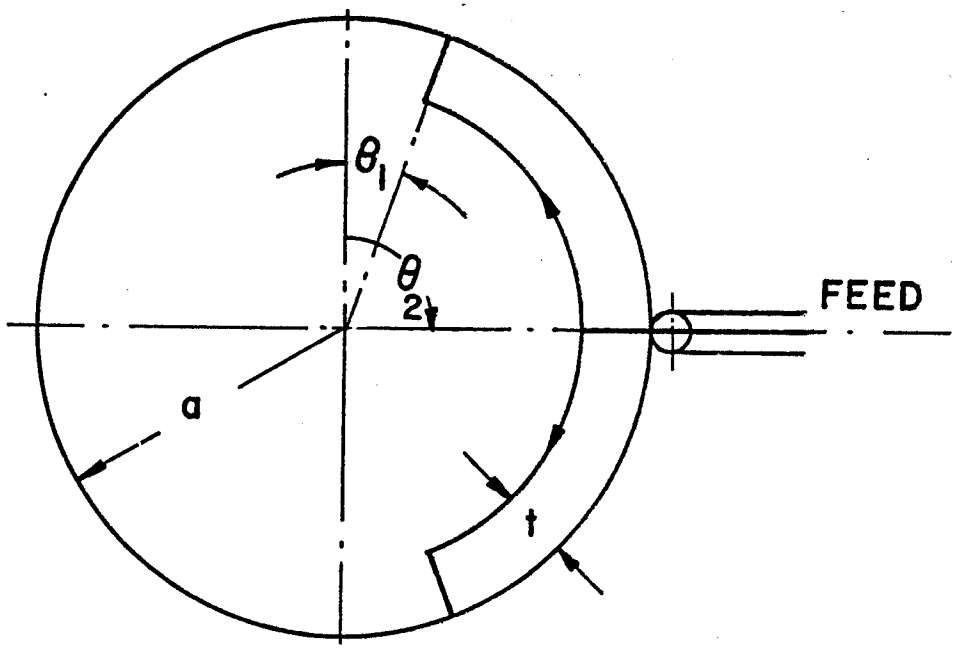

Fig. 5 Schematic of a center-fed half-wavelength dipole antenna.

where R_L is the loading resistance at the feed point, Q is the wave quality factor of an eigenmode of poloidal number m, a is the plasma radius and

$$F_{\pm}(m,\Delta\theta) = \frac{\sin(m\Delta\theta - \frac{\pi}{2})}{m - \frac{\pi}{2\Delta\theta}} \pm \frac{\sin(m\Delta\theta + \frac{\pi}{2})}{m + \frac{\pi}{2\Delta\theta}}$$

is the mode excitation coefficient with $\Delta\theta = \theta_2 - \theta_1$ being the poloidal angle the antenna subtends. In the context of the plasma model we adopted, it appears that matching at 30-50 ohms to low m single modes in NUWMAK is rather difficult to achieve unless the wave Q exceeds 1000. However, it is well-known that in a reactor-sized plasma the damping length of a fast wave mode due to cyclotron absorption is comparable to a toroidal circumference. If mode conversion to ion Bernstein modes is significant, a further drop in Q is expected. Thus, we assume that the Q for a fast wave mode in a reactor is between 10 and 50.

To get optimum coupling to a poloidal mode m via a self-resonant antenna requires the length of each coil to be $\frac{1}{2|m|}$ of the minor circumference, which means the frequency and hence the magnetic field have to be properly adjusted. These conditions cannot always be met in real situations.

By examining Eqs. (25a,b) and noting that $H_z \propto J_m(k_\perp r)$, we observe that the wave toroidal field H_z at the edge is extremely low compared to its peak value towards the core, resulting in a mismatch with the coax feed. If the plasma density is decreased, $k_\perp$ will drop resulting in a more gradual fall of the field amplitude in the radial direction. With

a decrease in plasma radius, $J_m(k_\perp a)$ will approach unity, making matching a much easier task, as found in small tokamaks. Thus, we believe that if a radial density profile is assumed and the wave equation properly solved by numerical methods, the matching problem should be greatly improved.

There are also engineering methods by which we can externally match to a low Q mode, such as

(i) Increasing the number of modules and the number of antennas in each module.

(ii) Connecting antennas in each module in parallel and matching each antenna to a coax feed of $R_L = N_m Z_o$, where N_m is the number of coils in each module and Z_o is the impedance of the main transmission line.

(iii) Feeding the antenna asymmetrically.

Although the problem of matching of a self-resonant coil antenna has not yet been solved completely, a preliminary engineering design of the coil antenna system is proposed and detailed in the next section, as an alternative to the cavity antenna.

References

1. R. F. Harrington, Time Harmonic Electromagnetic Fields, McGraw-Hill (1961), pp. 432-434.

2. R. E. Collin, Field Theory of Guided Waves, McGraw-Hill (1960), p. 291, Eq. 59.

3. Ibid, p. 298, Eq. 68b.

V. The Radio-Frequency Heating System for NUWMAK

A. Introduction

In the conceptual design of the NUWMAK tokamak fusion reactor, the radio-frequency (RF) supplementary heating method in the ion cyclotron range of frequencies (ICRF) is employed. It is proposed to launch the fast magnetosonic wave into a 50-50 DT plasma and heat the ions at the second harmonic cyclotron frequency of deuterium.

Most of the present-day magnetic fusion reactor designs advocate the use of neutral beams for heating and fueling purposes. However, as a supplementary heating scheme, RF has its potential advantages over beams which should not be overlooked. For instance, the technological demands for a successful RF heating system appear less severe than for the injection system in terms of high-power source development. With a properly designed RF system, the problem of material and equipment damage caused by prolonged radiation and neutron bombardment can be minimized. On the other hand, in the beam injection scheme the line-of-sight requirement places the beam accelerator directly in the path of neutron and radiation outflux from the plasma and results in a very stringent design criterion.

The RF supplementary heating system consists of the wave generator, the transmission line and the coupling structure. The wave generating system is responsible for producing an RF pulse of the required power level, frequency and duration during the start-up phase of the reactor duty cycle. The transmission system delivers the RF energy to the wave launching structure inside the reactor chamber, where the wave energy is coupled into and absorbed by the plasma.

In the design considerations outlined in the following sections, emphasis will be placed on the engineering problems associated with high power transmission and coupling to the plasma in a reactor environment. In particular, the problem of high voltage breakdown and the choice of structural materials to withstand radiation damage will receive special attention. For simplicity, only the fast magnetosonic wave heating scheme in the ion cyclotron range of frequencies will be presented. For lower hybrid wave heating, for example, the transmission and antenna design criteria are quite different, being in a higher frequency range, and have been dealt with in other works[1],[2].

Because of the preliminary nature of this work, alternative design schemes have been presented. As much theoretical calculation as possible will be incorporated into the design consideration to support the feasibility of the resulting system. Due to the limited scope of this work, no detailed cost analysis of the RF engineering system has been undertaken. But it is believed that the RF system cost will comprise only a small portion of the total estimated cost for building the reactor. Finally, it should be pointed out that much theoretical and experimental work has yet to be performed to provide a concrete understanding of the high power behavior of RF systems under the reactor environment. It is hoped that future experiments on large tokamaks such as PLT, TFTR and JET may just serve this purpose.

V.B. The Wave Generating System

The design of an efficient wave generating system is closely related to the amount of energy needed to heat a plasma the size of NUWMAK to ignition. Once ignition is reached, the sharply increased production of alpha-particles provides further heating of the plasma. A point is finally reached when the RF can be turned off while the plasma approaches a sustained burn condition, relying completely on alpha-particle heating.

Assuming that before the RF is on, the plasma has reached a temperature of 1 keV by Ohmic heating and that the RF pulse is turned off at about 8 keV after ignition, the required input of energy to the plasma is about 100 MJ for NUWMAK. Taking into account the losses through radiation, energy transport, and impurity heating, a conservative estimate of 240 MJ of RF energy will be needed. To optimize the duty factor of the burn cycle, an RF pulse of 1 to 3 seconds duration is desirable in the start-up phase of the Ohmic heating current. This implies a minimum power requirement of 80 MW for 3 seconds which translates to 20 MW per module for a system of four RF transmission ports. The wave generating system design specifications can be summarized as follows:

Total power transmitted at first wall	20 MW/port for each of 4 ports
Maximum pulse duration	3 sec.
Pulse repetition period (burn cycle)	245 sec.
Nominal center frequency	92 MHz

The frequency of 92 MHz in the table corresponds to the second harmonic ion cyclotron frequency of deuterium on the toroidal axis of the minor cross-section. For this reason, the idea of driving the RF system with super-power oscillators with drifting frequencies tuned to the loading circuits is not very practical. By far, the most efficient RF generator uses the driver, exciter and high-power amplifier (HPA) combination[1], which delivers full power into a matched load at a fixed frequency.

For reasonable operating conditions and design simplicity, power tubes capable of delivering at least several megawatts CW for 3 seconds at 92 MHz have to be used. At this frequency and power range, the RCA "coaxitron" is recommended as the HPA unit. A "coaxitron" is a super-power triode upgraded to the 100 MHz range by including the tuned cavities as part of the vacuum envelope. However, "coaxitrons" of MW-level power output are not presently available although their development is not believed to be a major technological problem and should pose no serious obstacle in the overall development of the RF system. Assuming that 5 MW "coaxitrons" are available in the future, four such units will be needed for each module, making it a total of sixteen units for the entire system.

Presumably, conventional power tubes, such as tetrodes, can be modified to meet the frequency and power demands for the NUWMAK RF system. In this respect, RCA[3] recently came up with the A3012, a liquid cooled super-power beam power tetrode, which has capabilities with some modifications of generating large amounts of

power within one vacuum enclosure. At present, they have a tube and circuit capable of over 50 kW of C.W. power at 100 MHz which can serve as a drive source for the larger tube. However, modification of the A3012 will not be undertaken until a sufficient market is assured to justify the expenditure.

The schematic of a module of the proposed RF generating system[2] is outlined in Figure 1. Power is drawn independently from the utility line, passed through a series of high-voltage step-up transformers and subsequently converted to DC by means of an SCR bridge converter. It is then fed in parallel to four ignition turn-on switches, each of which produces a DC pulse of 3 sec duration for every 245 sec. Any remaining ripples in the pulse can be filtered out by a low-pass capacitive network and the pulsed energy is then used to drive four HPA-IPA (intermediate power amplifier) units in parallel. Each HPA is composed of either a super-power tetrode or coaxitron with an output capability of 5 MW while the IPA consists of a high power (50kW) tube driven by a 92 MHz signal generator.

To ensure continuous and safe operation, a fault detecting circuit is included in the system. Connected in series with the transmitter is the fault detector consisting of a saturated time delay transformer (STDT) which acts as a current limiter when an arc is drawn in either the transmission or coupling system. The STDT also initiates a switch-regulator tube to remove the high voltage from the amplifier circuit in case of an arc fault. If the arc persists for more than a cycle, the crowbar will be energized through a crowbar time delay (CTD) circuit and the main power line will be disconnected by mechanical vacuum circuit breakers.

For this design, all switching and crowbarring will be performed at 40 kV levels and 125 A, which may necessitate a moderate improvement in tube technology. In the absence of an energy storage unit, the pulsed nature of the load will create disturbances on the main line and increase operation costs through "peak demand charges" by the utility company.

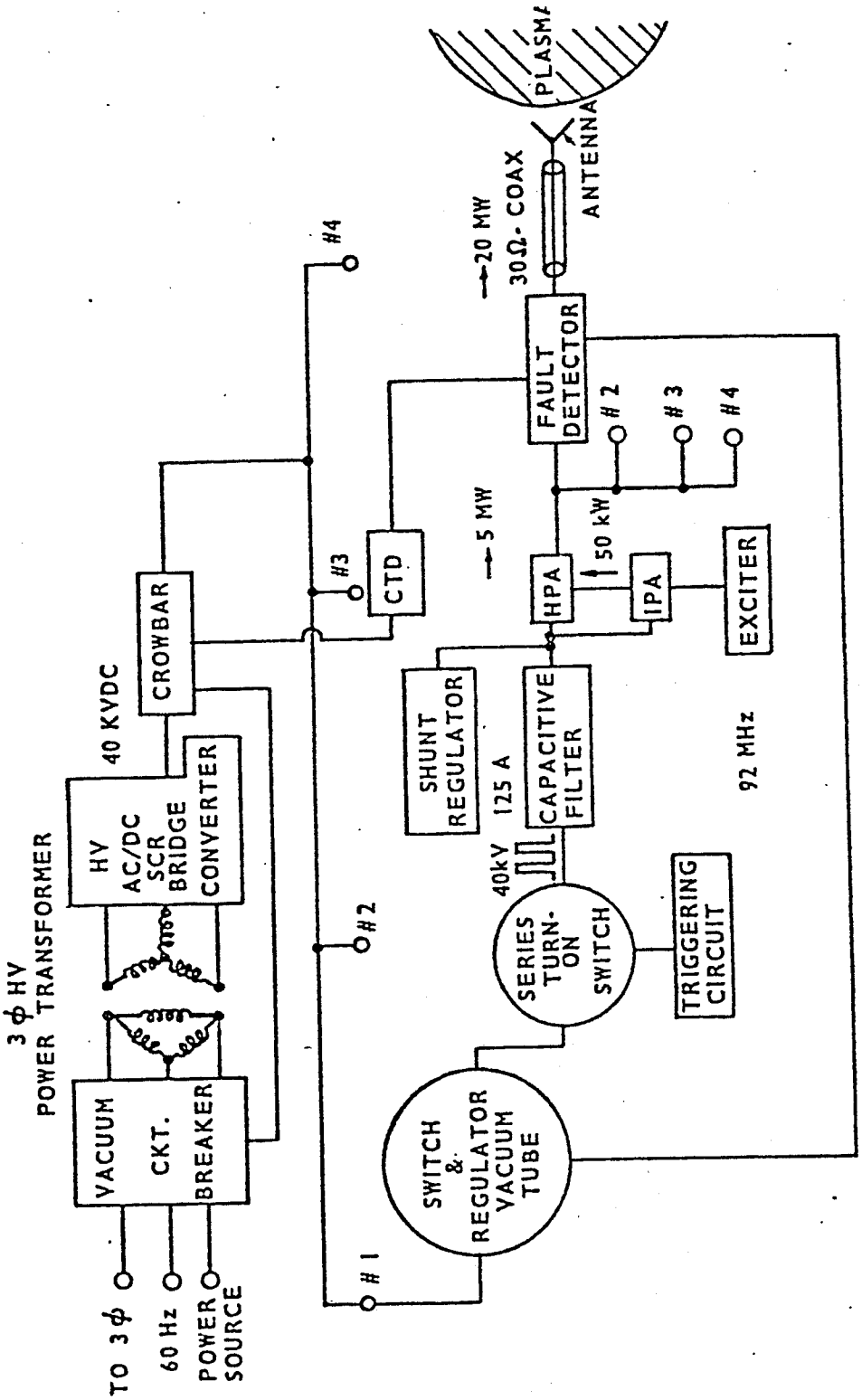

Figure 1 Schematic of HV Power Supply and Transmitter for One RF Module in NUWMAK

V.C. The RF Transmission System

The overall objective of the transmission system design is to choose or construct a transmission line capable of handling 20 megawatts of RF power at 92 MHz over a distance of 10 meters from the generator to the coupler. The requirement of handling megawatt levels of power precludes the use of open transmission lines, such as the slab line and the strip line. The enclosed transmission lines which can be considered are the coaxial line, waveguides (rectangular, circular or ridged) and balanced TEM lines.

Because the balanced TEM transmission lines are three-conductor systems, they are very difficult to construct and design as far as support, matching, and cooling are concerned. Therefore they will be ruled out of consideration in spite of their many advantageous features.

Waveguides are the most ideal transmission lines to work with basically because of their simple one-conductor geometry. However, in the ion cyclotron range of frequencies (ICRF), they are usually intolerably bulky and take up valuable space in the reactor walls. For instance, to propagate a TE_{10} mode in a vacuum-filled rectangular waveguide at 92 MHz will require a cross-section of a 1.63 m minimum width. Ridged waveguides filled with a ceramic material having a dielectric constant much greater than unity can considerably reduce the size of the system[4]. However, the dielectric medium will be directly exposed to neutrons and radiation from the plasma, and the choice of material which can withstand a continuous radiation loading of several MW/m^2 still awaits years of experimental testing.

In addition, there is a lower cutoff frequency for the dominant mode which, for a fixed-size waveguide, tends to limit the range of operating frequencies. The waveguide mode is inherently narrow band, imposing a restriction on the bandwidth of the generator.

By far, the coaxial line represents the most practical choice for high power transmission in the 100 MHz frequency range and is adopted by the NUWMAK group as the basic unit in the RF transmission system. There are many advantages of the coax over the other candidates and they are listed as follows.

Advantages of the Coaxial Line

(1) There has been ample experience in the industrial use of high-power coaxial lines, such as in radio stations, and in experimental design, with proven reliability.

(2) There is no low frequency cutoff.

(3) Because the TEM mode is the dominant propagating mode, the coax is inherently broad band. Thus a coax can easily be designed for a certain operating frequency without exciting the TE and TM modes.

(4) Although the coax is a two-conductor system which complicates the design of electrical components, its generally hollow center conductor can serve as a cooling pipe through which a coolant is circulated.

It is felt that enough industrial experience has been gained that the design of vacuum seals, tuning elements and dc breaks with coaxial lines can be achieved without a major technological advancement. Finally, through the use of rigid vacuum windows and quarter-wavelength stubs, insulating spacers may not even be needed to provide support for the center conductor.

(1) Design of the Coaxial Line

There are many types of high-power coaxial lines which are commercially available. As an example, the Prodelin Rigid "800" series[5] offers the following types:

Line Diameter (in.)	Characteristic Impedance (Ω)	Peak Power Rating (MW)
1-5/8	50	0.509
3-1/8	50	1.998
4-1/8	50	3.479
6-1/8	50	7.809
6-1/8	75	5.077
9.166	75	11.535

The peak power ratings given above are nearly constant with frequency and are based on a VSWR of unity and one atmosphere of dry air pressure at sea level and 50°C ambient temperature. Higher peak power ratings can be achieved by simply pressurizing with air or other gases having a dielectric strength greater than air. Sulphur hexafluoride, SF_6, with a dielectric strength twice that of air, is a commonly accepted choice. As an illustration, the curves[5] in Figure 2 show an increase in peak power ratings as a function of absolute pressure both in air and in SF_6. Usually if the cooling of both the inner and outer conductors is efficient, the coax can operate close to the peak rated power, especially when the RF pulse is short.

In coax design, there are a few basic equations which need to be considered. A simple cross-sectional view of a typical coaxial line is shown in Figure 3 together with the important design parameters. For a TEM mode, the field components are given by[6]:

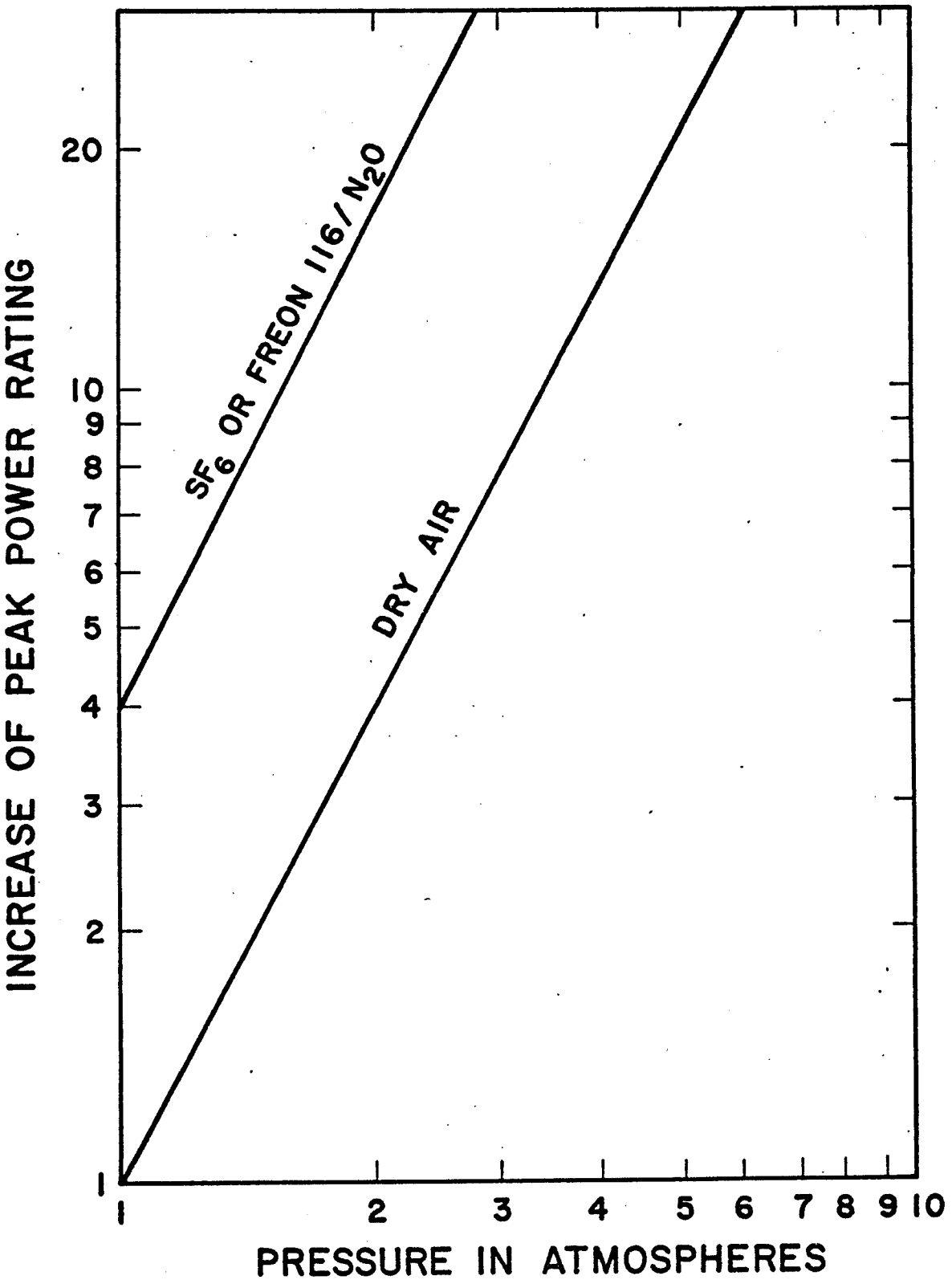

Fig. 2 Coax peak power ratings as a function of pressure and gas type. (Reproduced from Ref. 5).

a = OUTER RADIUS OF INNER CONDUCTOR
b = INNER RADIUS OF OUTER CONDUCTOR

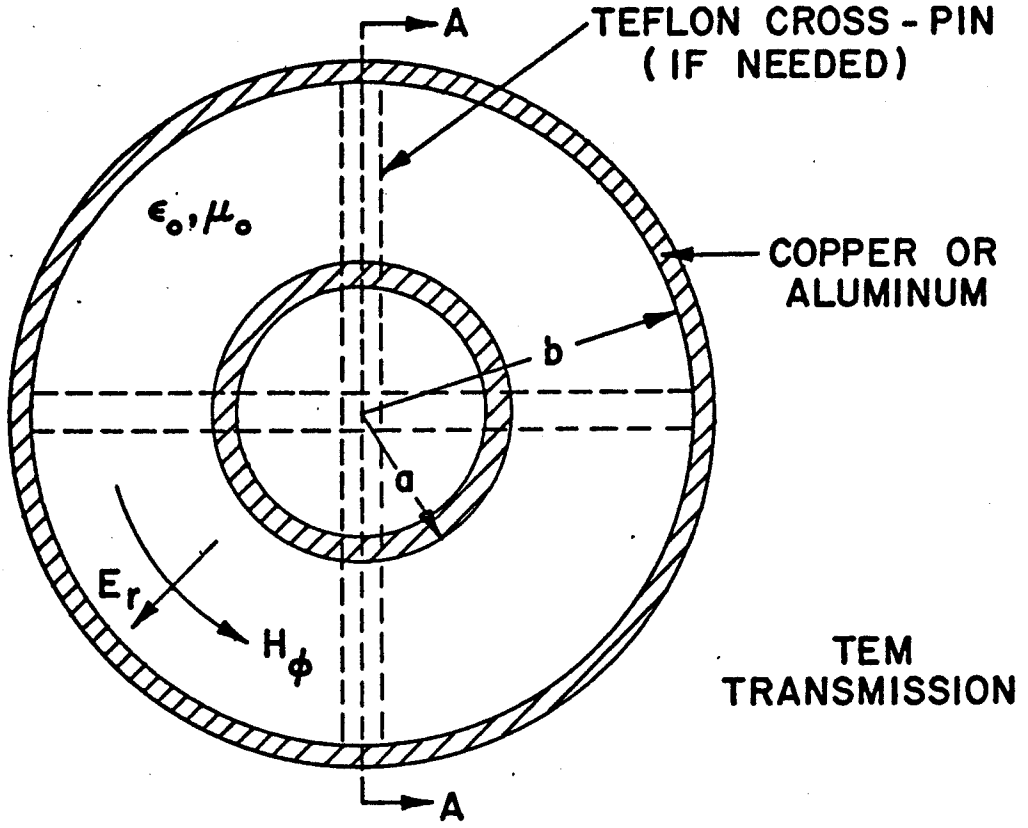

CROSS-SECTIONAL VIEW B-B

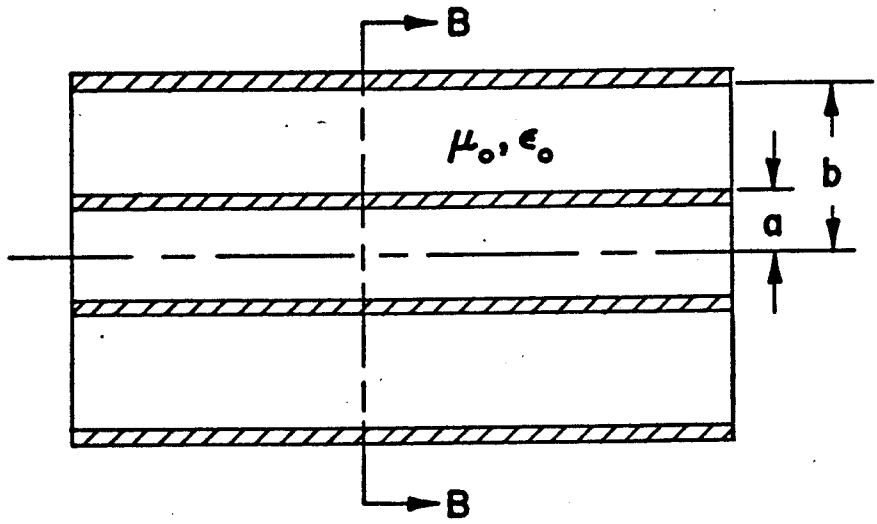

CUTOUT SIDE-VIEW A-A

Fig. 3 A typical coaxial line.

$$\vec{E} = \hat{r}\, E_o \left(\frac{a}{r}\right) e^{ik_o z} \qquad (1a)$$

$$\vec{H} = -\hat{\phi}\, \frac{E_o}{Z_o} \left(\frac{a}{r}\right) e^{ik_o z} \qquad (1b)$$

with the characteristic impedance

$$Z_o = \frac{1}{2\pi} \left(\frac{\mu_o}{\varepsilon}\right)^{1/2} \ln\left(\frac{b}{a}\right) \quad \text{(ohms)} \qquad (1c)$$

$$\text{and wave number } k_o = \omega\sqrt{\mu_o \varepsilon} \qquad (1d)$$

The total transmitted power is given by

$$P = \frac{E_o^2}{2Z_o} \left[a \ln\left(\frac{b}{a}\right)\right]^2 \quad \text{(watts)} \qquad (2)$$

and the attenuation constant α_w due to dissipation on the conductor surfaces is

$$\alpha_w = R_s \left(\frac{\varepsilon}{\mu_o}\right)^{1/2} \frac{(1 + a/b)}{a \ln (b/a)} \quad \text{(nepers/m)} \qquad (3)$$

with the surface resistance $R_s = (\omega\mu_o\rho/2)^{1/2}$ (Ω-m.), where ρ (Ω-m) is the resistivity of the conductor material. Copper and aluminum are the most commonly used conductor materials in commercially available coax lines. If one substitutes the dielectric strength of air divided by a safety factor (usually 2-3) for E_o in Eq. (2), one obtains the peak power rating of the coax at one atmosphere of dry air and 50°C ambient temperature. The dielectric strength of air is listed at 30 kV/cm.

It should also be noted that ρ, the metal resistivity,and hence α_w, are very sensitive to the temperature changes of the conductor.

In Figure 4 correction curves showing an increase in attenuation due to a rise in the inner conductor temperature are depicted[5].

Should support for the center conductor be needed, teflon or other ceramic cross-pins at intervals in the axial distance can be used. These pins can be designed and spaced appropriately along the axis to provide minimum wave reflection.

There are some design constraints on the efficiency of RF transmission in coax lines which need to be taken into account. For an air-insulated coax with a fixed size, minimum loss occurs at Z_0 = 73 Ω (b/a = 3.6) while maximum power handling capacity can be achieved at Z_0 = 30 Ω (b/a = 1.65). The commonly found line impedance of 50 Ω represents a compromise between the maximum power and minimum loss conditions.

One of the major concerns in designing a coax in a reactor environment is the heavy dose of radiation and neutron outflux it encounters for the portion in direct line of sight of the plasma. To date, there is little available experimental data on the effect of intense radiation on the performance of a coaxial line. The general consensus is that it enhances the possibility of breakdown in the coax. Therefore a safe margin will have to be established between the operating parameters and the maximum power rating in design considerations. The coax will be pressurized with static SF_6 to a pressure of one atmosphere, which will increase the maximum rated power by four fold (see Figure 2). However, to avoid chemical breakdown of the gas by neutron bombardment, the vacuum seal is located outside the reactor shield while coax bends near the first wall are desirable for reducing the number of energetic neutrons hitting the window.

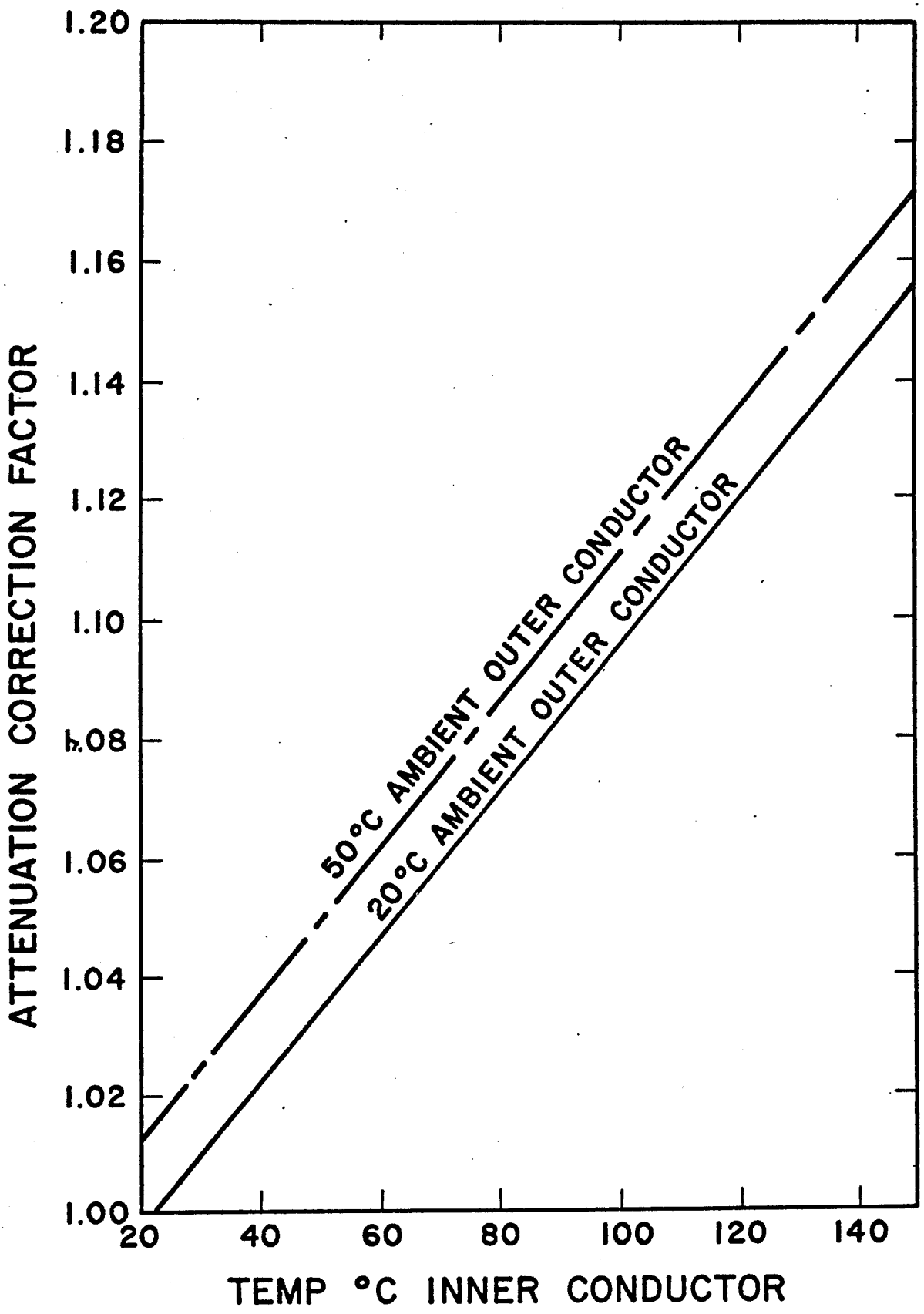

Fig. 4 Attenuation correction factor vs. temperature for coax. (Reproduced from Ref. 5).

Such a configuration will leave half of the entire coaxial line evacuated and reduce considerably the burden of the cryopumps if a gas-puffing scheme is used to refuel the plasma.

Since none of the commercially available coaxial lines have a power rating as high as 20 MW, a super-power coaxial transmission line needs to be deployed. Preliminary calculations indicate that in the ICRF the resistive losses will only be 1-2% of the total power over a length of 10 meters and sufficient cooling of the conductors will be achieved to permit operation close to the peak rated power. In this respect, a 30 Ω line looks particularly attractive. To maintain a safe operating condition, a conservative value of 12 in. is chosen as the outer diameter of the outer conductor. Assuming air insulation, the following parameters are obtained:

12" - 30 ohm Coaxial Transmission Line Characteristics

Material	Copper (vanadium + 5% Ti)
Insulator	Air
Outer conductor	12.000" O.D. x 11.800" I.D.
Inner conductor	7.152" O.D. x 6.952" I.D.
Characteristic Impedance	30 ohms
Peak power rating (safety factor = 3)	35.5 MW
E_o (r=a) at 20 MW	7.6 kV/cm
Attenuation constant α_w (50°C Ambient temp., 150°C inner cond.)	6.16×10^{-4} np./m.
Percentage power loss/10 m.	1.23%
Insulator supports (if needed)	Teflon cross-pins, spacing approx. $\lambda_o/2$, $\lambda_o = c/f$ (At f=92 MHz., $\lambda_o/2 \cong 1.5$ m.)

In a reactor environment, lower energy ions and neutrals tend to deteriorate the copper surface over a long period of time, resulting in

higher resistivity and power loss. Therefore, the part of the coax which is exposed directly to radiation near the coupler feed point should be made of a vanadium + 5% titanium alloy, which can withstand high radiation and neutron wall loadings in a reactor environment[7].

(2) Design of the Vacuum Window

As mentioned earlier, a pressurized coaxial line is used to alleviate the possibility of arcing over part of the transmission system. For this reason, a coaxial vacuum window is needed to seal off the pressurized portion of the line from the evacuated part.

First, the theoretical aspect of vacuum window design[6] is briefly reviewed. The cut-out side view of a typical coaxial window is shown in Figure 5. This window is assumed to be made of a ceramic material of dielectric constant $\varepsilon_r > 1$. Let P_i, P_r and P_t be the incident, reflected and transmitted power respectively in the axial direction. Assuming a lossless dielectric, the following power ratios are obtained:

$$|R|^2 = \frac{P_r}{P_i} = \frac{(\varepsilon_r - 1)^2}{(1+\varepsilon_r)^2 + 4\,\varepsilon_r \cot\beta'\ell} \tag{4a}$$

$$|T|^2 = \frac{P_t}{P_i} = \frac{4\,\varepsilon_r \csc^2 \beta'\ell}{(1+\varepsilon_r)^2 + 4\,\varepsilon_r \cot\beta'\ell} \tag{4b}$$

where $\beta' = \omega\sqrt{\varepsilon_r \varepsilon_o \mu_o}$ is the wave number in the dielectric medium and ℓ the axial length of the window. Note that in accordance with the lossless assumption, $|R|^2 + |T|^2 = 1$. It is immediately clear from Eqs. (4) that for minimum reflection, the condition

$$\ell = n\,\frac{\lambda'}{2}\,, \quad n = 0, 1, 2, 3, \ldots \tag{5}$$

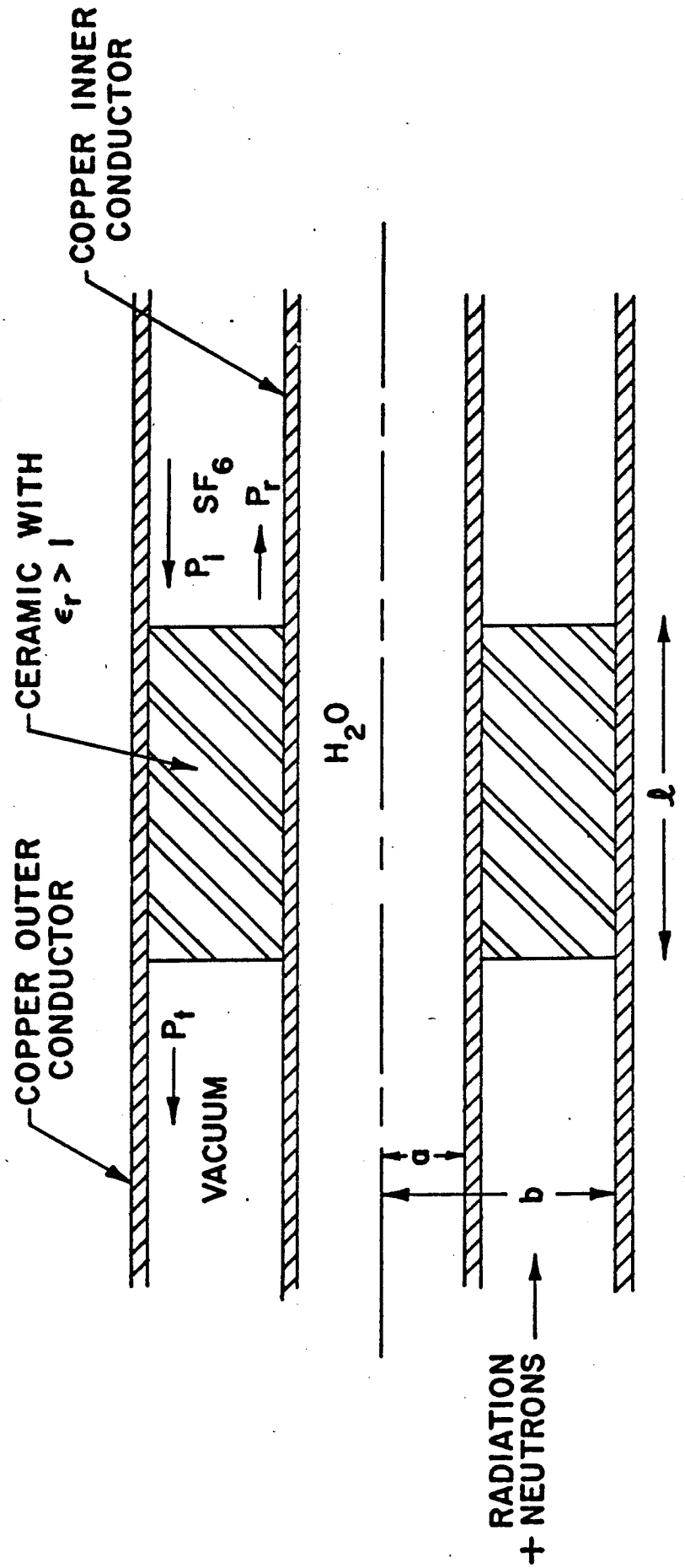

Fig. 5 Coaxial vacuum window configuration (side-view).

has to be met, where $\lambda' = 2\pi/\beta'$. As an illustration, the power reflection coefficient $|R|^2$ is plotted as a function of $\beta'\ell$ for $0 < \beta'\ell < \pi$ in Fig. 6, for $\varepsilon_r = 6.5$. It is clear from this curve that there are two practical configurations for the vacuum window, namely, (i) the thin window ($\ell << \lambda'$) and (ii) the half-wave window ($\ell = \lambda'/2$). A third useful configuration consists of two thin windows spaced $\lambda_o/2$ apart, where $\lambda_o = c/f$ with f being the wave frequency and c the speed of light in vacuum.

For the thin window structure, it can be seen from Fig. 6 that the window must be sufficiently short or wave reflection may become excessive. As an example, for a ceramic with $\varepsilon_r = 6.5$, a 5 cm. long window gives rise to a reflection coefficient of 0.065, which represents a 1.3 MW reflected power in a system carrying 20 MW of power. In addition, such a thin window may be insufficient for rigid support of the center conductor or may become brittle and crack after long periods of exposure to heavy doses of radiation.

The double-window configuration possesses some merits from an engineering point of view. The space between the windows can be used for cooling purposes but this is not essential if a ceramic with high conductivity is used. The windows tend to compensate for changes in their dielectric properties due to radiation damage so that the transmission coefficient remains stable. However, a standing wave is set up between the windows with a VSWR equal to

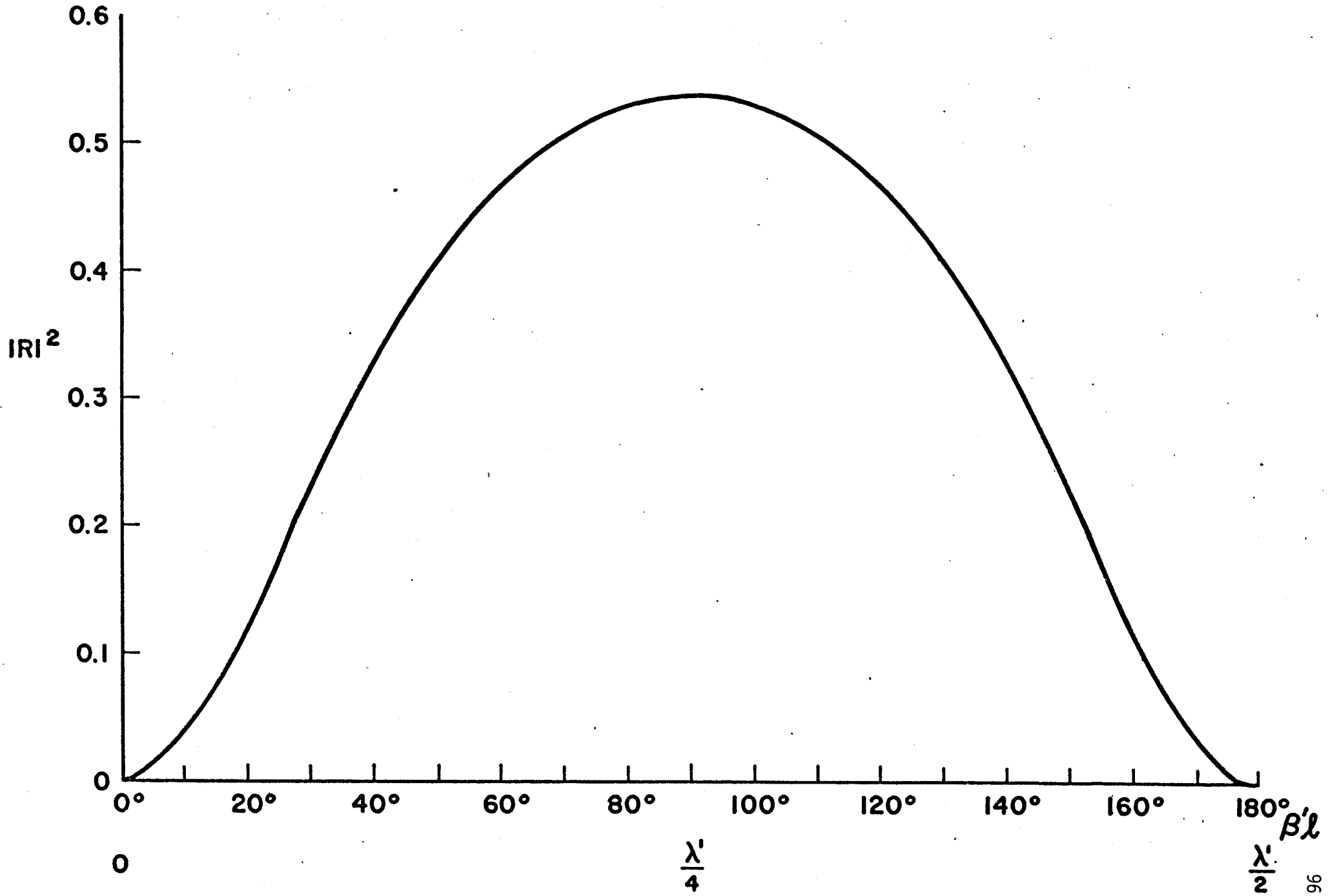

Fig. 6 Power reflection coefficient as a function of window length. ε_r = 6.5 for BeO.

$$\text{VSWR} = \frac{1 + |\rho|}{1 - |\rho|} \quad \text{where } \rho = \frac{\sqrt{\varepsilon_r} - 1}{\sqrt{\varepsilon_r} + 1}$$

For $\varepsilon_r = 6.5$, $\rho = 0.44$, VSWR = 2.57 and the peak electric field inside the window is increased by a factor of $1 + |\rho|$. Thus the peak power rating of the coaxial line has to be reduced by a factor of $(1 + |\rho|)^{-2}$, which is equal to 0.48 for $\varepsilon_r = 6.5$.

Based on the above arguments, the half-wave window configuration appears to be the best choice to fulfill its intended function. Because of the bulk size of this window, a ceramic with an exceptionally high thermal conductivity has to be used, as cooling is only provided by running water along the conductors of the coax. From the RF point of view, the ideal location of the vacuum seal in a pressurized line is at the first wall of the reactor where the antenna is generally positioned. However, the window will be exposed directly to a tremendous thermal energy throughput in the form of neutron and radiation flux. To date, tests[8] are still being carried out to find a window material which can absorb the kind of loading typical in reactor first walls without long-term deleterious effects. The most practical solution is to place the window outside the reactor shield and have bends in the coax near the first wall to reduce the number of energetic neutrons which may reach the window. In this configuration, the radiation loading at the windows is drastically reduced so that commonly used ceramics such as beryllium oxide (BeO) and aluminum oxide (Al_2O_3) can be considered.

A ceramic suitable for window construction in a reactor RF heating system should possess the following basic features:

(i) Highly resistant to radiation and neutron bombardment

(ii) High thermal conductivity

(iii) High specific heat

(iv) Low coefficient of thermal expansion

(v) Stable electrical properties under long periods of exposure to radiation and thermal stresses

(vi) Low loss tangent

(vii) High surface dielectric strength

Under a mild radiation environment, beryllium oxide is the most ideal ceramic to use, primarily because of its very high thermal conductivity and specific heat. However, more extensive tests should be performed to insure the stability of this material subject to repetitive pulses of 20 MW RF power over a long period of time. The extent of swelling under tremendous thermal stresses and interface effects in bonded ceramic-copper coax windows should also be investigated. For comparison, the properties of a few commonly used ceramics are listed in the following table:[9]

	Sintered Beryllia	Sintered Alumina	Sintered Yttria
Composition	99.8% BeO	99.8% Al_2O_3	99.8% Y_2O_3
Porosity (vol. %)	3-7	3-7	2-5
Fusion Temperature (°C)	2570	2030	2410
Max. Normal Use Temperature (°C)	1900	1900	2000
Density (gm./c.c.)	3.03	3.97	4.50
Specific Heat (cal./gm./°C)	0.50	0.26	0.13

	Sintered Beryllia	Sintered Alumina	Sintered Yttria
Linear Expansion (10^{-6} in./in./°C.) (20-1000°C.)	8.9	8.6	9.3
Thermal Conductivity (cal./sec./°C/cm)	0.500(100°C) 0.046(1000°C)	0.069(100°C.) 0.014(1000°C)	0.02(100°C) --------
Modulus of Rupture (psi)	20,000(100°C) 10,000(1000°C)	30,000(100°C) 22,000(1000°C)	-------- --------
Modulus of Elasticity (10^6 psi)	45	53	--------
Thermal Stress Resistance	Excellent	Good	Fair-Poor
Electrical Resistivity (1 MHz) (ohm-cm.)	10^{16}(23°C.) 10^9(500°C.)	$5x10^{13}$(23°C) 10^{13}(500°C.)	-------- --------
Dielectric (1 MHz.) Constant (100 MHz.)	6.7 6.5	9.6 8.0	-------- --------
Loss tangent (100 MHz.)	$7x10^{-4}$	10^{-4}	--------

From the table, $\varepsilon_r = 6.5$ for beryllium oxide at 100 MHz and the required length ℓ of the coax window is 64 cm at 92 MHz. The loss tangent of a dielectric is defined as

$$\tan\delta = \frac{\sigma}{\omega\varepsilon}$$

where σ is the conductivity under the operating conditions. For a loss tangent of 0.0007, $\sigma \simeq \varepsilon_r\varepsilon_0\ \omega \tan\delta = 2.91 \times 10^{-6}$ mhos/m. Then, with Eq. (1a), the radial profile of power dissipation in the window is found to be

$$P_{diss} = \sigma E^2 = 1.64\left(\frac{a}{r}\right)^2 \text{ watts /cm}^3 \qquad (7)$$

which is shown in Figure 7 so that a substantial portion of the heat

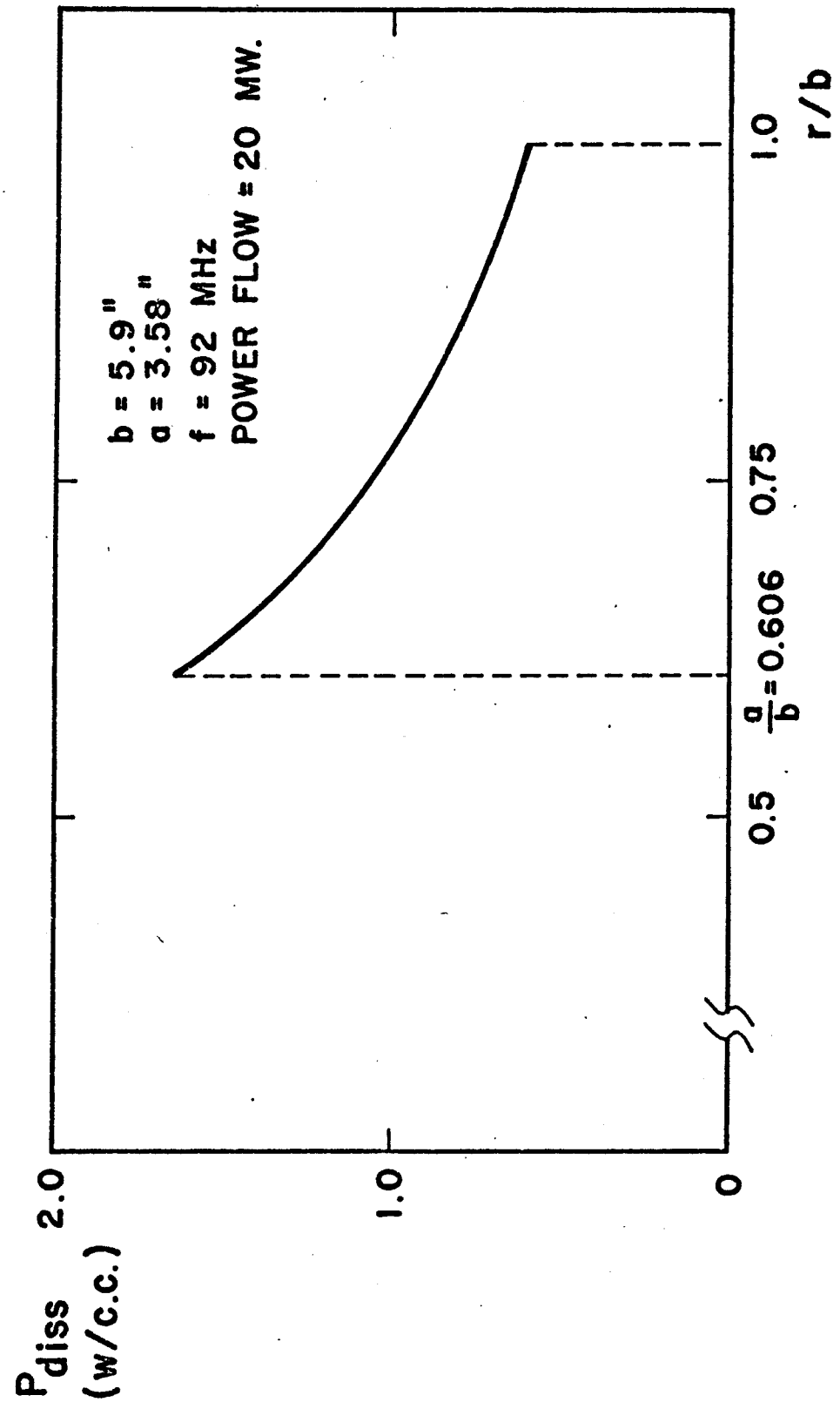

Fig. 7 Radial profile of RF dissipation in coaxial BeO windows.

is generated near the inner conductor surface. The total power dissipated over the entire volume of the BeO window is then

$$P_{total} = 2\pi\ell\ \sigma E_o^2\ a^2 \ell n(\frac{b}{a}) = 28.15\ kW \qquad (8)$$

This corresponds to 84.5 kJ of heat deposition over a period of 3 seconds for each burn cycle. For a specific heat of 1255J/kg °K at 100°C, a conservative estimate of a one degree centigrade temperature rise is predicted, if heat conduction is neglected.

In Figure 8 is shown the minor cross-sectional view of the basic orientation of the coax and the wave coupler with respect to the reactor blanket and the shield. This particular configuration indicates that the coax window is located between the blanket and the shield on the outside of the toroidal chamber. At the coax feed point to the coupler, the wall loading is at a maximum of 5 MW/m^2, which corresponds to a 16.2 $watts/cm^3$ absorption at the first wall. At the location of the window, the volume dissipation is reduced by several orders of magnitude to about 1.5×10^{-3} $watts/cm^3$ which corresponds to a total of 9.8 kJ over a burn time of 225 seconds. Compared to the number for RF power, an approximate 0.1 degree centigrade rise in window temperature is predicted for each cycle without cooling.

Combining the dissipative effects of RF and radiation, a temperature rise of 1°C is predicted over one duty cycle in the vacuum window made of BeO. However, this number is generally conservative and should drop significantly when thermal conduction is taken into account. Nevertheless, it is important that an efficient cooling system be devised to stabilize the temperature, and hence the electrical and mechanical properties, of the vacuum window.

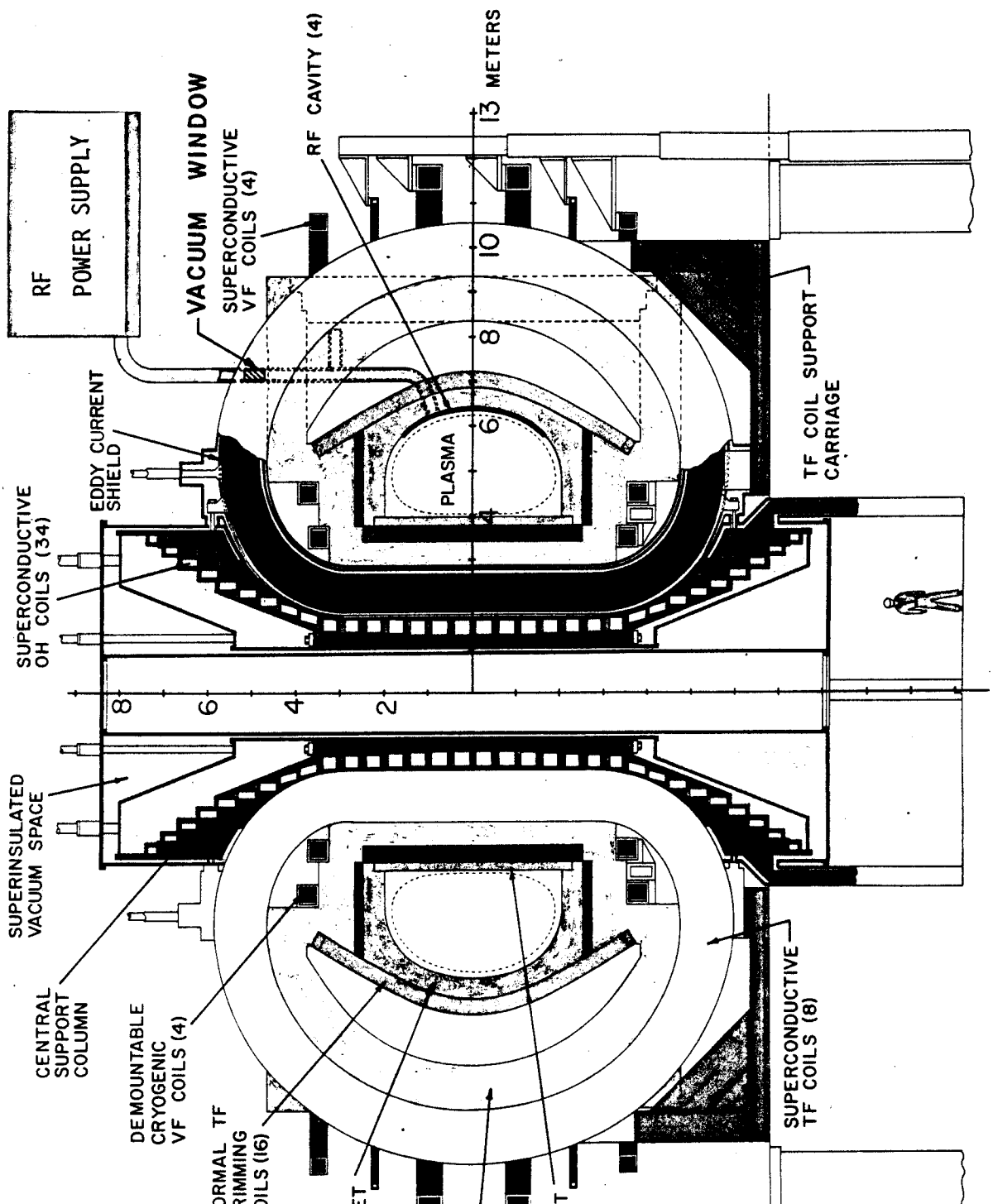

Fig. 8 Cross-sectional view of NUWMAK.

Preliminary calculations[10] also show that the RF power imposes a radial temperature gradient of less than 1°C across the window, while the corresponding value for radiation dissipation is much less than 1/3°C. Thus the stresses exerted by these thermal gradients are expected to be negligible over a reasonable period of time.

From Eqs. (4), it is evident that once ℓ is fixed, the performance of the window is very sensitive to changes in ε_r due to radiation damage. At the window position in NUWMAK, a neutron flux of 4.2×10^9 n/cm^2/sec is anticipated, which corresponds to a dosage (n.v.t.) of 1.3×10^{17} cm^{-2} over a period of one year[11]. Therefore an experiment to test the stability of the electrical parameters of beryllia under such a dosage should be undertaken to consolidate the above window design. If the change in ε_r is tolerable, the window may still have to be replaced once every year together with the first wall blanket. In the case of a highly unstable dielectric constant, additional shielding should be used or the double-window configuration may have to be considered.

(3) The Voltage Breakdown Problem

In designing a high-power RF system, it is essential to provide sufficient insulation to the system to prevent breakdown which may disrupt operation and inflict severe damage to equipment. Design problems related to high-voltage breakdown in the transmission system are considered for three separate regions, namely, the pressurized line, the evacuated line, and the vacuum seal.

(a) The Pressurized Line

For the most part, the coaxial transmission line is insulated with SF_6 at a pressure of one atmosphere. Within this pressure range, the motion of an electron is primarily dominated by collisions with the gas molecules. In the presence of a continuous electric field, the electrons maintain a constant drift velocity given by[12]

$$\vec{v} = \mu\vec{E} \tag{9}$$

where μ is the electron mobility given by $\mu \simeq \frac{e}{m_e\nu}$, with ν being the collision frequency. Since the velocity is in phase with the force, the electron absorbs a mean power[12]

$$\overline{P}_e = \overline{\nu\mu E} = \frac{e^2E_o^2}{2\, m_e\nu} \tag{10}$$

From this equation, one observes that the electron gas behaves essentially as a resistive medium. An electron-molecule collision may result in ionization of the molecule, producing more charged particles. If the process is allowed to continue, eventually a large number of charged particles will be accumulated. In the presence of a large electric field, an avalanche electron current is triggered, resulting in breakdown.

Free electrons which trigger the avalanche current can be produced by any one of the following processes:[13]

(i) Photoelectric emission in the gas or from the metallic conductors, caused by impinging gamma rays from a radioactive source or Bremsstrahlung radiation.

(ii) Thermionic emission from the conductor surface.

(iii) Secondary emission from the walls by electron or heavy ion impact.

(iv) Field emission from the wall due to an electric field normal to the surface, resulting in lowering of the work function.

(v) Emission by neutral atom or alpha-particle impact.

To prevent breakdown in a pressurized line, the most effective method is to use a gas with a high ionization energy or dielectric strength, since ionization is the main cause for such a process. Sulfur hexafluoride (SF_6), which fulfills the above requirements and is commonly used in industry, is apparently the ideal choice under the present conditions.

(b) The Evacuated Line

The prevention of breakdown in the evacuated portion of the coax presents a completely different problem from the one in the previous section. Two aspects of this problem need to be clarified. The first one is whether or not this region can be treated as a virtual vacuum as far as breakdown is concerned. The second one concerns the validity of dc breakdown theory under the prescribed conditions.

The NUWMAK reactor employs a gas puffing scheme to re-fuel the plasma from the low-field side of the chamber. Therefore, the scrape-off region and the vicinity of the coax feed to the coupler contains a weakly ionized plasma. It is reasonable to assume a 10% ionized gas, with $T_{neut.} \simeq 5$ eV and $T_i = T_e = 30$ eV, with a density of 10^{10} cm^{-3}. The kinetic pressure of the gas is 1.26×10^{-4} Torr. Apparently, this number is a little high since the presence of pumping ports in each blanket segment has been neglected.

The electron mean free path is calculated by

$$\ell_{mfp} = \frac{\langle v_e \rangle}{\nu} \qquad (11)$$

where $\langle v_e \rangle$ is the mean thermal speed and ν is the collision frequency. By including ν_{ei}, ν_{ee} and ν_{en} in ν, ℓ_{mfp} is found to be of the order of 10^5 m , while the interelectrode distance d is 6 cm. Thus

$$\ell_{mfp} >> d \tag{12}$$

which implies that practically no collision occurs during an electron transit between the electrodes. Thus one can treat the coax as a "vacuum"-insulated line and conclude that only emissions from the electrodes play a part in causing a breakdown.

When the RF frequency is sufficiently high such that the wave period 1/f is short compared to the transit time τ of an electron between electrodes, i.e., $f\tau \geq 1$ the dc breakdown theory is inadequate. For the coax system, $\tau = d/\langle v_e \rangle$, f = 92 MHz so that $f\tau \gtrsim 1$ implies $T_e \leq 142$ eV, while the estimated T_e is only 30 eV. Thus ac breakdown theory must be used for the evacuated coax.

For simplicity, consider two parallel electrode plates separated by a distance d and an electric field normal to the plates given by $E = E_a \sin(\omega t + \theta_o)$. Then the collisionless equation of motion for a free electron is[12]

$$\ddot{x} = - \frac{e}{m_e} E_a \sin(\omega t + \theta_o) \tag{14}$$

with $\dot{x} = v_o$ and $x = x_o$ at $t = 0$. The solution to Eq. (14) is

$$\dot{x} = v_o - \frac{eE_a}{m_e \omega} [\cos\theta_o - \cos(\omega t + \theta_o)] \tag{15a}$$

$$x = x_o + (v_o - \frac{eE_a}{m_e \omega} \cos\theta_o)t - \frac{eE_a}{m_e \omega^2} [\sin\theta_o - \sin(\omega t + \theta_o)] \ . \tag{15b}$$

Note that unlike the collisional case considered in the pressurized line, the electron velocity and the force acting on it are in quadrature, resulting in no energy absorption from the wave.

In the absence of collisions with gas molecules, multiplication of electrons is dominated by secondary-electron emission from the walls. Breakdown is then possible through a secondary-electron resonance or "multipactor" effect[14]. For a certain range of E_a and θ_o, the secondary-emission time phase angle, it is possible for electrons to travel from one electrode to the other in approximately one-half period (1/2f) of the wave field. When these "primary" electrons strike an electrode, they produce secondary electrons which are emitted in a reversed field and accelerated to the opposite electrode in half a cycle of the field. If the secondary-emission coefficient is greater than unity, repetition of this process will accumulate a large number of these oscillating electrons, eventually triggering an avalanche breakdown current.

Now, by setting $t = \pi/\omega$ in Eqns. (15) and letting $v_a = \dot{x}(t=\pi/\omega)$ and $d = x(t=\pi/\omega)$, where v_a is the arrival velocity of the electron, one obtains the following criterion for multipactor breakdown[14],

$$E_a = \frac{\omega^2 d}{(e/m_e)\,\Phi} \tag{16a}$$

where $\Phi = \frac{k+1}{k-1}\,\pi\cos\theta_o + 2\sin\theta_o, \qquad -60° < \theta_o < 18°$ (16b)

with $k = v_a/v_o$. The limits of θ_o are determined experimentally[14]. From Eqns. (16), it is evident that for fixed ω and d, there is a range of E_a values within which multipactor breakdown may take place.

Minimum E_a is reached when Φ is a maximum, with

$$(\theta_o)_{min} = \tan^{-1} \left(\frac{k - 1}{k + 1} \cdot \frac{2}{\pi}\right) \tag{17}$$

which gives k=3 for $(\theta_o)_{min} = 18°$. There is also a low end cutoff frequency f_{co}, below which it is impossible to trigger a multipactor breakdown. This cutoff frequency f_{co} can be roughly determined by the empirical relation

$$f_{co} = C_b/d \tag{18}$$

where $C_b \approx 79$ MHz-cm is found from experiments[14].

The multipactor breakdown analysis for a coaxial transmission line is relatively complicated due to the radially varying electric field. However, a good qualitative picture can be deduced if one assumes E_a to be the averaged electric field across the two conductors. This gives the relation

$$E_a = \frac{E_o a}{b - a} \ln \left(\frac{b}{a}\right) \tag{19}$$

which results in $E_a = 0.77\ E_o$ for the designed coax. The multipactor breakdown regime for the evacuated coax is plotted in Fig. 9. At f = 92 MHz, breakdown occurs for 0.175 kV/cm $< E_a <$ 0.8 kV/cm which translates to the range of power 0.019 MW < P < 0.385 MW. It is found[14] that if the rise time of the RF pulse is sufficiently short that $\Delta t < \frac{1}{2f}$, where Δt is the time interval for the line power to pass through the breakdown region and $\frac{1}{2f}$ corresponds to the electron transit time, multipactor breakdown may not be initiated. For f = 92 MHz, Δt must be less than 5.4 nsec., which is very unlikely to be achieved

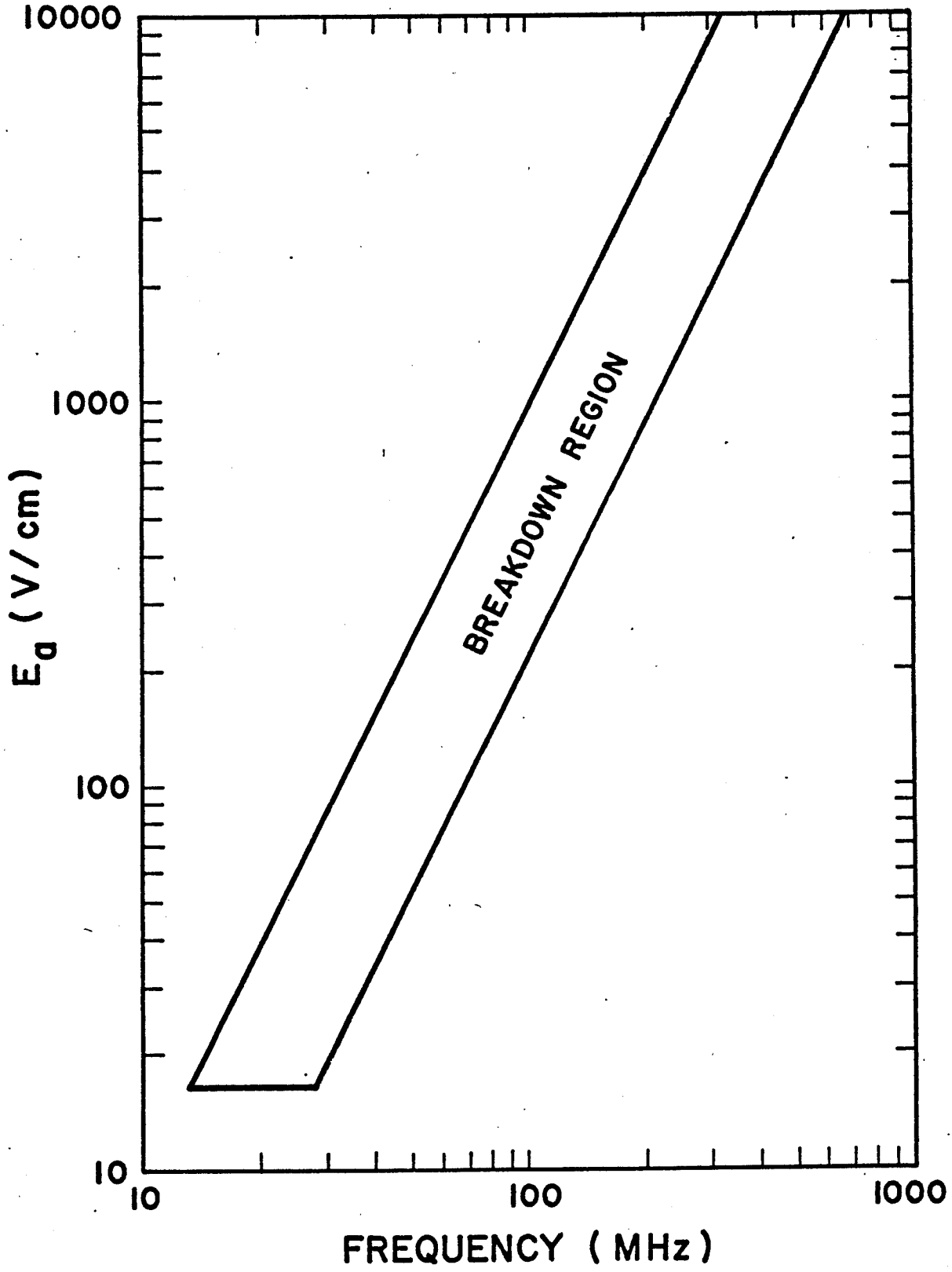

Fig. 9 Fundamental multipactor breakdown region; plate separation = 6 cm and $-60° < \theta_o < 18°$, k = 3.

due to the presence of shunt regulators in the generator. Thus some method to suppress this breakdown mechanism must be used. There are two commonly suggested techniques[1]:

(i) A thin coating (thickness < skin depth) of metal with a low secondary emission coefficient such as titanium on the conductor surfaces.

(ii) Surface grooving to introduce electric field inhomogeneities near the conductor surface.

It should be noted that the above multipactor analysis for the coax is only approximate. Clearly a theory involving the electric field variation in a cylindrical geometry should be developed to correctly determine the breakdown region. The effect of the presence of a magnetostatic field inside the coax should also be considered. Tests on the quenching mechanisms should also be conducted to determine their effectiveness.

(c) The Vacuum Window

Because of the difference in the dielectric constants of vacuum and BeO a standing wave is established inside the window. For ε_r = 6.5, the reflection coefficient is ρ = 0.44 and the VSWR = 2.57. Thus the field at the inner conductor surface (r=a) varies between 2.9 kV/cm and 7.5 kV/cm inside the window. The dielectric strength of BeO is listed as 94 kV/cm so that breakdown within the window is very unlikely. Surface breakdowns, especially those caused by surface multipactor effect, may cause trouble, but they can generally be suppressed by the methods mentioned in the previous section.

V.D. The Coupling System

The main goal of the RF coupling system design is to construct a launching antenna which couples wave energy efficiently to the plasma and is structurally sound to survive in a radiation environment found in NUWMAK. Several aspects of antenna design need to be considered.

(1) The antenna must be well matched to a vacuum-bounded toroidal plasma so that undesirable wave reflection at the first wall is minimized. This can generally be achieved by carefully choosing a wave mode at an appropriate frequency and wave number, or by the use of an impedance matching network. However, the matching circuit tends to create a large amount of reactive power between the tuner and the antenna. Thus the impedance matching concept is not highly recommended in this system.

(2) Due to the high power requirement, special emphasis should be addressed to the high-voltage arcing problem in the antenna structure.

(3) The coupler should be compact in size and positioned close to the first wall to avoid obstruction of the flow of plasma in the torus.

(4) The structure should be constructed of a radiation resistant material with a stable electrical conductivity so that losses can be kept low.

(5) An efficient cooling system should be developed to stabilize the temperature of the launcher during the burn cycle.

(6) The wave absorption mechanism should be properly identified to determine the wave mode to be launched. The spectral requirement for the wave should also be considered from the point of view of launching and absorption efficiencies.

In the NUWMAK reactor, the fast magnetosonic mode at the second harmonic deuterium cyclotron frequency (~ 92 MHz) is to be launched. This wave is approximately transverse electric (TE) with respect to the toroidal axis and is right-hand elliptically polarized. It can be coupled to the plasma through the poloidal electric field (E_ϕ) or the toroidal wave magnetic field (B_z). Waveguide[4] and balanced TEM line[1] coupling to the plasma in the ICRF have been previously investigated. In these configurations, the wide side of the line is aligned parallel to the toroidal axis so that the electric field points in the poloidal direction at the aperture. Up to this date, poloidal current loops, which couple through the B_z-field, have been employed successfully in RF experiments in present day tokamaks, such as ST, ATC and TFR.

Two coupler designs have been proposed for NUWMAK, one using a cavity-backed aperture antenna and the other a current loop. The latter scheme has been proven successful in smaller machines but may be susceptible to radiation damage in reactors, while the former has advantages mentioned in Sec. V-D. The cavity-backed aperture coupler needs extensive testing to evaluate its performance. It is felt that both plans should be developed in parallel until experimental results in the next generation of tokamaks are available to determine the final choice.

(1) The Cavity-Backed Aperture Antenna

The conceptual design of this antenna consists of a wedge coaxial cavity flush-mounted on the first wall of the torus as shown in Figure 10. The cavity is fed by a coaxial line on its outer wall, with the center conductor welded to the inner wall, forming

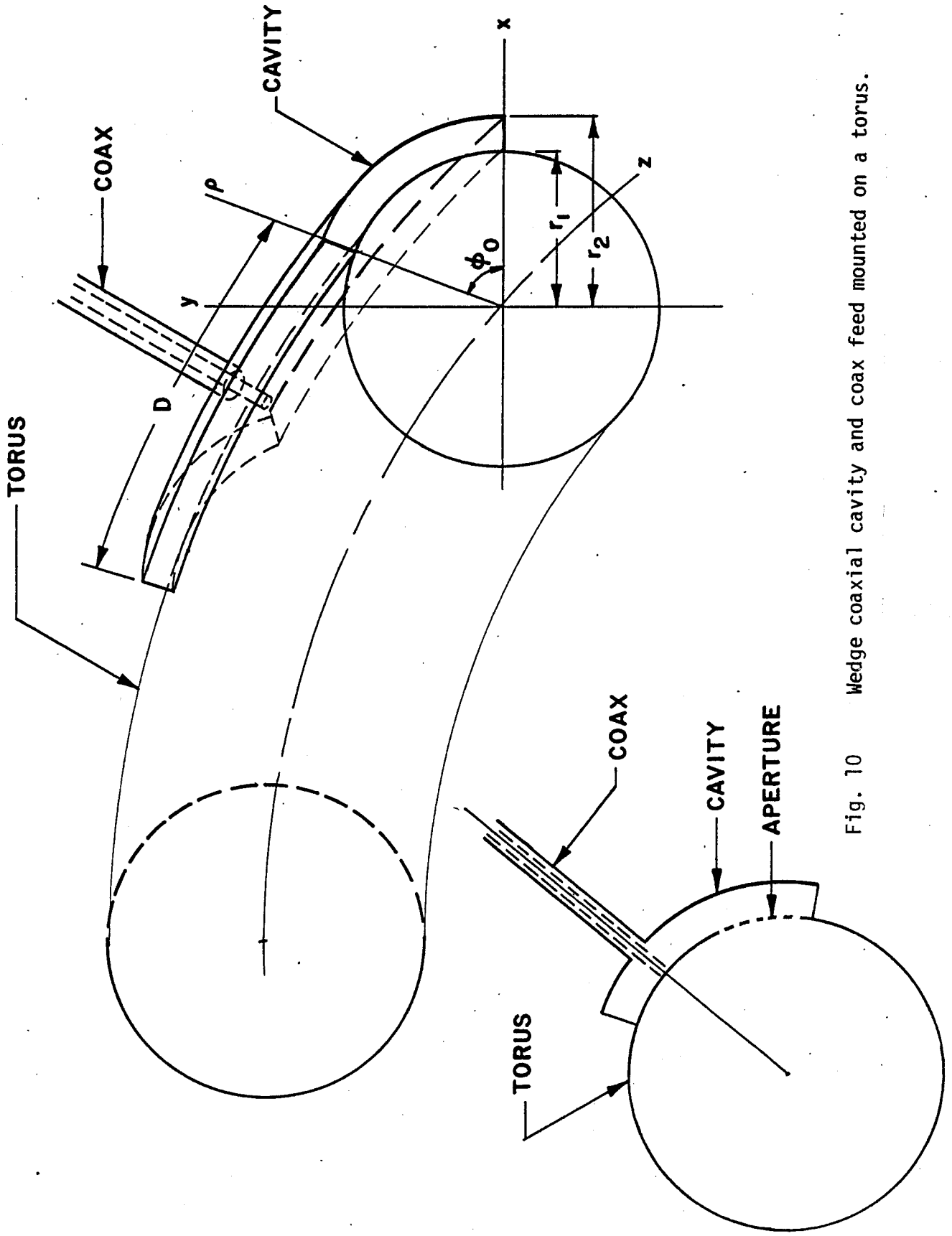

Fig. 10 Wedge coaxial cavity and coax feed mounted on a torus.

a current coupling loop. On the lower side of the cavity, an array of apertures is cut out which serves as an antenna radiating wave energy into the plasma.

To determine the condition for eigenmode excitation, one has to look at the field structure inside the cavity. With reference to Figure 10, the poloidal component of the electric field E_ϕ for the $TE_{mn\ell}$ mode in the cavity is[15]

$$E_\phi^{mn\ell} = k_\rho^{n\ell} B_{mn\ell} \sin(\tfrac{m\pi}{D} z) \cos(n\phi) \{J_n'(k_\rho^{n\ell}\rho) + A\, N_n'(k_\rho^{n\ell}\rho)\} \qquad (20)$$

where m, n, ℓ are the toroidal, poloidal and radial mode numbers respectively, with $n = p\pi/\phi_o$, ($p = 0, 1, 2, 3, \ldots$) and ϕ_o the poloidal angle subtended by the cavity. In Eq. (20), $k_\rho^{n\ell}$ is the ℓ th resonant radial wave number for poloidal n, J_n' and N_n' are derivatives of Bessel functions of the first and second kind with respect to the argument and $B_{mn\ell}$ is the amplitude factor for the mode. The boundary conditions of $E_\phi^{mn\ell} = 0$ at $\rho = r_1$ and $\rho = r_2$ yield the resonant condition

$$J_n'(k_\rho^{n\ell} r_1)\, N_n'(k_\rho^{n\ell} r_2) - N_n'(k_\rho^{n\ell} r_1)\, J_n'(k_\rho^{n\ell} r_2) = 0 \qquad (21)$$

for which the dispersion equation is given by

$$(k_\rho^{n\ell})^2 = \omega^2 \mu_o \varepsilon_o - (\tfrac{m\pi}{D})^2 \quad . \quad m = 1, 2, 3, \ldots \qquad (22)$$

Given p, ϕ_o (and thus n), m and ℓ, and the dimensions r_1, r_2 and D, one can determine the resonant frequency for the $TE_{mn\ell}$ eigenmode by using Eqs. (21) and (22). In particular, from Eq. (22), one notes that for given ω and m, the toroidal length D has to exceed a minimum value for a propagating mode, i.e., $(k_\rho^{n\ell})^2 > 0$.

The fundamental mode of oscillation in this cavity is given by the mode numbers: m=1, p=1 ($n = \pi/\phi_o$) and ℓ=1, which is equivalent to the TE_{101} mode in a rectangular cavity. Clearly it is desirable to excite only the fundamental cavity mode in the NUWMAK RF coupling system. The primary design calls for the cavity to be mounted on the outside wall of the torus, as shown in Figure 8. In spite of the D-shaped minor cross-section, the profile of the outer first wall is well approximated by a circular arc of radius r_1 = 2.4 m. For a 10 cm radial thickness ($r_2 - r_1$ = 10 cm), Eqs. (21) and (22) are solved numerically for the fundamental mode at an operating frequency of 92 MHz. The possible toroidal and poloidal widths of the cavity are plotted in Figure 11. As a comparison, the corresponding dimensions of a rectangular cavity for the TE_{101} mode are plotted in the same figure. Note that, except for operation near cutoff which occurs at ϕ_o = 39°, the simpler rectangular cavity analysis is evidently a very good approximation to that for the wedge coaxial cavity.

For the NUWMAK RF system, the following cavity parameters are chosen:

Resonant Cavity Parameters

Radial Width	10 cm
Toroidal Width	1.85 m
Poloidal Width	3.5 m
Wall Thickness	0.2 cm
Material of construction	vanadium + 5% titanium alloy

The vanadium + 5% titanium alloy is chosen as the material of construction because vanadium maintains a high conductivity under

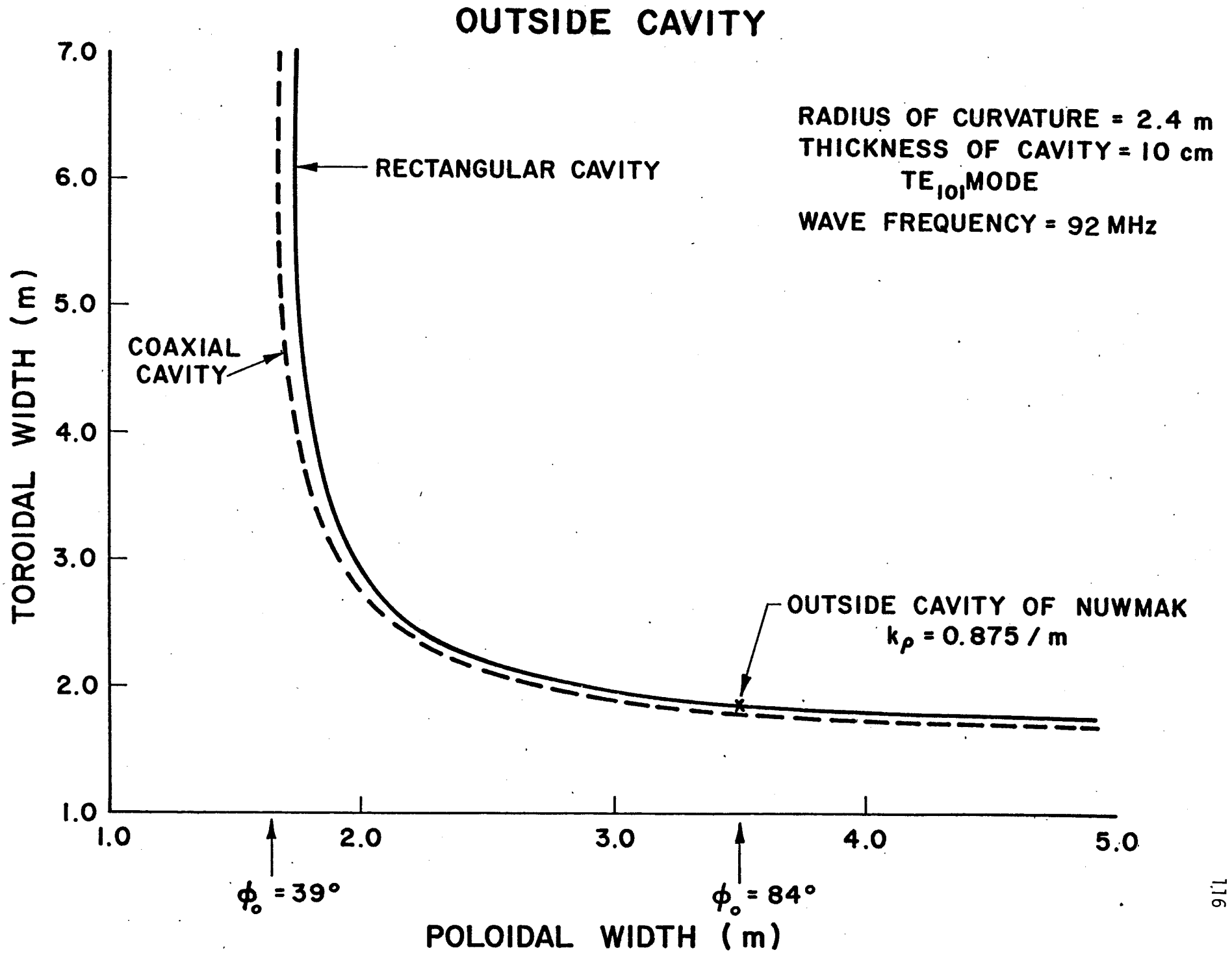

Fig. 11 Exact and approximate TE_{101} resonance curves for the poloidal and toroidal dimensions of the outer cavity at 92 MHz.

severe radiation environment and titanium is present to protect the surface from excessive damage by neutrals, neutrons and radiation. Cooling pipes containing running water are installed on the inside of the inner wall to maintain the first wall temperature at 300°C. These pipes also form grooves on the surface to prevent multipactor breakdown. The toroidal and poloidal dimensions of the cavity are chosen so that each unit can be mounted on a movable blanket segment and does not interfere with the pumping port located on the lower side of the outer first wall. The cavity is also positioned so that it does not intersect with the $\omega = 2\omega_{CD} = 3\omega_{CT}$ resonance surface (Figure 8) over its poloidal extent. Catastrophic breakdown may occur due to anomalous acceleration of the ions if the cavity intersects such a resonance surface.

Preliminary design of a launching array of apertures on the cavity has been considered. Coupling of the fast wave is achieved via the toroidal wave magnetic field, which is B_z in the cavity (Figure 10). For the TE_{101} mode, B_z reverses its direction from the upper to the lower poloidal half. In order that the fields radiated from the apertures do not cancel one another far away from the wall, the array is located entirely on the lower poloidal half while the coax is fed into the upper half on the opposite wall, shown in Fig. 12.

As discussed in an earlier section, a wave spectrum centered at $k_{\parallel} = k_z = 20\ m^{-1}$ is desirable if one wishes to minimize the effect of mode conversion[16] which complicates the picture of cyclotron absorption. For any array of apertures on the cavity, it seems inevitable that

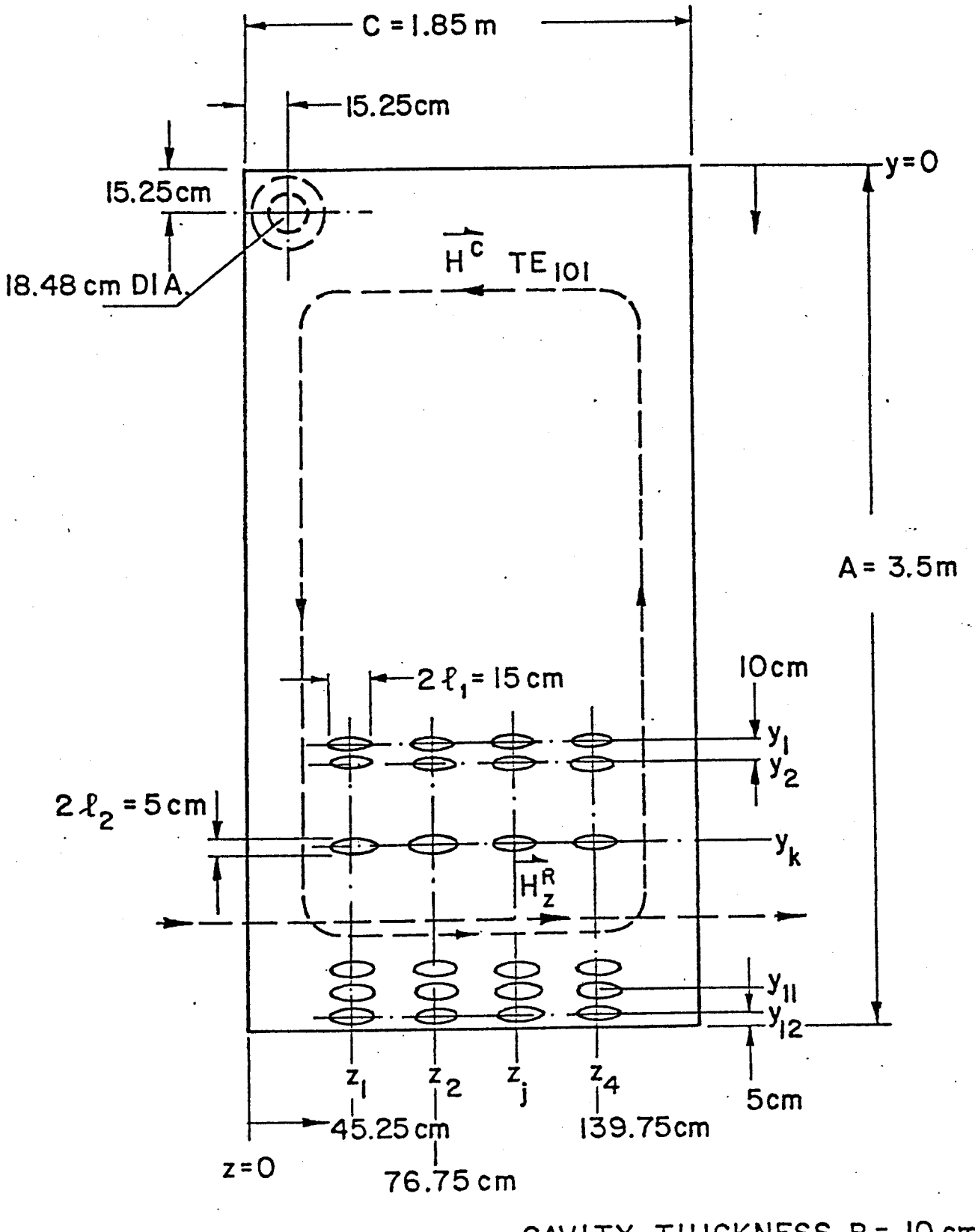

Fig. 12 Aperture array on outer cavity as viewed from the major axis

some $k_{\parallel} = 0$ component is always present in the radiated field. However, a sideband centered at $k_{\parallel} = 20\ m^{-1}$ can be achieved if the apertures are spaced 31.5 cm apart toroidally, which corresponds to one toroidal wave length. In Figure 12, an array of 12 x 4 apertures is drawn as a preliminary design. The holes are elliptical in shape to achieve optimal coupling efficiency[17] and to prevent breakdown at sharp corners.

A detailed theoretical analysis should be carried out to determine the wave number $k_{\parallel}$-spectrum of the radiated field from the array of apertures shown in Figure 12.

An auxilliary coupling system using the cavity-backed aperture antenna is shown in Figure 13. In this scheme, the cavity is mounted on the inner first wall where space is extremely limited. Thus the cavity thickness is reduced to 5 cm while the other dimensions remain the same as the outer cavity. A relatively sharp bend in the cavity is needed to accommodate the structure, but the rectangular cavity approximation is still valid above cutoff. The merit of this system is that the wave is now launched from the high field side and the mode conversion heating mechanism can be utilized and is particularly efficient for the $k_{\parallel} = 0$ wave component. Thus the aperture array design is much simpler than the previous one. However, the incorporation of this inner cavity into the reactor is considerably more complicated than for the outer cavity.

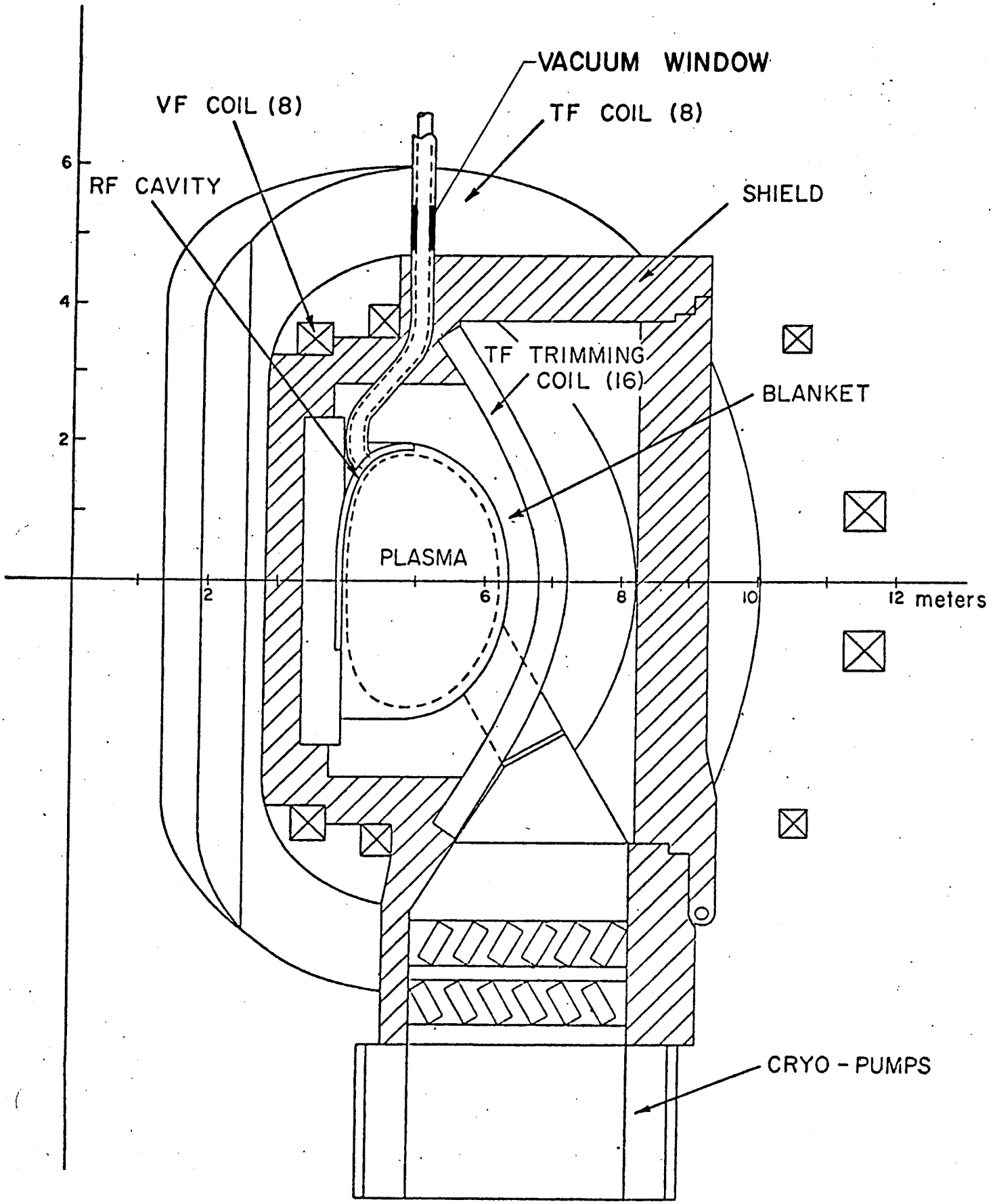

Fig. 13 Cross-section of NUWMAK between TF coils (with inner RF cavity).

As mentioned earlier, four RF modules are needed to deliver 80 MW of power over a period of 3 seconds. In Figure 14 is shown the top view of the NUWMAK reactor together with the location of the four resonant outer cavities and their coax leads. Each cavity is placed directly under a toroidal field (TF) coil, where field ripples are at a minimum, so that the plasma column remains stable during the RF pulse.

(2) The Coil Antenna

A parallel design of coil launching structures has been made because of their proven success in present-day machines. If properly designed and matched, very high coupling efficiencies (90%) can be achieved. In Figure 15, the basic scheme of such a system for NUWMAK is shown. The top view shows a total of four RF modules located on the outer wall of the toroidal chamber. Each module consists of a pair of coil antennas, driven in phase separately by coaxial transmission lines. For each antenna, a coax is fed through the first wall with the center conductor split poloidally to form two quarter-wavelength current loops connected in parallel along the minor cross-section circumference, as illustrated in Figure 15(b). For $f = 92$ MHz, $\lambda_0 = 3$ m so that each current loop is 75 cm long poloidally.

Because of the size of the coils and their coaxial feed lines, there is a restriction as to how close together they could be placed without affecting their coupling efficiency. For this reason, coil coupling to a wave field with a high toroidal wave number presents a formidable problem. To excite a wave with $k_{\parallel} = 20\ m^{-1}$, the two coax feeds in each RF module have to be 31.5 cm

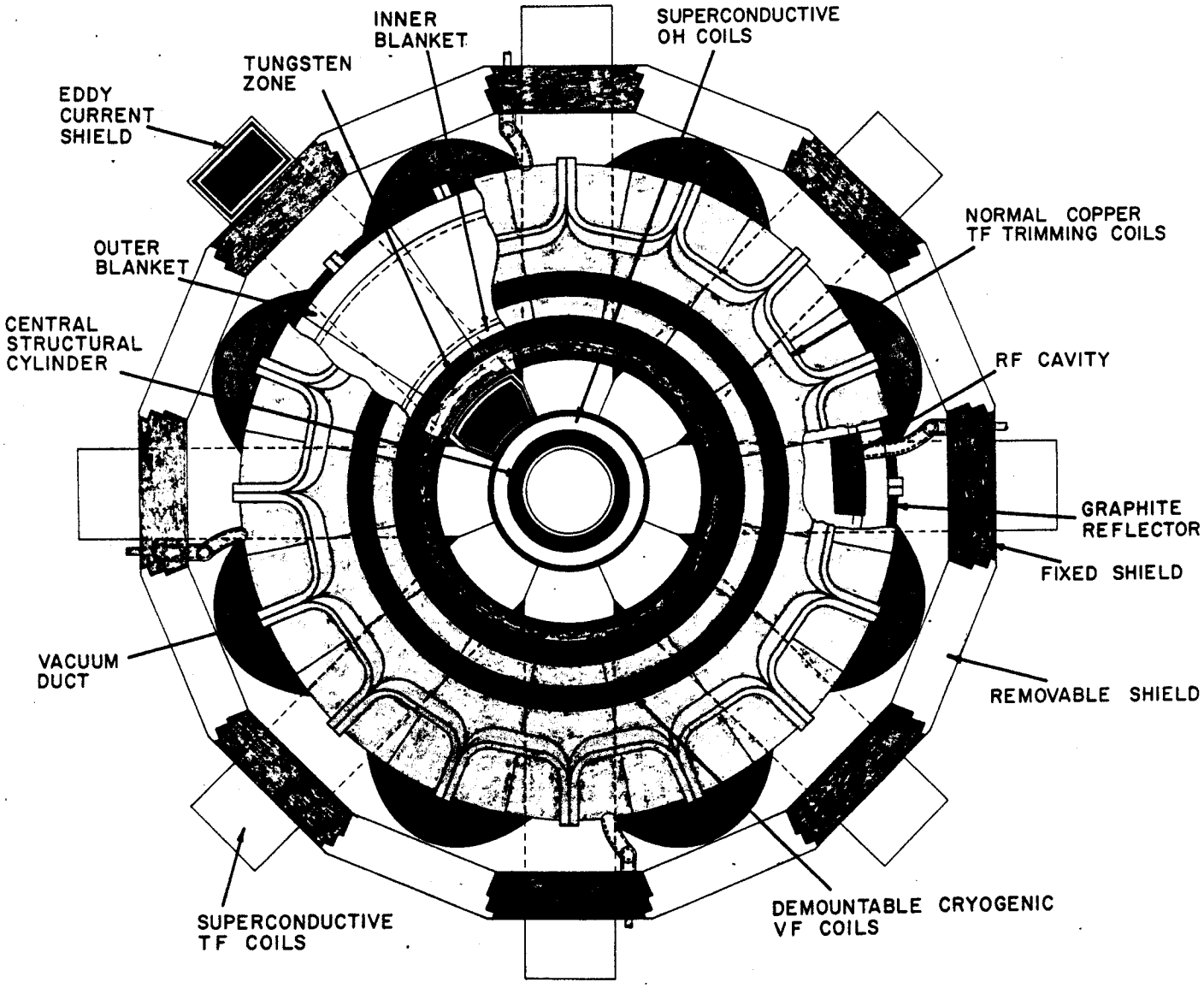

Fig. 14
Top view of NUWMAK.

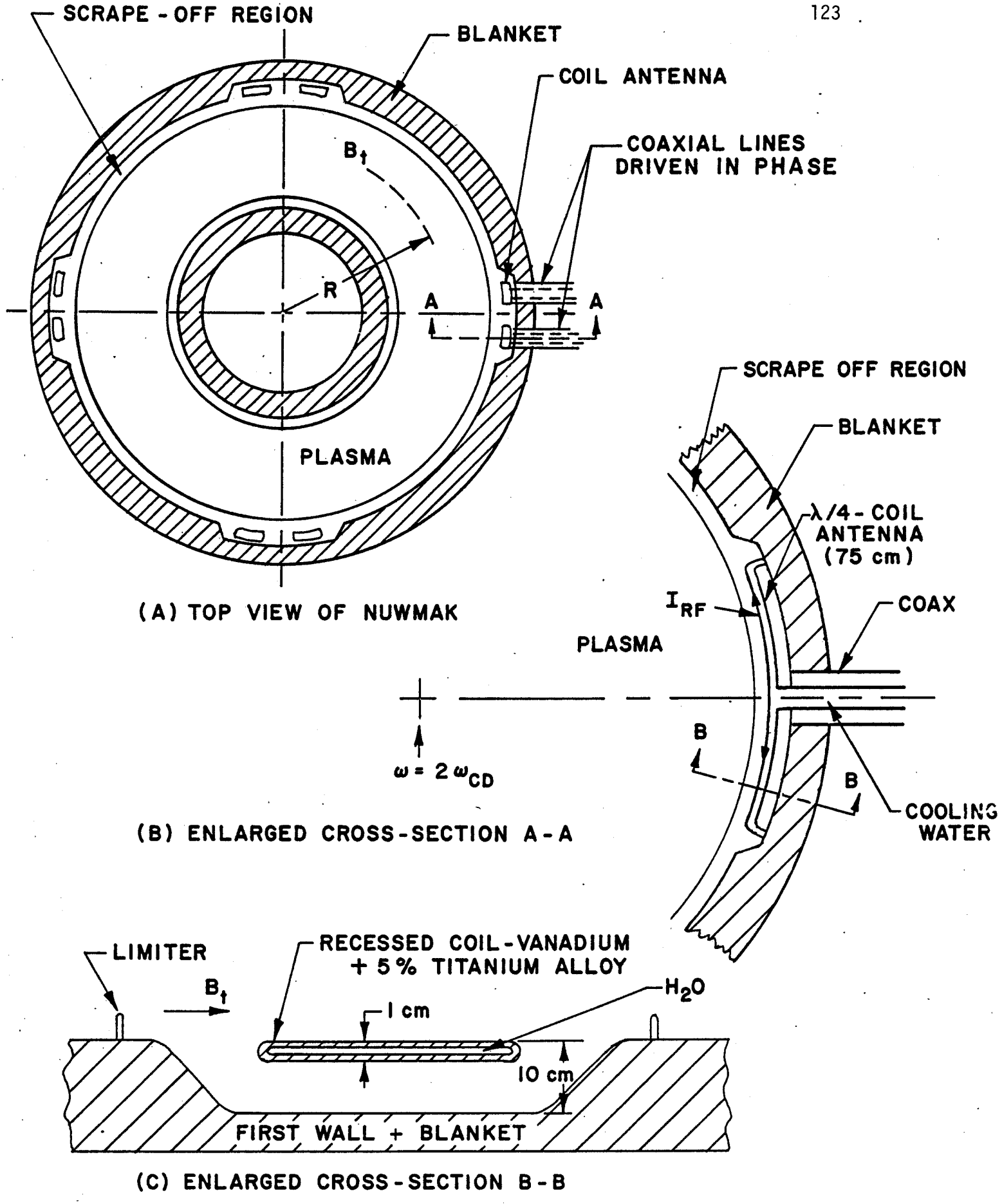

Fig. T5 Base design of RF coils coupling array for NUWMAK.

($\lambda_{\parallel}/2$) apart. The original 12"-coax has to be tapered gently to a 9.166"-coax towards the first wall. Keeping the characteristic impedance at 30 Ω, the inner conductor diameter becomes 14 cm. The short section of 9.166"-coax is required to carry 10 MW of power with a 3 sec pulse, and its peak power rating is 21 MW.

As shown in Figure 15(c), the coil antenna is recessed into a 10 cm deep groove in the first wall so that its profile remains essentially undisturbed. The edges of the coil and the groove are rounded, to prevent field disruption in their vicinity. The current coil and its 9.166"-coax feed are constructed of a vanadium alloy with 5% Ti so that they can withstand a constant wall loading of 4 MW/m^2 during the reactor burn cycle. Each coil is 14 cm wide toroidally and 1 cm thick, with a hollow inside through which pressurized water from the coax center conductor is run to keep the surface temperature at 350°C. The coil is placed 9 cm away from the surface of the groove to insure a matched 30 ohm driving impedance.

V-E. Prime Power Requirement for the Overall RF System

Numerical calculations using a global energy balance model indicate that a 3-sec RF pulse of 80 MW power is required at the first wall to ignite the plasma. However, considerably more power is needed from the utility lines to compensate for losses due to dissipation along the intermediate stages. A total prime power requirement will be assessed according to the efficiency of each subsystem.

Power is assumed to be supplied primarily by a utility source. A series of three-phase high voltage step-up transformers, which have a nominal efficiency of 85%, delivers power to the entire high voltage end of the RF system at the required level. Each RF module consists of a high-voltage (~ 40 kV, 125 A) pulse generator which serves as a DC power supply for the tubes in the IPA/HPA stage. The efficiency of a SCR bridge power supply is about 95%. For each IPA/HPA stage, the efficiency is essentially determined by the HPA as long as its power gain is sufficiently high (~ 20 dB). For a class C coaxitron at 92 MHz CW with a 1 MHz bandwidth and 2.5-5 MW output, the projected efficiency is 75-80%. A corresponding super-power triode operating class C narrowband will have a higher efficiency (~ 90%) but has yet to be developed with the 3 sec pulse widths required. Dissipation losses along the 10 meter long coax, the BeO window, and the resonant cavity walls amount to about 3% of the power flow. These results are summarized as follows:

Subsystem	Efficiency
HV Transformers	85%
DC Power Supply	95%
IPA/HPA	75%
Transmission Line + Cavity	97%
Cascaded Total	59%

For a power absorption of 80 MW by the plasma, a prime power of 136 MW is required from the line. This number may be somewhat optimistic because of the uncertainty of the HPA efficiency, but it, nevertheless, provides some ideas about the overall efficiency of the RF heating system.

References

1. B. W. Reed, O. N. Bowen, H. M. Hill, J. Q. Lawson, W. G. Newman and A. J. Sivo, PPPL Report - 1410 (1977).

2. W. M. Stacey, Jr., et al., Argonne National Laboratory Report ANL/CTR-76-3, Vol. 1 (1976).

3. Private communication with J. D. Stabley, RCA, Lancaster, Pennsylvania.

4. J. E. Scharer, R. W. Conn and D. T. Blackfield, EPRI Report ER-268 (1976).

5. Prodelin, Inc., General Catalog (1976).

6. W. M. Stacey, Jr., et al., Argonne National Laboratory Report ANL/CTR-76-3, Vol. 2 (1976).

7. S. Ramo, J. R. Whinnery and T. Van Duzer, Fields and Waves in Communication Electronics, John Wiley & Sons, New York (1965).

8. The Task Group on Special Purpose Materials, U.S. Department of Energy Report DOE/ET-0015 (1978).

9. Walter H. Kohl, Handbook of Materials and Techniques for Vacuum Devices, Reinhold Publishing Corporation, New York (1967).

10. Private communication with D. K. Sze, Nuclear Engineering Department, University of Wisconsin, Madison (1978).

11. Private communication with E. Cheng, Nuclear Engineering Department, University of Wisconsin, Madison (1978).

12. R. Papoular, Electrical Phenomena in Gases, American Elsevier Publishing Company, Incorporated, New York (1965).

13. A. M. Howatson, An Introduction to Gas Discharges, Pergamon Press, Oxford (1965).

14. A. J. Hatch and H. B. Williams, J. Appl. Phys. 25, 417 (1954).

15. R. F. Harrington, Time-Harmonic Electromagnetic Fields, McGraw-Hill Book Company, New York (1961).

16. D. G. Swanson and Y. C. Ngan, Phys. Rev. Lett. 35, 517 (1975); J. E. Scharer, B. D. McVey and T. K. Mau, Nuclear Fusion 17, 297 (1977); J. Jacquinot, B. D. McVey and J. E. Scharer, Phys. Rev. Lett. 39, 88 (1977).

17. R. E. Collin, Field Theory of Guided Waves, McGraw-Hill Book Company, New York (1960).

VI. Summary

We have examined the use of fast magnetosonic wave heating in the ion cyclotron frequency range for heating a conceptual tokamak reactor to ignition. The current status of theoretical work on the subject was first reviewed. The linear local dispersion and absorption properties for the fast magnetosonic branch and coalescence in spatial regions near the second ion cyclotron harmonic with the ion Bernstein branch are well understood. The competing processes of ion cyclotron harmonic absorption and mode conversion to the ion Bernstein branch in spatial regions near the second ion cyclotron harmonic was discussed. Researchers have found that for low values of $k_{\parallel}$, mode conversion processes can dominate the absorption process. Further, as reactor parameters of higher density and temperature are reached, the mode conversion process is expected to become more pronounced and contribute to a reduction in the fast magnetosonic wave Q for lower values of $k_{\parallel}$. This, together with a stronger finite ion gyroradius absorption of the fast wave branch for higher $k_{\parallel}$ in the reactor regime are expected to contribute to a lower wave Q situation than was previously anticipated. Finally, the importance of rotational transform in tokamaks in determining the local $k_{\parallel}$ in the absorption zone and its relation to electron Landau damping via the ion Bernstein mode or ion cyclotron harmonic absorption is noted. According to ray tracing studies, this, together with the poloidal location and $k_{\parallel}$ spectrum excited by the launching structure essentially determine the species, spatial deposition profile, and efficiency of heating in the ion cyclotron frequency range. The formulation and solution of a tokamak heating, startup, and coupling

problem taking mode conversion processes into account is quite formidable and will have to await further detailed work on the subject.

This work uses the weak damping approximation to calculate local ion and electron power absorption density. The resulting ion absorption, when averaged over a flux surface in a tokamak, yields a spatial deposition profile which is highly peaked on the axis, in agreement with previous work by Stix.

The problem of eigenmode density in a reactor as the radial, poloidal, and toroidal indices are varied is then addressed. It is shown that for the compact size of the NUWMAK reactor, the mode density is considerably lower than that for previous reactor designs. Ideally, a wave launching structure with low azimuthal mode number, $|m| < 3$, and a narrow but moderate $k_{\parallel}$ spectrum, $k_{\parallel} \simeq 20\ m^{-1}$, can be used to minimize mode conversion processes and ensure substantial ion cyclotron harmonic absorption near the plasma core. The launching structure spectrum can, ideally, provide selectivity so that several modes are excited at any one time and complex mode tracking is not required. However, the selectivity is such that several modes are simultaneously excited but that large numbers are avoided so that destructive interference of total wave fields far from the launching structure is not substantial.

Next, the ion and electron power absorption expressions are averaged over the tokamak cross-section and incorporated in a spatially independent, time dependent model which solves the ion and electron energy balance equations. The results show that for absorbed power levels of 80 MW and above, an equilibrium ion temperature of 15 keV

can be reached within 3 seconds after the Ohmic heating phase. By operating at higher RF power levels of 175 MW, an equilibrium can be reached due to the faster rise in ion temperature after a second, allowing a better duty cycle if the reactor burn time is limited.

It is found that the ions absorb most of the RF power initially, but that as the electrons heat up a substantial amont of RF power is delivered to the electrons during the final phase of ignition.

Finally, we have looked at RF heating the plasma during the Ohmic heating phase in order to improve the duty cycle and reduce RF peak power requirements. The power is linearly ramped from 0 to 75 MW over a period of 3 seconds and remains at 75 MW for an additional second. This is done to keep the poloidal β at a sufficiently low value so that confinement of heated particles is assured. This procedure, assuming that coupling efficiency from the launching structure to the plasma is not degraded, results in a reduced net energy input requirement and more time for the thermonuclear burn phase of the reactor power cycle. However, the practicality of its implementation and possible benefits for the reactor cycle must await more detailed work.

For the reactor startup calculations, the power levels quoted are those absorbed by the plasma. The problem of efficient coupling from an external generator through a launching structure to the plasma was investigated. It was immediately recognized that, due to the moderate wave Q and low wave impedance in a reactor, a coupler which performs an impedance transformation between the plasma and a higher impedance transmission line is desired. Cavity-backed aperture and coil antennas located near the torus wall were proposed.

A coupling calculation was made for the driving point impedance at the coaxial feed point to the TE_{101} mode aperture cavity. By assuming a single eigenmode within the reactor, the field at the apertures is calculated for a given power absorbed in the plasma. It is found that by making a twelve by four array of 15 cm major axis elliptical apertures in the lower part of the external cavity, the desired impedance transformation is achieved by locating the coaxial feed near a corner in the upper part of the cavity. The cavity-backed aperture coupler is particularly attractive since it is flush mounted with the torus wall, achieves the impedance transformation through the location of the coaxial feed point and apertures, and reduces the RF field intensity at the torus wall by distributing the power flow over the large surface area of the aperture. This preliminary calculation indicates the potential of such a technique and suggests that implementation of aperture coupling on current ICRF experiments should be encouraged.

For coil antenna coupling, resonant $\lambda/2$ antennas may be used to enhance the radiation resistance in reactors. We considered an antenna about $\lambda/2$ long fed from a higher voltage point near the ends of the antenna. This design allows a solution for a vacuum zone between the antenna and wall of about 10 cm.

In the last section the technological and hardware design for the radiofrequency heating system was presented. The RF generators provide 20 MW/port for each of four ports at the first wall of the reactor. The frequency is 92 MHz and coaxitrons or tetrodes having 5 MW output/tube are used in units of four to provide the required power.

A 30 Ohm coaxial line of one foot (= 30.5 cm) outer diameter is used to transport the RF energy over 10 meters from the generators to the antenna systems mounted on the torus. A half-wavelength beryllium oxide window is placed just outside the shield so that radiation damage is not a problem. By bending the coaxial line and filling the center conductor with borated water for cooling, the neutron flux down the annulus of the coax can be essentially eliminated at the position of the RF window.

The problem of RF breakdown in the coupling system is solved by proper design of the coaxial system to accommodate 20 MW power levels. A safety factor for multipactor and ionization breakdown is provided by either vacuum pumping or pressurized operation of the coaxial line.

The cavity-backed aperture antenna has a radial width of 10 cm, a toroidal length of 1.85 m, and a poloidal heigth of 3.5 m corresponding to a TE_{101} mode resonance at 92 MHz. The cavity is constructed of 95% vanadium and 5% titanium alloy yielding a high conductivity, low induced radioactivity level with good strength and thermal conductivity properties for cooling. The wall thickness is 2 mm allowing the neutrons to pass through the cavity region and be collected in the reactor blanket. Cooling pipes of 0.5 cm diameter are located on the inside of the cavity. Pressurized water is used to cool the cavity to 300°C during the burn cycle so that the electrical and mechanical properties of the cavity are maintained. An alternative coil coupling system is also considered which is close to $\lambda/2$ long and fed from the end in order to improve the radiation resistance to match a 30 Ohm line. The coil is made from the same materials as the cavity

design and is flush mounted with the torus wall with a 10 cm groove cut behind the antenna in order to reduce image currents. The coils are 14 cm in toroidal width by 1 cm thick with a hollow center to provide water cooling to keep the surface temperature at 300°C.

Finally, the overall electrical efficiency of such a high power heating system including the HV transformers (85%), D.C. power supply (95%), RF amplifiers (75%) and transmission line and cavity (97%) is 59%. For an 80 MW power absorption by the plasma, 136 MW are required from the line for a three second startup period.

It is recognized that considerable experimental investigation of high power ICRF heating is required to validate it as a means for igniting a tokamak reactor. However, this preliminary investigation of scaling to reactor size should provide some degree of optimism, as well as identifying problems which require more work before the ignition of a tokamak reactor by ion cyclotron harmonic heating can be realistically achieved.

Acknowledgements

We would like to thank Brian McVey for many discussions regarding the role of mode conversion and the interpretation of ray tracing results for a reactor tokamak. We would also like to thank Dai-Kai Sze and the Wisconsin NUWMAK design group for their many suggestions regarding the choice of coupler material, cooling of the antennas, and the effects of neutron irradiation on the fast magnetosonic wave heating system.